HYDROGEN EMBRITTLEMENT OF NANOSTRUCTRED BAINITIC HIGH STRENGTH STEEL

A Dissertation

by

ARASH SHADRAVAN

Submitted to the Office of Graduate and Professional Studies of
Texas A&M University
in partial fulfillment of the requirements for the degree of

DOCTOR OF PHILOSOPHY

Chair of Committee,	Raymundo Case
Committee Members,	Homero Castaneda Lopez
	Mahmood Amani
	Bilal Mansoor
Head of Department,	Ibrahim Karaman

August 2019

Major Subject: Materials Science and Engineering

ABSTRACT

Characterization of nanostructured bainitic high strength steel revealed austenitic and bainitic-ferritic constituents. Hydrogen diffuses through austenite slower than bainitic ferrite. Discovering the effective hydrogen diffusion coefficient, subsurface hydrogen concertation and number of traps of such a microstructure leads to a deeper understanding of the role of retained austenite, as the dominant trap in such microstructures. Devanathan–Stachurski hydrogen permeation experiments determined the permeation parameters and subsequently numbers of reversible and irreversible traps. Volume of the retained austenite correlated well with the total number of traps and the mean free path.

Lower mean free path, higher austenite content and trap density and more importantly finer dispersed distribution of films of retained austenite alongside with thin plates of bainitic ferrite satisfied percolation through the austenite. Therefore, permeation experiments demonstrated the lowest diffusivity in 2000 MPa microstructure between all the bainitic high strength membranes. On the contrary, combination of granular morphology and smaller volume of retained austenite triggered the loss of percolation and yielded to the lowest diffusivity for 1000 MPa microstructure. Higher volume of the retained austenite in isolation in the nanostructured bainitic steel does not produce lower diffusivity. With a semi analytical nonlinear fracture mechanics model and NTSSRT, we evaluated the hydrogen embrittlement susceptibility of the 1600 MPa exposed to H_2S and the 2000 MPa steels exposed to hydrogen charging. At a certain hydrogen concertation, pre-charged samples showed greater decrease in hydrogen embrittlement index and J integral drop.

DEDICATION

To my family,

For their support and love.

ACKNOWLEDGEMENTS

Over the past few years, I had the pleasure of working in the National Corrosion and Materials Reliability Laboratory at Texas A&M University. Several people influenced and helped me to accomplish my PhD.

First, I would like to express my sincere gratitude to my advisor, Raymundo Case. After several years of working in the industry, he returned to academia. I was honored to be his first Ph.D. student in Materials Science and Engineering, graduating from Texas A&M University. He passionately taught me electrochemistry and safe slow strain rate test (SSRT) experimentation with hydrogen sulfide. I truly appreciate him for all the brainstorming including our heated discussions on the role of hydrogen embrittling high strength steel and fracture mechanics. He is a great electrochemist and is capable of connecting the dots in the simplest and most effective way. I learned a lot from him.

Second, I must thank Homero Castaneda, a truly gracious corrosion scientist who patiently taught me not only the fundamentals of corrosion but also familiarized me with NACE! Under his supervision, I had the opportunity to establish NACE Texas A&M University section, serve as its president for three years and grow my leadership skills. Our chapter reached various milestones including holding several industry lecture series inviting many corrosion engineers. He supported us to initiate the Annual Corrosion and Materials Reliability Symposium (CMRS) at Texas A&M. We promoted the culture of safety and health on campus and echoed gaining the value of leadership skills early on.

Mahmood Amani has been my life-long mentor. In the past ten years, his kind contributions to my personal growth as an engineer have been beyond imagination. I have

been always grateful to him for steering my academic path towards starting graduate school at Texas A&M University. He has been always supportive of me and his wisdom always shed light on my path.

I should genuinely thank Bilal Mansoor as well. Having him in my PhD graduation committee and receiving feedback from him was very valuable.

During my PhD, I had the pleasure of working with several friends, graduate students, postdocs and staff: Mohammadali Tarrahi, Cody Statton, Mahdi Mohajeri, Behrouz Haghgouyan and Jing Ning. I should thank Ibrahim Karaman, Michael Elverud, Anup Bandyopadhyay, Murat Kaynak, Jules Henry and Erin Bandza, in Materials Science and Engineering department, Wilson Serem, Yordanos Bisrat and Andrew Mott at Materials Characterization Facility, Tom Stephens, Rick Littleton and Hansoo Kim at Microscopy and Imaging Center (MIC).

ExxonMobil, Shell, ConocoPhillips, Schlumberger, Tenaris and VODIK generously provided the funding sources for my Ph.D. research: David Fischer, Julian Hallai, Brian Chambers, Manuel Gonzalez, Mark Yonovich, Sebastián Cravero, Kris Kocurek, Hernan Enrique Rincon, Argie Rumann, Carey Hilton, Clayton Sikes, Steve Sikes and Jeff Stamps all played a role by either providing me with the nanostructured steel samples, using SSRT to investigate the samples susceptibility to hydrogen embrittlement or building finite element models. I am very thankful to ExxonMobil who not only allowed me to work on building a new machine learning based corrosion prediction model at its Upstream Research Company through a summer internship during my third year, but also invited me to embark on an exciting full-time career as a materials integrity engineer.

I would like to truly thank certain individuals who not only delivered a talk at Texas A&M and supported our NACE section but also played an active role in developing future aggie corrosion and materials engineers; Bob Chalker, Heather Hill, Cindy Tracy and Michelle Simpson from NACE International, Doug Fairchild, Cecilie Haarseth, Conchita Mendez, Jorge Pacheco and Yao Xiong from ExxonMobil, Kristen Williams from Boeing, John Stevens and Tracey Jackson from Baker Hughes, Ardjan Kopliku and Time Bieri from BP, Sandra Hernandez from Chevron, Daria Bougai from Shell, Hernan Enrique Rincon from ConocoPhillips, Herman Amaya and James Fajt from Schlumberger, Larry Siqueiros from Marathon Oil, Alyx Kahn from Marathon Petroleum, Matthew Banasik from Anadarko, Drew Hevle from Kinder Morgan, Krista Heidersbach and Sudhakar Mahajanam from Stress Engineering and Fred Addington along with Cesar Espinoza from PinnacleArt.

My NACE dream team made all our activities possible on campus. I want to acknowledge all of them in the past three years, Reece Goldsberry, Yenny Cubides, Mahdi Mohajeri, Tse-Ming Chiu, Abhinav Srivastava, Hannah Boon, Tianyang Zhou, Dimitris Loufakis, Juanita Pombo, Ines Figueroa, Kennon Wishert, Alan Martinez and Brion Cakaj. Lastly, I would like to truly thank my family for their indefinite love, unwavering support and perpetual encouragement. My parents, Azar and Rasoul, my brother, Arvin, and Sarah, thank you very much y’all!

CONTRIBUTORS AND FUNDING SOURCES

This work was supervised by a dissertation committee consisting of Professor Raymundo Case of the Department of Materials Science and Engineering, Professor Homero Castaneda of the Department of Materials Science and Engineering, Professor Mahmood Amani of the Department of Petroleum Engineering and Professor Bilal Mansoor at the Department of Mechanical Engineering. All other work conducted for this dissertation was completed by the student independently.

This work was made possible through the funding provided by Schlumberger, VODIK Lab, ExxonMobil, Shell, ConocoPhillips and Tenaris.

Its contents are solely the responsibility of the authors and do not necessarily represent the official views of the TEES.

TABLE OF CONTENTS

Page

LIST OF FIGURES

Page

LIST OF TABLES

Page

1. INTRODUCTION

High strength steels has been an evolving field of research in academia and industry. The utilization of high strength steels in increasingly more harsh environments has promoted manufacturing of new generations of highly ductile high-strength steels. Emergent intricacy in designing parts safely along with requirements to assure stiffness with less wall thickness has increased the use of high strength steels. The auto industry used dual-phase steels and manufactured Transformation-Induced Plasticity steels. Complex Phase steels were born once researchers discovered the benefits of partially replacing martensite by bainite. Martensitic steels gained popularity due to the demand for intrusion resistance and their high yield strength to tensile strength ratio. Hydrogen embrittlement for more than a century imposed several detrimental impacts on the ductility of steels and incurred hefty expenses in numerous industrial applications. Hydrogen embrittlement weakens the interatomic bonds between grains and causes premature failures.

Despite significant research in the area of hydrogen embrittlement, it is fair to emphasize that we still do not fully understand this complex phenomenon. Hydrogen embrittlement is a major challenge to several industries including oil and gas, aerospace, nuclear and automotive and it has plagued military airplanes, pipelines, nuclear waste disposals and power systems. Hydrogen embrittlement and stress corrosion cracking, together, could cause failures in the components made out of high strength steels. Despite various metallurgical processes used to promote the toughness of high strength steels, their microstructure is susceptible to hydrogen embrittlement. Damage produced by hydrogen

in high strength steels poses a risk to the integrity of many structures and equipment. The premier challenge in this field is to understand how hydrogen embrittles high strength steels. The hydrogen embrittlement mechanisms are still widely debated. This report analyzes hydrogen embrittlement mechanisms including adsorption induced dislocation emission, hydrogen enhanced local plasticity, hydrogen enhanced decohesion and a combination of these mechanism. Finally, this study investigates the impacts of hydrogen embrittlement on the microstructure of high strength steels and proposes future avenues of research as potential solutions to combat this detrimental phenomenon.

High strength steels were traditionally used in the nuclear, petroleum, aerospace, and recently in automobile industries. Hydrogen damage is a common cause of failure in high strength steels. Almost a century ago, Pfeil found out that hydrogen exposure to steel alters its mechanical performance, leading to a considerable loss in ductility at room temperature due to the penetration of atomic hydrogen into the steel[1]. Hydrogen atoms are nearly omnipresent and even 10^{-4} of its weight percentage can lead to steel cracking and inter-granular, trans-granular or ductile failures. The first and second generation of Advanced High Strength Steels includes Dual-Phase (DP), Complex-Phase (CP), Transformation-Induced-Plasticity (TRIP) with high-energy absorption, Martensitic (MS), Hot-Formed (HF), and Twinning-Induced Plasticity (TWIP). Third generation of Advanced high-strength steel (AHSS) refers to a family of cost-effective ductile steels made by specialty alloying thermo-mechanical methods. **Figure 1** shows a banana curve of different families of high strength steels [2].

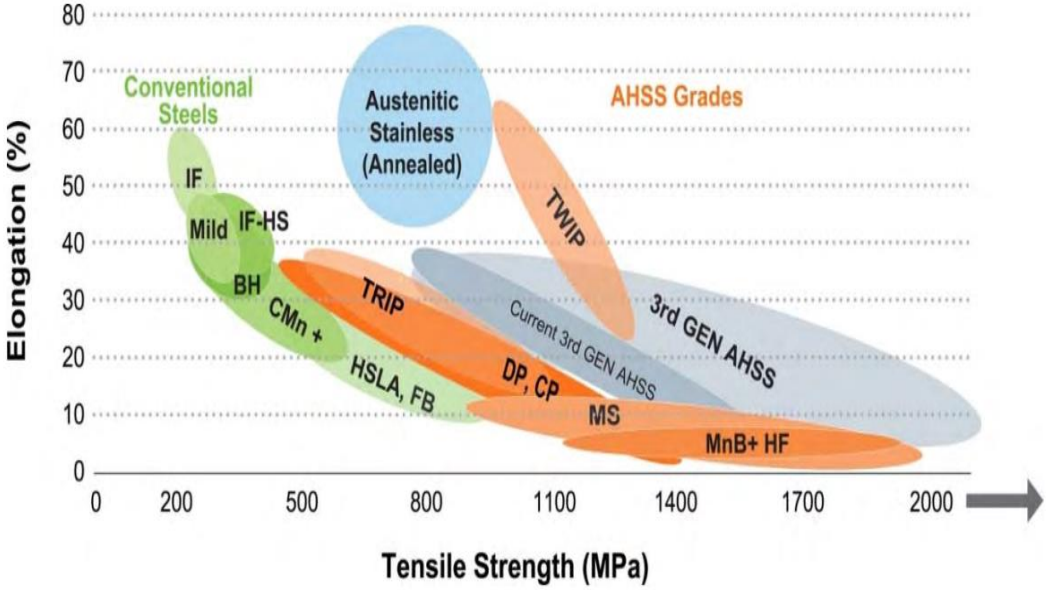

Figure 1. Elongation-tensile strength plot of conventional steels and advanced high strength steels [2].

Advanced high strength steel steels, such as high strength low alloy (HSLA), contain more than two phases to enhance the strength and the ductility that single-phase steels and specialty alloys grades cannot provide. While AHSS are manufactured, through exact alloys and meticulous thermomechanical processes, HSLA materials gain their ductility and strength by solid solution hardening and alloying.

It is no longer appropriate to qualify steel for AHSS category by strength alone. Multiple phase steels with 440 MPa strength, can be categorized as AHSS, however, in the past, steels with tensile strength over 550 MPa would qualify as AHSS and any steel above 780 MPa was labeled as ultrahigh-strength steels. In this report, high strength steel (HSS) refers to steels with more than 300 MPa ultimate tensile strength.

1.1. High strength steels

1.1.1. Dual phase steel

DP steels include a soft ferritic matrix with a 10-40% of hard martensitic island-shaped second phase. DP steels with at least 20% volume fraction of martensite are called partially martensitic. Raising the volume density of hard second phases typically boosts the strength. Dual phase (ferrite and martensite) steels are manufactured through precise cooling from the austenite or two-phase ferrite/austenite. At the time of steel deformation, lower strength ferrite phase would go through strain concentration resulting in a preliminary rate for work-hardening (n-value) showed by such steels[2].

The outstanding elongation and work hardening rate gives DP steels high ultimate tensile strengths compared to conventional steels of similar yield strength. In dual phase steels, carbon along with optimal cooling rates develop martensite, which raises hardness. Mg, Cr, Mo, V and Ni contribute to higher hardenability. C, Si and P, on the other hand, also makes martensite stronger. To achieve a homogeneous dual phase steel microstructure with properly distributed martensite islands and fine recrystallized ferrite, we use an uninterrupted annealing process. This process comprises of reheating of the initial cold-rolled pearlitic-ferritic or bainitic-ferritic microstructure into the range of inter-critical annealing or quick austenitic annealing, after quenching below the martensite start temperature. **Figure 2** demonstrates the heat treatment approaches utilized to attain a ferritic-martensitic dual phase microstructure. The ultimate annealing process for dual phase steels include keeping the material in an austenitic-ferritic zone and then quenching

while holding at temperatures marginally less than martensite initiation temperature that austenite changes to martensite.

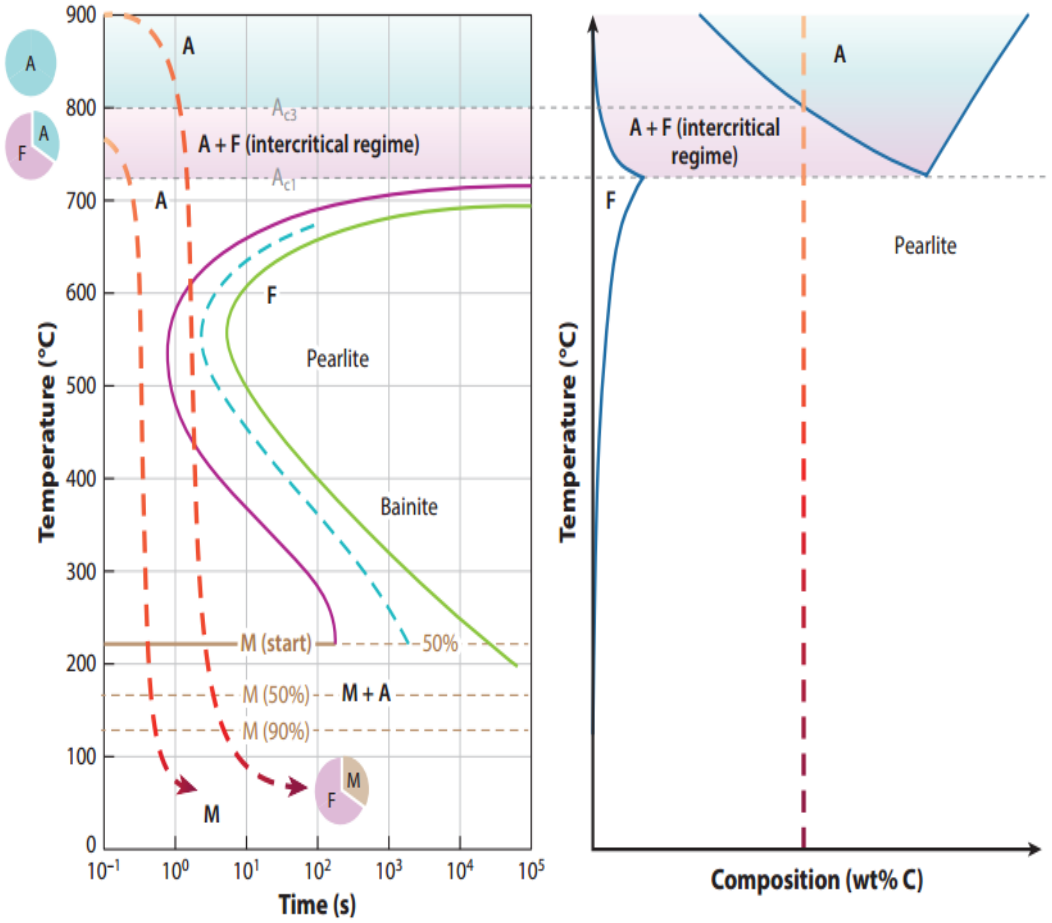

Figure 2. Heat treatment approaches to get a ferritic-martensitic microstructure, A (austenite); F (ferrite); M (martensite)[3].

Krajewski et al. proposed a valid artificial neural network (ANN) model to shed light on the relationship of tensile strength of dual phase steels with the microstructure, heat treatment, alloying and transition temperature, **Figure 3** [4].

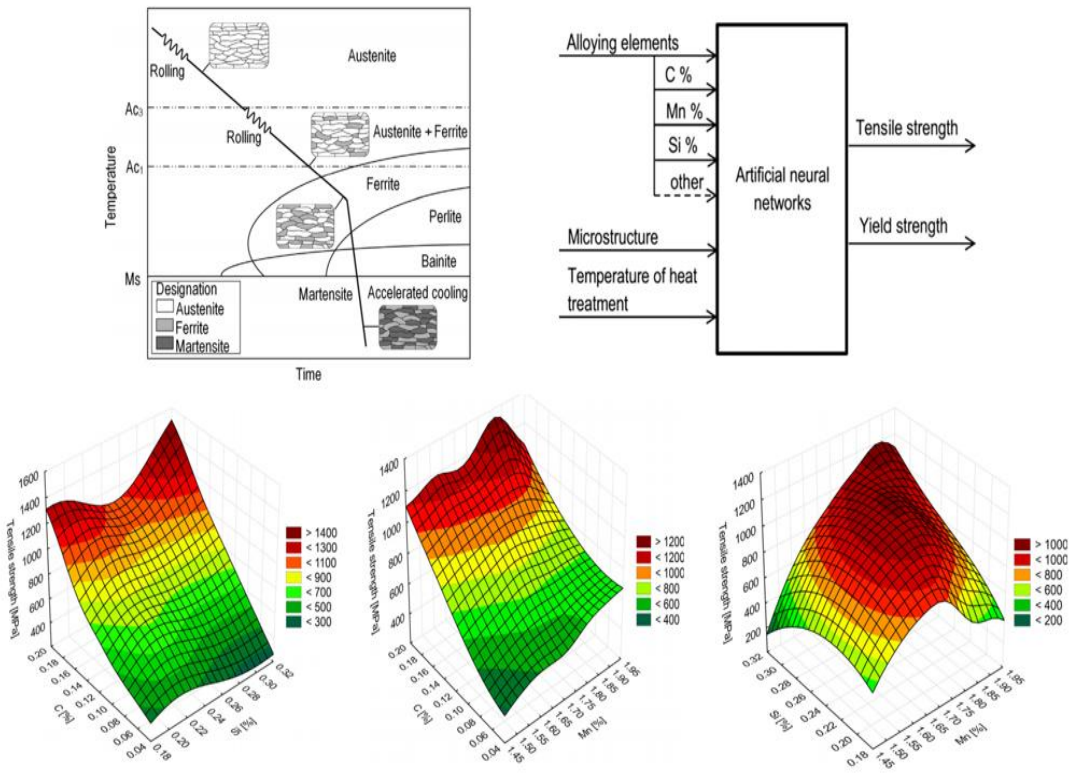

Figure 3. AHSS phase transformations due to cooling mode. ANN model relates tensile strength of DP steels to C%, Si% and Mn% [4].

1.1.2. Transformation induced plasticity steel

TRIP steel consists of five volume percent of retained austenite distributed in a matrix of ferrite besides martensite or bainite (formed due to isothermal hold and intermediate temperature). The ultimate retained austenite fraction would vary based on the C and Si content. Similar to DP steels, TRIP has a high work hardening due to the dispersion of hard second phases in soft ferrite [2]. Nevertheless, retained austenite would change to martensite gradually due to strain increase leading to final higher rate of work hardening at more stress level, **Figure 4.** TRIP steels usually have 0.5 - 0.55% ferrite, 0.30 - 0.35% bainite, 0.07 - 0.15% retained austenite and perhaps 0.01 - 0.05% martensite. Dini et al.

used ANN to model how in a Fe–Mn–(Al, Si) TRIP steel raising Mn percentage impacts elongation, tensile and yield strength [5].

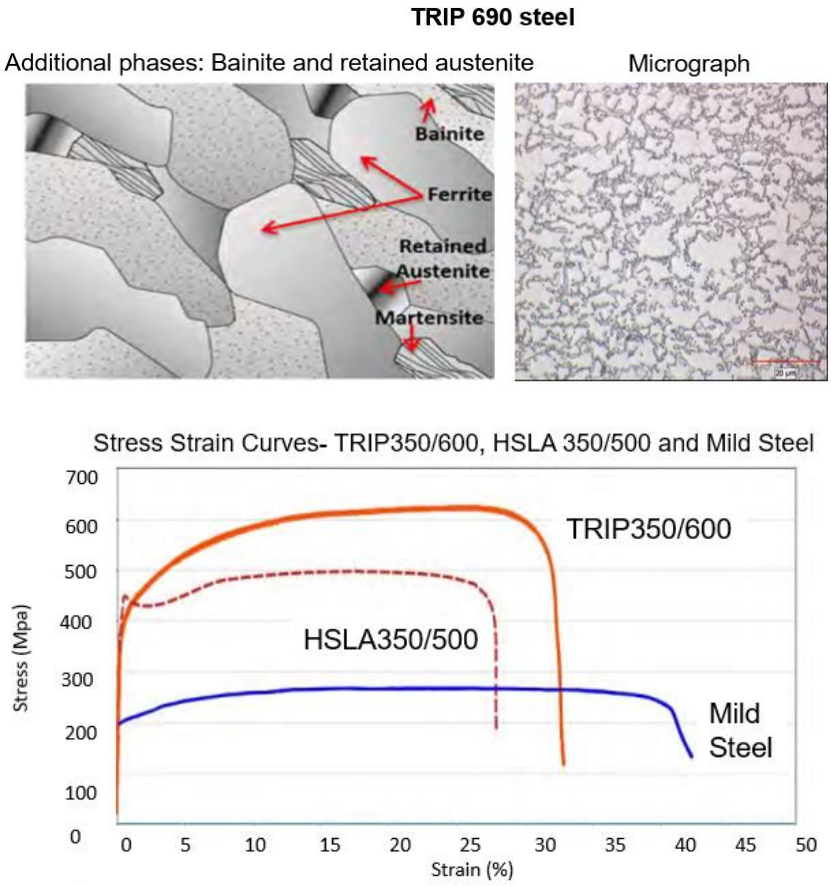

Figure 4. TRIP steel microstructure and its mechanical performance vs. mild steel and HSLA steel [2].

A ferritic-martensitic steel with retained austenite was studied experimentally and through microstructural simulations. Finite element method with the crystal plasticity based constitutive equations was used to model the microstructure similar to a composite, which include ferrite, martensite and retained austenite. This research showed that in modeling retained austenite, we should consider plasticity of untransformed austenite,

transformation induced plasticity, in addition to plasticity in the produced martensite. This would enable us to properly forecast the macroscopic flow behavior and understand how the deformation-induced martensite volume fraction evolves with respect to strain [6]. Artificial Neural networks was could be also utilized to estimate the properties of a TRIP steels. **Figure 5** shows three heat maps of how the variation in the chemical composition of a 15Mn–(2–4) Si–(2–4) Al TRIP steels could change the elongation, yield strength and tensile strength.

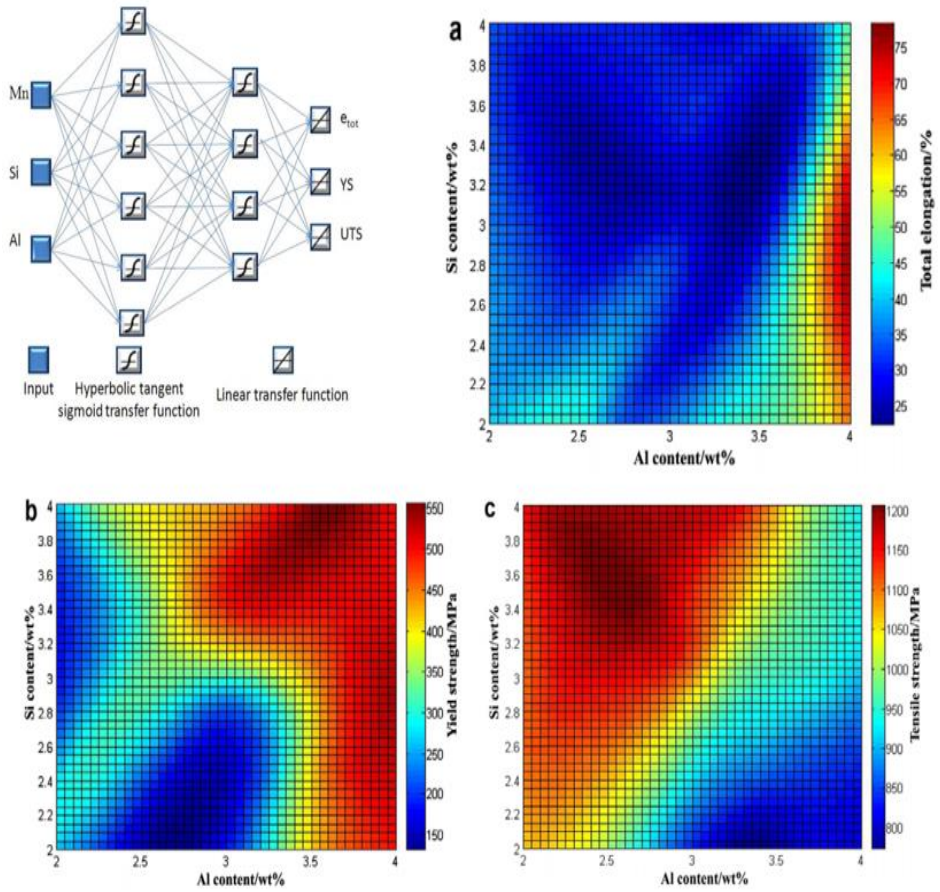

Figure 5. Projection of mechanical performance of 15Mn–(2–4)Si–(2–4)Al TRIP steels: (a) elongation%, (b) yield strength (MPa) , and (c) tensile strength(MPa)[5].

1.1.3. Complex phase steel

Complex phase steels characterize the transition to steel with significantly more ultimate tensile strengths and its microstructure includes scarce amount of retained austenite, martensite and pearlite within the ferritic-bainitic matrix[2], **Figure 6.** Micro alloying by Ti and Nb along with retarded crystallization lead to extremely refined grains. CP steels, comparatively with DP steels at 800 Mpa tensile strength, demonstrate greater yield strength. This family of AHSS steels own great energy absorption and residual deformation.

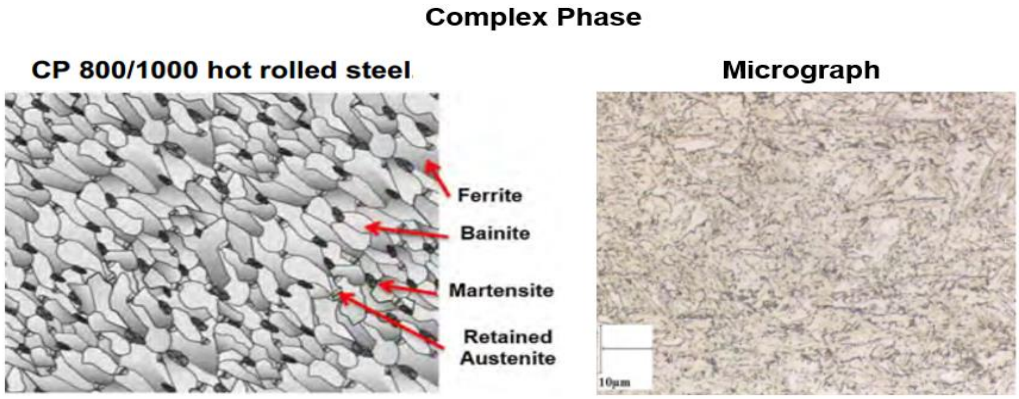

Figure 6. Microstructure of a complex phase steel [2].

1.1.3.1. Nanostructured bainitic steel

Bainite, an acicular, dark etching aggregate, was first discovered by Davenport and Bain in 1930s. They initially classified Bainite as a form of martensite and named it martensite troostite. Bainite structure, however, etched more quickly than martensite and it was less relative to troostite (fine pearlite). For a similar hardness, Bainitic

microstructure exhibited to be tougher than martensite and triggered a huge excitement in the field of metallurgy.

The transformation of austenite at lower temperature could have two stages: premature bainitic reaction followed by very slow pearlite formation. Bainite transformation starts when BS temperature is reached. Higher under cooling below BS correlates well with the amount of bainite formation which enriched retained austenite. In fact, before bainitic formation, the composition of Austenite is not stable and therefore it splits to carbon free or carbon rich volume. Regions with scarce carbon will change to supersaturated bainite with same composition post iron carbide precipitation.

Microcopy techniques demonstrated that Bainite sheaves enhance in length much slower than martensite plates. They also happen to have irrational habit planes with planes different than martensite. Bainite plates do not intersect with austenite grain boundaries and the extent of transformation to bainite reduces, finally to zero, by increasing isothermal transformation temperature. **Figure 7** summarizes the history of bainite.

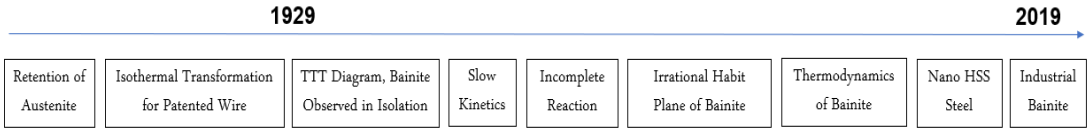

Figure 7. Research journey of Bainite

Bainite, in contract with pearlite and cementite, forms in separable stages. Pearlite happens at the similar austenite transformation front. The carbon which could not be accommodated by the ferrite, will be in cementite. Lower bainite as well as higher bainite

have accumulation of ferrite plates separated by cementite, martensite or austenite which is not transformed. Such aggregates known as bainite sheaves and the plates within each subunit is knows as sub-units which are connected in three dimensions[7]. Through several microscopy it was revealed that bainite has a wedge-shaped plate with the thicker side began from the nucleation site, often from austenite grain [8]. The subunits forming a bainite sheath have usually lath or lenticular shapes. Newer subunits also could nucleate close to the tips the existing subunits.

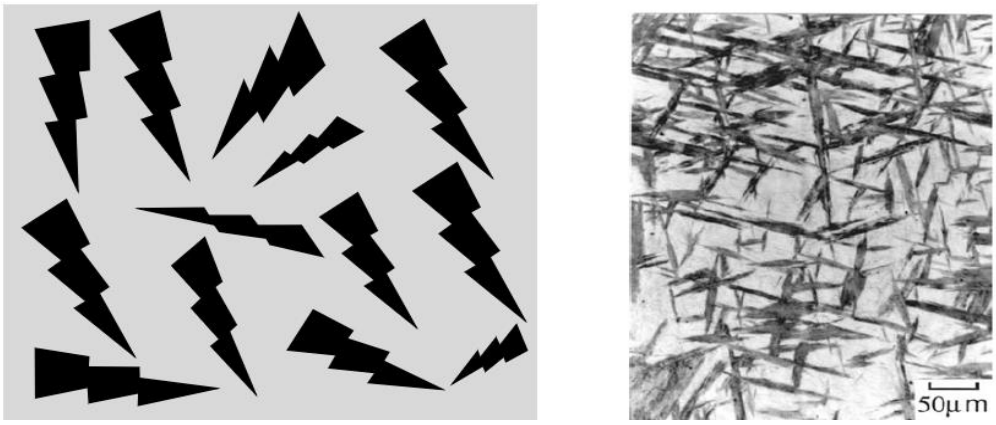

Figure 8. Microstructure model with several bainite sheaves, each sheath has some subunits (left), Sheaves of lower bainite in a partially transformed alloy (395C) Fe-0.3C-4Cr wt.% (right).

Austenite strength determines to what extent a change in shape is plastically accommodated. Haezebrouck anticipated the formation of plate shape due to swift radial growth and a parent phase with high yield stress which both favor an elastic growth [9]. Higher growth rate will entail higher strain rate making yielding even harder. Bainitic plates can mainly be in an elastic equilibrium with the matrix if the deformation is elastic. They continue to get thicker isothermally until strain energy equates the free energy. At

lower temperature, the driving force is higher and therefore these plates could grow more freely and become thicker [10]. **Equation 1** shows a relationship in a microstructure as a function of transformation temperature [11]. Dislocation density could be calculated in nanostructured Bainite via T, the reaction temperature in Kelvin and ρ_d, dislocation density in m^{-2}.

$$\log_{10} \rho_d = 10.292 + \frac{5770}{T} + \frac{10^2}{T^2} \quad (1)$$

Higher conventional heat-treatment temperature yields to a coarser microstructure. The dislocation density is often non-uniform, with the largest density at the bainitic ferrite and austenite interfaces. Through developing a quantitative model to discover the bainite plate thickness in steels containing silicon, it was revealed that austenite strength and the chemical free energy change of transformation, are mainly the most important factors affecting plate-thickness[12].

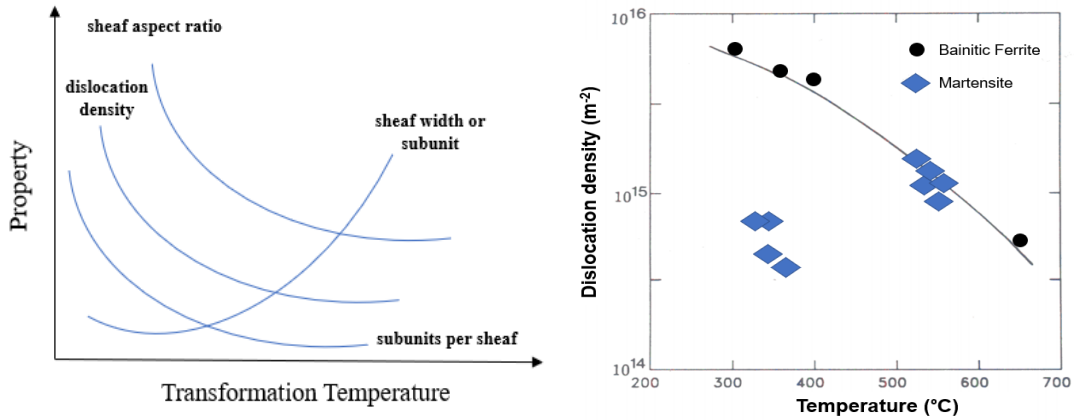

Figure 9. Transformation temperature increase will yield in the decrease in sheath aspect ratio, dislocation density and subunits per sheath and an increase in sheath width.

Table 1 details the composition of alloys with bainitic plates in which w_i shows the concentration in wt% of alloying elements, and $T_r = T - 25$ and T is the temperature in ˚C. The equation is based of data with thickness ranging from 0.053-0.330μm.

$$\text{Austenite Strength (MPa)} = \text{Temperature Term} * \text{Composition Term}$$

$$\sigma_Y = (1 - 0.26 \times 10^{-2}\, T_r + 0.47 \times 10^{-5}\, T_r^2 - 0.326 \times 10^{-8}\, T_r^3) * (15.4(4.4 + 23w_C + 1.3w_{si} + 0.24w_{Cr} + 0.94w_{Mo} + 32w_N)) \quad (2)$$

Table 1. Bainite plate thickness alloy composition (wt.%).

Alloy	C	Si	Mn	Ni	Cr	P	S	N
A	0.27	1.98	2.18	0.02	1.90	0.015	0.012	0.0054
B	0.46	2.10	2.15	0.02	-	.014	0.013	0.0062
C	0.1	1.77	2.12	2.00	0.02	0.013	0.012	0.0053
D	0.26	1.85	2.10	0.02	-	0.015	0.013	0.0086
E	0.26	1.93	2.04	0.02	1.02	0.015	0.010	0.0069
F	0.1	1.63	1.99	0.03	1.97	0.013	0.011	0.0080

Bainite orientations relative to an austenite grain affect the mechanical properties since it determines the length scale over which cleavage cracks or other deformation phenomena are not impeded[13-15]. A small block size helpful to higher toughness could be achieved by: (i) reduction of austenite grain size; (ii) guaranteeing an arbitrary crystallographic texture in the austenite; (iii) transforming at a large undercooling below BS; (iv) transforming from unstressed and undeformed austenite. High-carbon steels could often transform to lower bainite plates that do not have a homogeneous microstructure.

Microscopy showed black lines which are lower bainite is seen to have a black line running centrally along its axis, **Figure 10**, [16]. ε-carbide detection in lower bainite implies trapped large excess of carbon in bainitic ferrite when it first forms (≥ 0.25 wt%). **Figure 11** pictures the precipitation of variant cementite. Carbide participation in lower bainite results to a lesser fraction of inter-plate cementite at the austenite decomposition. Lower bainite usually has a more toughness than upper bainite, although it typically is stronger.

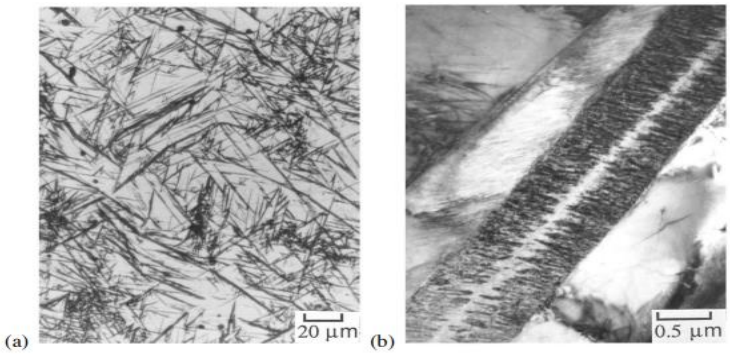

Figure 10. Optical and TEM micrographs of lower bainite in a plain carbon steel.

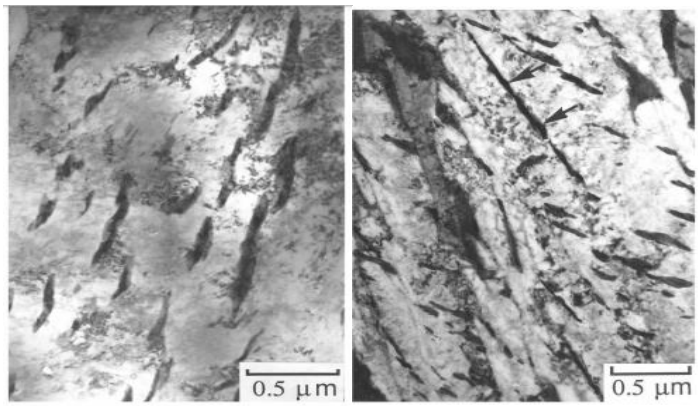

Figure 11. AISI 4340 steel, cementite particles between the ferrite platelets, upper bainite (left), Fe-0.3C-4.08Cr wt% showing a lower bainite produced via an isothermal transformation for a prolonged heat treatment (435 ˚C, 30 min) leading to the precipitation of carbides between the ferrite platelets(right).

The precipitation reactions for lower bainite can be summarized as below:

Table 2. Lower bainite precipitation reaction.

High dislocation density	Low dislocation density
$\gamma \rightarrow \gamma + \alpha_{b,\ supersaturated}$ $\rightarrow \theta_{\ in\ ferrite} + \alpha_{b,unsaturated} + \gamma_{enriched}$ $\rightarrow \alpha_{b,unsaturated} + \alpha + \theta_{between\ ferrite\ plates} + \theta_{in\ ferrite}$	$\gamma \rightarrow \gamma + \alpha_{b,supersaturated}$ $\rightarrow \varepsilon_{in\ ferrite} + \alpha_{b,unsaturated} + \gamma_{\ enriched}$ $\rightarrow \alpha_{b,unsaturated} + \varepsilon_{in\ ferrite} + \alpha + \theta_{between\ ferrite\ plates}$ $\rightarrow \alpha_{b,unsaturated} + \theta_{in\ ferrite} + \theta_{between\ ferrite\ plates} + \alpha$

Silicon often exists in steels as a result of the deoxidation reactions occurred during steelmaking. High concentration of silicon retards the cementite formation from austenite, making it feasible to have a carbide-free microstructure of austenite and bainitic ferrite. Silicon has an extremely low solubility in cementite which is in equilibrium with austenite. In the past two decades, research in the area of the nanostructured materials has evolved [17]. Nanostructured materials have at least one dimension less than 100 nm, while ultrafine-grained materials (UFG) grain size is between 200 nm and 1μm in diameter. However, it's difficult sometimes to distinguish between materials with the nano grain size to submicron size and practically any nanostructured metallic materials in bulk could be comprised of nanoscale and submicron-scale microstructures.

The first obstacle to overcome nanostructuring is the large-scale processing of high quality of nanomaterials given the fact that bulk materials has structural defects and impurities. The following processes could be used to make nanostructured metallic materials.

1) Solid Deformation Processing (SPD):
    a. Equal Channel Angular Pressing (ECAP)

b. Accumulative roll-bonding (ARB)

c. Mechanical attrition (MA)

d. High pressure torsion (HPT)

e. Mechanical machining process (MM).

2) Solid Reaction Processing: pearlite or ultrafine bainite structure in carbon steels via thermal reaction and deformation.

3) Liquid– Solid Transformation: liquid to solid phases transformation.

The focus of this research is on solid reaction processing, however severe deformation processing and liquid-solid transformation are briefly discussed as well.

Severe Plastic Deformation

Research on metals microstructural refinement under high plastic deformation is the reason behind the popularity of nanostructured metallic materials today. Through ECAP and HPT, ultrafine grains (100–300 nm) could be formed by repetitive application of large shear deformation on ductile metals leading to dislocation density (number of dislocations in a unit volume) up to 10^{14} to 10^{17} under strains as high as 5 [18]. Similarly, ARB is suitable for generating fine-grained microstructures especially for bulk nanostructured metallic materials production in the form of sheets. However, the inability to produce such materials in bulk, is one of obstacles for HPT and ECAP to become industrially feasible. 200 nm grain size could be also achieved by conventional machining process for production of foils, rods or sheets, from the coarse-grained bulk metals [19].

Liquid–Solid Transformation

Liquid–solid transformation developments could have two methods. Nano-grains could be produced by controlled heat treatment when an amorphous phase is created due to the solidification of a molten alloy [20]. Second method is thermal spray coating on the substrate. In this method, the molten phase stability is very important [21].

Solid Reaction Processes

Thermal reaction and diffusion could help building nanostructured materials when SPD would be challenging to use due to high flow stresses. Bainite steels have been used for a long period of time and their kinetics and nucleation were explained. Heat treating bainitic steels for a longer period at comparatively lower temperature could generate nano-bainitic ferrite plates (20–40 nm) in steels with high carbon concentration. For instance, supercooling Fe-0.78-0.98 C-Si-Mn-Cr-Mo alloys at (125–325 °C) with one to six days holding time results in the nucleation of ferrite in austenite [22]. Nanostructured bainitic steels could be made in large dimensions due to flexible heat treatment, while martensitic steels have limited dimensionality because of high cooling rate. Higher percentage of silicon in bainitic steels leads to higher strength and toughness [23]. A material can be made stronger by either diminishing its size and avoiding defects (e.g. carbon nanotubes) or by packing it with defects restricting dislocations mobility or reducing the microstructure scale via heat treatment (e.g. martensitic steels produced by rapid cooling).

1.2. Hydrogen assisted cracking

High strength steels are susceptible to hydrogen cracking and premature failures. The ASM materials handbook considers five types of hydrogen damages for metals and alloys: (1) hydrogen embrittlement (HE), (2) hydrogen-induced blistering, (3) cracking from

precipitation of internal hydrogen, (4) hydrogen attack and (5) hydride formation[24]. All hydrogen damages except hydrogen embrittlement, occurs with phase transformation and are comparatively easy to grasp qualitatively. Hydrogen embrittlement, on the other hand, is an abstract phenomenon.

Hydrogen assisted cracking (HAC) consists of internal hydrogen embrittlement (IHE) which refers to accumulation of pre-existing hydrogen near locations with large stress concentrations and hydrogen environment embrittlement (HEE) explaining cracking due to hydrogen sulfide or hydrogen exposure. Hydrogen embrittlement in high strength steels is certainly a problem in naval aviation since in offshore environments HSS would be exposed to salt water and other corrosive chemicals which aid the atomic hydrogen absorption [25]. As the strength level of a steel goes up, its susceptibility to HE also increases. Provided hydrogen reduces the atomic bonding strength, stress fields may play the main role in HE. On the other hand, for ductile failures, HE susceptibility is governed by the microstructures reactions to the strain field. Low hydrogen sensitivity and high hydrogen mobility make HE mechanisms difficult to understand. Difference in materials, hydrogen fugacity and loading along with experimental methods determine the main HE mechanism. Sievert's law explains the solubility of hydrogen in steel in equation 1, where k is hydrogen solubility, C_L is hydrogen concertation in lattice sites and P_{H2} is the pressure of hydrogen molecules in the voids:

$$C_L = k\left(P_{H_2}\right)^{0.5} \tag{3}$$

Hydrogen could be adsorbed to a metal surface in the hydrogen molecule. Hydrogen Thermal Desorption Analysis (TDA) investigates the desorption of adsorbed gases from

the metal surface. Experimental variables (e.g. temperature ramp rate and sample size) along with hydrogen states in the metal affect the desorption rate profile. Lovicu et al. defined embrittlement index (EI) for hydrogen embrittlement for a notched sample, which implies the influence of HE on steel's strength[26].

$$EI = \frac{Notched\ ultimale\ tensile\ strength_{no\ H} - Notched\ Ultimate\ Tensile\ Strength_{maxH}}{Notched\ ultimale\ tensile\ strength_{no\ H}} * 100 \quad (4)$$

1.2.1. Hydrogen diffusion

Hydrogen diffusion into steel has three stages: physisorption (van der Waals forces between adsorbent and the surface), chemisorption (adsorbent and the surface chemical reaction) and absorption (results of chemisorption go into the lattice). Error! Reference source not found. demonstrates how hydrogen atoms (protons) get absorbed into the metal's lattice [27]. Desorbed hydrogen atoms could turn into molecules. Arrhenius relationship predicts the diffusion coefficient in solids:

$$D = D_0 e^{\frac{-E_A}{KT}} \quad (5)$$

Where D shows the diffusion coefficient ($\frac{m^2}{s}$), D_0 is the maximum diffusion coefficient at absolute temperature ($\frac{m^2}{s}$), E_A is activation energy (J atom^{-1}), T demonstrates the absolute temperature in Kelvin and K shows the Boltzmann constant. Based on Fick's second law: where *x* the average diffusion penetration depth, *k* is a geometry-dependent constant, J denotes the hydrogen flux ($\frac{mol}{s.cm^2}$), ϕ ($\frac{mol}{s.cm}$) is the hydrogen permeation rate, F is Faraday's constant, sample thickness is L (cm) and n shows the transferred electrons.

$$x^2 = kDt \tag{6}$$

$$J = -D\frac{\delta C}{\delta x} \tag{7}$$

$$J = \frac{1}{nF} \qquad so \qquad \phi = JL = \frac{1}{nF}.L \tag{8}$$

1.2.2. Pure iron lattice and hydrogen

The number and size of interstitial sites for FCC and BCC are different. Hydrogen is marginally larger than FCC and BCC interstitials; hence, extra energy is essential for a lattice to accept a hydrogen atom. FCC iron has higher solubility than BCC iron because it has smaller interstitial sites, **Table 3**. Hydrogen typically occupies the octahedral sites due to its larger volume. Hydrogen could dissolve in any metals interstitially at atomic level. It could diffuse quickly in iron and especially in BCC unit cells such as ferrite (α) however, its diffusivity is less in FCC structures such as austenite (γ) and hcp structures as well. Therefore, hydrogen diffusion rate depends on its mobility in the lattice of metals. Martensite also has less hydrogen solubility than austenite but its hydrogen diffusivity (BCC) is higher than FCC structures. Interestingly, the solubility of hydrogen in martensitic AISI-4135 steel is about 0.4wppm, which is substantially more than that for α-iron due to trapping related phenomena [28]. HE in martensitic HSS does not require the concentration of hydrogen to exceed solid solution solubility threshold. Even a very low-hydrogen concentrations would result in HE in martensitic and ferritic structures. Eliaz et al. suggested that local concentrations of hydrogen at microstructural defects are

rather more critical than the average hydrogen content to cause embrittlement of these alloys [29].

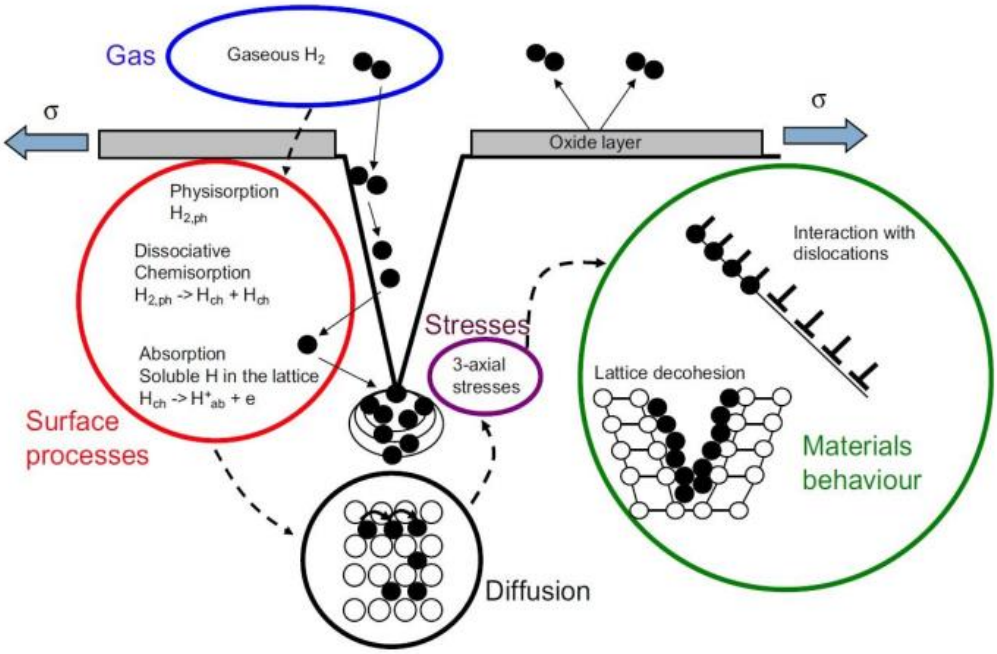

Figure 12. Stages of hydrogen interactions with steel [27]

Table 3: FCC and BCC lattices, number of interstitial sites and atoms in a unit cell [30].

Lattice	Site	Number of sites per Unit Cell	Number of atoms per Unit Cell	β
BCC	Octahedral	6	2	3
BCC	Tetrahedral	12	2	6
FCC	Octahedral	4	4	1
FCC	Tetrahedral	8	4	2

1.2.3. Hydrogen permeation in nanostructured bainitic steels

Hydrogen permeation studies showed that the effective diffusivity of hydrogen for nanostructured bainitic steel was lower than that of mild steel. Transformation temperature and consequent change in the microstructure played a significant role in the hydrogen permeation behavior of nanostructured bainitic steel. BS-200 steel—473.15 K, which exhibited 79 pct (volume fraction) bainitic ferrite, showed lower effective diffusivity of hydrogen than BS-350 steel with 47 pct (volume fraction) bainitic ferrite. Finer microstructural constituents (i.e., bainitic ferrite and retained austenite) and higher dislocation density in the bainitic ferrite of BS-200 steel can be attributed to its lower effective diffusivity of hydrogen as compared to BS-350 steel and mild steel. **Figure 13** shows the hydrogen diffusivity experiments on a mild and two nanostructured bainitic steels by Devanathan–Stachurski permeation cell. **Figure 14** demonstrates various transient curves in a hydrogen permeation of mild steel [31]. As more cycles repeated, more irreversible traps were filled and finally the zoomed area showed some cracks in the sample.

1.3. Hydrogen traps

Heat treatment is defined as controlling the temperature with a certain pattern to increase diffusion rates. This process modifies the steel's properties such as strength, ductility, toughness, hardness and elasticity through reducing the internal stress, reorganizing the alloys element via atomic diffusion, new grain creation and recrystallization, dissolving phases and forming novel phases by precipitation of solid solutions.

Based on the hydrogen binding energy, the traps could be reversible or irreversible[32]. Microstructure has a key role in defining the diffusivity and trapping of hydrogen through the material [33]. For instance, the API X100 steel mobile hydrogen decrease (760-990 MPa tensile strength) could be due to the bainite microstructure, where the bainite lath boundaries acts as hydrogen trap sites [34]. Pearlite/ferrite or bainite microstructures can hold less hydrogen than quenched martensitic structure [35]. Thermal desorption spectroscopy (TDS) is a unique technique which facilitates observing molecules desorption from a surface when the temperature of a surface increases. TDS shows that different carbon contents lead to different amounts of trapped hydrogen. Through microscopy and transmission electron microscopy (TEM) Frappart et al. revealed that the potential hydrogen trap sites in quench and temper HSLA Fe-C-Mo steel are lath and grain boundaries, precipitates and dislocations[36]. Also the apparent diffusivity in HSLA martensitic steel would increase because more dislocation density translates into more hydrogen trap sites [37]. Norena et al. studied a modified 9%Cr - 1%Mo ferritic–martensitic steel (P91) steel with five metallurgical processes subjected to hydrogen permeation test. He discovered that the fine carbide precipitates are the main factor in hydrogen trapping relative to the dislocations in [38]. Crolet defined a critical thickness above which $[H]_{subsurface}$ (subsurface hydrogen concentration) remains constant and the diffusion flux changes in reverse with the thickness. Also below the critical thickness, the $[H]_{subsurface}$ is proportional to the thickness[39]. It is still a challenge to identify the effect of hydrogen at various sites as the tensile strength of a HSS decreases. The effects of thickness and temperature on hydrogen diffusion are captured in **Table 4**.

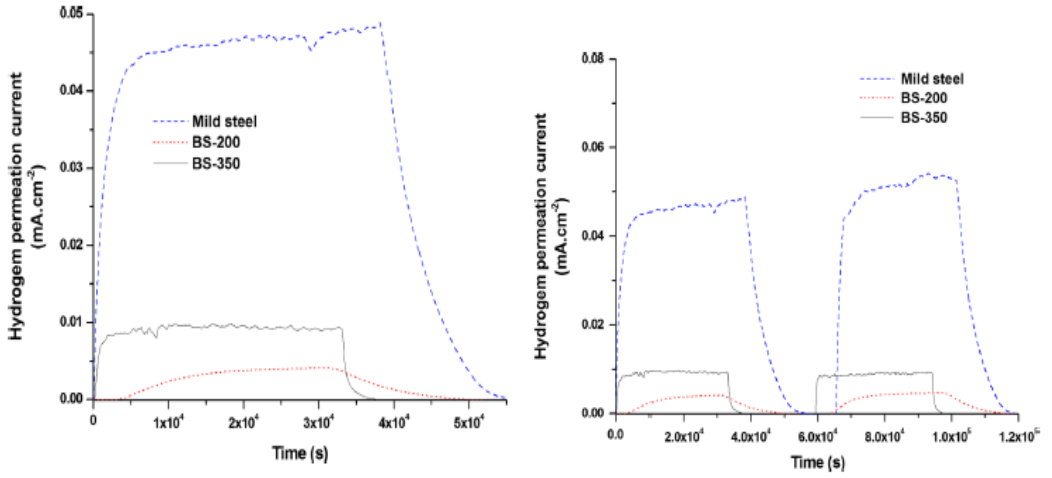

	Mild Steel	BS-200	BS-350
L (cm)	0.05 (±0.005)	0.05 (±0.005)	0.05 (±0.005)
t_b (s)	90 (±30)	3150 (±260)	180 (±30)
I_p (A/cm^2)	4.61×10^{-5} (±0.37)	3.89×10^{-6} (±0.26)	8.89×10^{-6} (±0.01)
J (mol/cm^2 s)	4.78×10^{-14} (±0.3)	4.03×10^{-15} (±0.3)	9.21×10^{-15} (±0.01)
Q (mol/cm s)	2.39×10^{-15} (±0.3)	2.02×10^{-16} (±0.3)	4.61×10^{-16} (±0.01)
D (cm^2/s)	1.82×10^{-6} (±0.20)	5.19×10^{-8} (±0.31)	9.08×10^{-7} (±0.15)

Figure 13. Hydrogen diffusivity experiments on a mild and two nanostructured bainitic steels by Devanathan–Stachurski permeation cell [31].

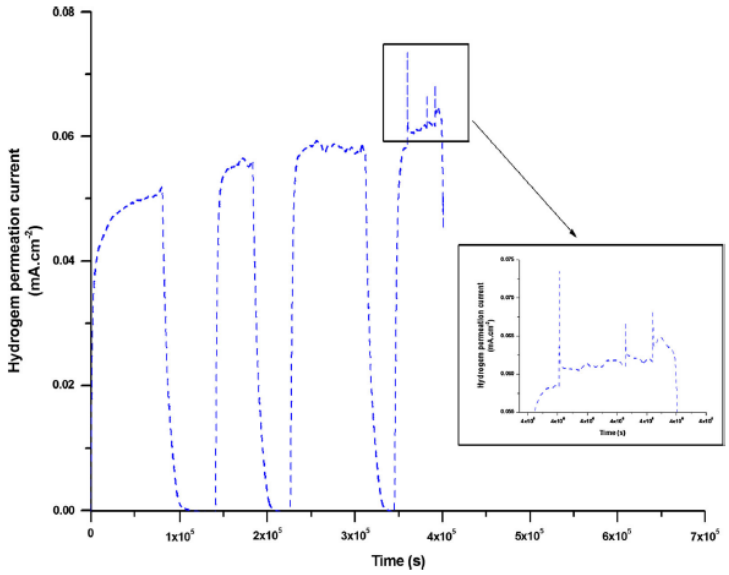

Figure 14. Various transient curves in a hydrogen permeation of mild steel.

Table 4. The effect of thickness and temperature on hydrogen diffusion.

Thickness	Thickness↑	Hydrogen diffusivity↓ [40]
	Thickness↑	Hydrogen diffusivity↑ [41-43]& [42]
	Thickness changes	$[H]_{subsurface}$ ↑↓ and diffusivity↓↑[39]
Temperature	Temperature↑	Hydrogen diffusivity& trapping and apparent solubility↑[41]
	Temperature↑	Steady state permeation current↑ (P91 steel) [38]

If a microstructural element were a trapping site, A, it has a potential or binding energy (E_b) relative to the normal interstitial position, B, in the iron lattice, a trap activation energy (E_t), and saddle point energy (E_s), **Figure 15**.

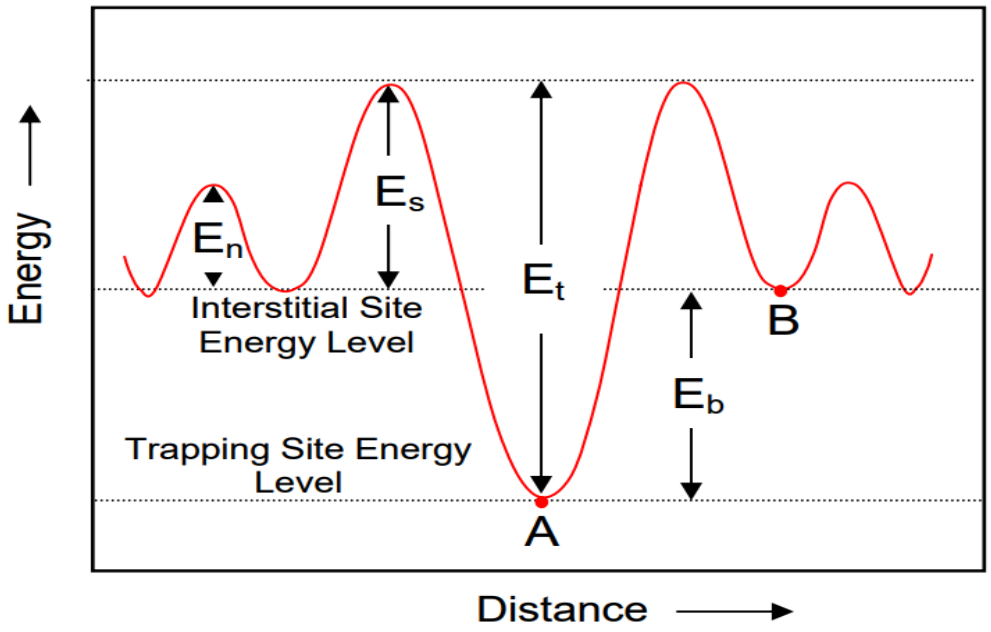

Figure 15. Hydrogen energy levels nearby trapping sites, E_n= hydrogen activation energy of normal lattice site, E_s= Saddle point energy near trapping site, E_t= Energy of trap activation and E_b= Potential well of trapping site [44].

Traps are classified based on how many hydrogen atoms they can accommodate and their binding energy. A reversible trap is when the hydrogen capture and release is sufficiently high to allow match the hydrogen atom relaxation time for a hydrogen atom to diffuse in the metal. Reversible traps have small interaction energy and short residence time, whereas irreversible traps do not release hydrogen without receiving thermal energy and: $|E_t|>>|E_b|$.

1.3.1. Traps in high strength steels

Coherency is the extent of crystallographic match with the lattice of the matrix that governs the interaction energy between traps and hydrogen atoms. For instance, metal carbides (MC), epsilon carbides (a transition Fe carbide with a chemical formula between Fe_2C and Fe_3C), and M_2C have less interaction energy. However, incoherent interfaces (e.g. cementite , Fe_3C) and semi coherent precipitates (metal-carbides) in some HSS have high energies [45]. Frappart et al. generated a list of trap binding energies for a martensitic steel in which the energies range from 0.3 eV to 0.6 eV [36]. The diffusivity for hydrogen in steel is often between 10^{-6}-10^{-7} $\frac{cm^2}{s}$ [46] . Hydrogen sulfide also hinders hydrogen molecule recombination; forcing hydrogen atoms to diffuse to other defects. Furthermore, the diffusion of hydrogen atoms into a metal is additionally dependent on a number of factors such as residual stress, micro-structure, hydrogen concentration gradient, stress gradient, thickness, cracks, non-metallic inclusions, and blisters, grain boundaries and dislocation densities[47].

Li et al. assessed the dislocation binding energy as 58 $\frac{Kj}{mol}$, and mentioned that grain boundaries could be reversible hydrogen traps with analogous binding energies of 59 $\frac{Kj}{mol}$ [48]. Dislocations are also the main hydrogen traps for cold worked AISI-4340. Lee et al. revealed that the activation energies for hydrogen at ferrite-carbide interfaces, micro-voids, and dislocations of AISI-4340 HSS were about 48.3 $\frac{Kj}{mol}$, implying the existence of reversible or relatively low energy traps[44]. They proposed that alloying elements and the cold work intensity raises the concentration of dissolved hydrogen in AISI-4340 HSS if introducing further traps exist in the microstructure by enhancing dislocation density. Also, high pressure built at small inclusions are due to a ductile fracture. At the interface of high sulfide saturated inclusions also, micro-voids form because of the embrittlement of AISI-4340 HSS by hydrogen. Type of heat treatments, alloying involved in elements, cold work and hydrogen sources impact trapping. Each alloy composition of HSS determine the traps characteristics.

1.3.2. Impacts of trapping on hydrogen diffusion

Hydrogen diffusion in the nonexistence of traps, results in the ideal lattice diffusivity definition, (D_L), administered by lattice migration energy between interstitial sites (E_n). D_H demonstrates the trap affected or apparent diffusivity, 3 orders of magnitude less than D_L, depending on the traps nature:

$$\frac{D_L}{D_H} = 1 + \frac{Nk}{p} \tag{9}$$

Trapped hydrogen must acquire a substantially larger energy level than the lattice migration energy to be able to escape the trap, **Figure 15**. Therefore, the diffusing

hydrogen atom mean residence time is noticeably longer in the trap than the lattice, thus the lattice diffusivity is higher than apparent diffusivity lower [30].

At a lattice with presumably only irreversible traps, the hydrogen charging diffusivity declines to D_H until the traps get saturated. Owing to no interaction between the irreversible traps and the dissolved hydrogen in lattice, diffusivity surges back to $D_{L.}$ In reversible traps, however, there is an ongoing equilibrium among dissolved hydrogen in the lattice and hydrogen; therefore, in a lattice with reversible traps $D_L > D_{H.}$

1.3.3. Impacts of trapping on hydrogen embrittlement

Trapped hydrogen, unlike diffusible hydrogen, does not cause HE in low alloy steels. In fact, low-binding-energy reversible traps are ideal for hydrogens that diffuse to lower hydrogen chemical potential (e.g. crack tip). Additionally low energy traps reduce the threshold intensity stress with increasing hydrogen concentration in HSS leading to HE [49]. Heterogeneities type determine the degree of HE susceptibility of HSS. Pound concluded that larger irreversible traps (high binding energy) usually cause more susceptibility [45].

1.4. Hydrogen pressure theory

Pressure theory is one of the first proposed mechanisms for failure due to hydrogen for high fugacity charging situations. After hydrogen molecule formation (H_2), pressure would increase, initiating voids and crack growth. Hydrogen transport by dislocations would increase the internal pressures in the voids even at low external pressure and fugacities. To study the fracturing phenomenon, it is vital to assess the crack tip stresses,

observe how plastic deformation of such stresses caused and finally project how the produced deformations would trigger ensuing crack growth.

Through quenching from high temperature and cathodic charging, researchers produced some micro-cracks in high purity iron-three percent silicon single crystals. Once a crystal is cracked under the stress, σ, researchers observed high stresses at the crack tip. If these stresses are applied for a sufficiently long period, they would trigger plastic deformation where D is the crack length, γ_s denotes the crystal's reversible energy, γ_p is the energy expanded by plastic deformation and E is the elastic modulus of the crystal.

$$\sigma \leq \sqrt{\frac{\pi E(\gamma_s + \gamma_p)}{L(1-\upsilon)}} \tag{10}$$

To identify γ_p, a Griffith penny-shaped crack with the diameter of L spreads once the internal pressure is P is reached. In the below equation, γ_s is the crystal's surface energy and the plastic work done due to crack propagation is γ_p.

$$\mathrm{P} = \sqrt{\frac{\pi E(\gamma_s + \gamma_p)}{L(1-\upsilon)}} \tag{11}$$

The stationary crack with L_0 length has a more blunted tip relative to a quick propagating crack. The required internal pressure (P_t) to re-initiate the crack propagation is larger than P shown in the above equation to retain the crack in motion ($P_t > P$). $\Delta\gamma$ shows the plastic relaxation due to slowed down or stopped crack.

$$\mathrm{P_t} = \sqrt{\frac{\pi E(\gamma_s + \gamma_p + \Delta\gamma)}{L_0(1-\upsilon)}} \tag{12}$$

$$\Delta P = \mathrm{P_t} - \mathrm{P} = \sqrt{\frac{\pi E\left(\gamma_s + \gamma_p + \Delta\gamma\right)}{L_0(1-\upsilon)}} - \sqrt{\frac{\pi E\left(\gamma_s + \gamma_p\right)}{L_0(1-\upsilon)}} \quad (L = L_0) \tag{13}$$

When the crack resumes propagating, a cleavage could form provided it moves sufficiently quickly to hinder plastic relaxation at the tip. We have the below relation for constant internal pressure P_t

$$P + \Delta P = \mathrm{P_t} > \sqrt{\frac{\pi E\left(\gamma_s + \gamma_p + \Delta\gamma\right)}{L_0(1-\upsilon)}} - \sqrt{\frac{\pi E\left(\gamma_s + \gamma_p\right)}{L(1-\upsilon)}} \quad (L > L_0) \tag{14}$$

The hydrogen pressure, however, is not kept constant during the crack growth because the atoms of hydrogen are unable to reach the crack surface quick enough. The hydrogen pressure depends on hydrogen atoms diffusing out of the lattice to the crack surface and form H_2. Crack growth would arrest if the pressure goes below P. Once sufficient hydrogen is available to raise the pressure in the crack again crack growth resumes. As a result, this process occurs discontinuously[50].

1.5. Hydrogen embrittlement mechanisms

1.5.1. Adsorption induced dislocation emission (AIDE)

AIDE is one of the most complex HE mechanisms which involves dislocation movement and nucleation[51]. In this mechanism, adsorbed hydrogen to on a metal surface enables the emission of dislocation from a crack tip by reducing the stress for the nucleation dislocation [52]. Adsorbed hydrogen dwindles the intermetallic bonds and provides the nucleation sites for of dislocations near the surface and at the plastic region.

On one hand, back-stresses due to the dislocation emission prevents creation of more dislocations, On the other hand, formation of micro-voids ahead of crack tip occur at slip band intersections or at a second-phase particle. Similarly, the diffusible pre-existing hydrogen in the metal migrates to the tip of the cracks and voids along dislocation planes whereas it can adsorb at the crack-tip[51]. Consequent to crack propagation, crack tip would be blunter and further crack propagation decelerates. However, merging the blunt crack tip and voids will sharpen the crack tip and therefore accelerate the crack propagation again. Micro-void coalescence (MVC) implies voids growth due to hydrogen adsorption, **Figure 16**. The detection of large dimples would be difficult and MVC creates small dimples in larger dimples leading to inter-granular and trans-granular fractions [5], [12].

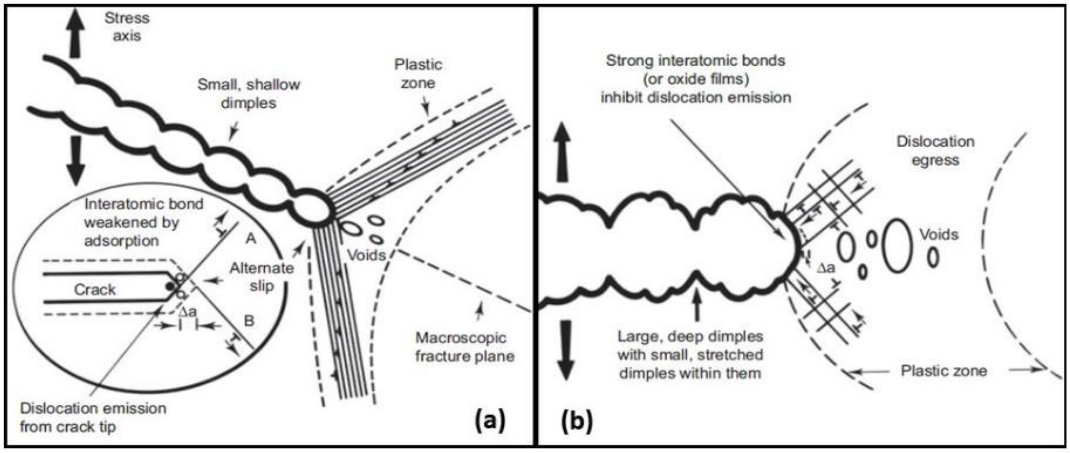

Figure 16. Crack propagation in a) an AIDE mechanism b) a MVC mechanism [51].

Dislocation nucleation occurs due to the lattice's weakened interatomic bonds, less stacking fault energy and the steels' softened elastic moduli. A main weakness in AIDE's

mechanism is the dominance of near-surface hydrogen adsorption in HE [52]. In addition, the slip structure around the a crack tip was not characterized adequately to illustrate hydrogen driven dislocation emission and geometric crack extension[49]. Furthermore, high strength polycrystalline alloys have some intrinsic barriers preventing dislocation movements, AIDE might not ensue. Finally, this mechanism does not explain the predominantly observed inter-granular cracking.

1.5.2. Hydrogen-enhanced decohesion (HEDE)

This model is one of the initial models, proposing that adsorbed hydrogen would be make the interatomic forces weaker and subsequently cause a crack. In this model, the hydrogen atoms electrons fill the metals' d band, and diminish the cubic cleavage planes cohesive strength [53]. Once the elastic tensile force perpendicular to the crack's plane equates the local highest cohesive force per unit area, a crack would initiate. Hydrogen solubility surges in the presence of a tensile force for instance at the crack tip. Troiano also believed that HE reduces the cohesive strength of the lattice of metals [54].

Molecular orbital simulations conducted based on models of Fe-Fe and Fe-H pair potentials, as well as Fe-H atom clusters assisted understanding the fundamentals of hydrogen effects on decohesion. Effort made by Gerberich et al. revealed that the tensile forces nearby the crack tip is approximately 2.9×10^6. Such forces are adequate to form a high local concentration of hydrogen [55].

HE of high strength steels depends on the impacts of local high hydrogen concentrations on the cohesive energy of the iron lattice. Interstitial lattice sites would stimulate an inter-granular fracture, if decohesion alongside slip planes occurs due to

diffusible hydrogen accumulation. However it is arguable if through strain hardening the sufficient elastic strain could be accomplished[51]. Impurities as well as diffusible and trapped hydrogen in grain boundaries could cause decohesion. On the other hand, if decohesion happens in grain boundaries, a trans-granular fracture could grow. Additionally, a hydrogen source could summon decohesion at the atomically sharp crack tip. **Figure 17** shows the HEDE mechanism happening at three sites: (a) hydrogen in the lattice, (b) adsorbed hydrogen at the crack-tip, (c) hydrogen in particle-matrix interfaces. The dots symbolize hydrogen atoms and the circles are metal atoms.

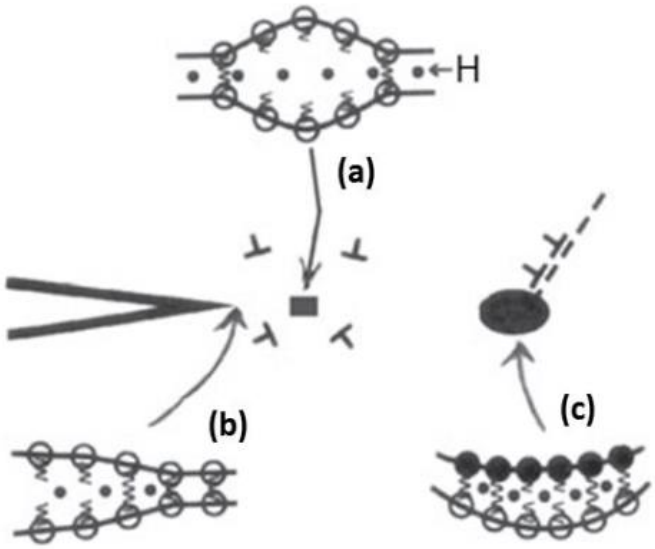

Figure 17. HEDE mechanism weakens the metallic bonds [51].

1.5.3. Hydrogen-enhanced localized plasticity (HELP)

Beachem detected dimples on the surface of fractures created due to HE and proposed that hydrogen unlocks dislocations[56]. Ferreira et al. believed that hydrogen effects on the dynamics of dislocation and mentioned that hydrogen helps dislocation to increase or

transport at reduced lower stresses[57]. Sirois & Birnbaum suggested that hydrogen shapes an atmosphere near dislocations and elastic stress regions[58]. Hydrogen atmospheres rearrangement protects the dislocation from the elastic center and plummets the interaction energy between the obstacle and the dislocations. Thus, dislocations would be able to transport with less stress level. Higher concentration of hydrogen would yield to less stress requirement to move an edge dislocation. HSS exposed to high hydrogen concentrations would mainly follow the decohesion mechanism, however, low strength steels with small hydrogen amounts, favors HELP, **Figure 18**. This model reveals that because of hydrostatic stresses in the material can diffusible hydrogen reach high localized concentrations in stress zones, like crack-tips[59, 60]. Hydrogen also diminishes the energy of stacking fault, allowing for an increase in separation distance of Shockley partial dislocations[57, 61]**.**

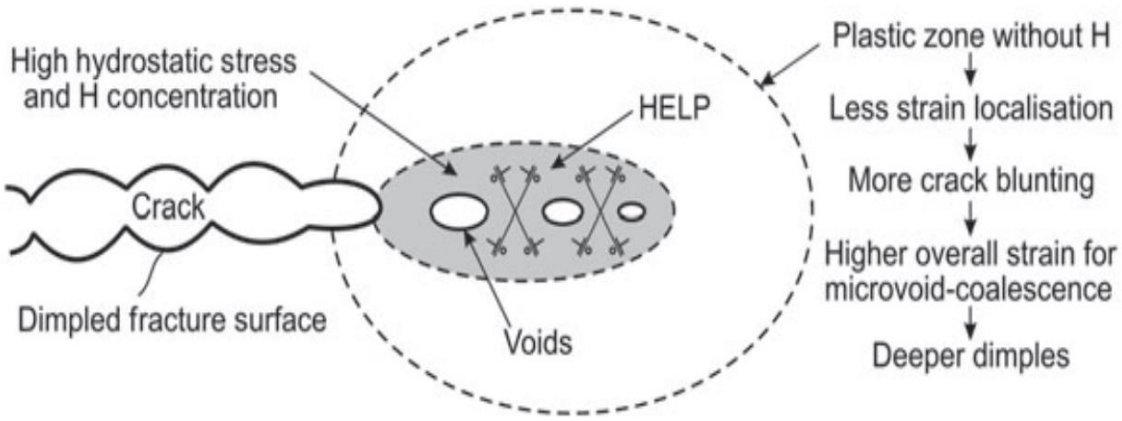

Figure 18. HELP mechanism, involving a MVC process inside the localized plasticity zone [51].

1.5.4. Combinations of mechanisms

Hydrogen causes HE by growing a subcritical fracture. Once hydrogen adsorbed at a crack-tip, dislocations nucleation starts at surface and progress into the material because of hydrogen accumulation. Adsorption induced dislocation emission and Hydrogen-enhanced localized plasticity mechanisms would reduce the back-stress and help the nucleation of more dislocations and MVC. The MVC primarily caused by the AIDE, in slip-plane intersections could be also explained by either HELP or in interstitial sites by HEDE. Decohesion production explained by HEDE could be similar to a crack-tip sharpener, permitting the emission of dislocation in the AIDE mechanism interact with the sharp crack-tip. It is however difficult to explain exactly which mechanism or combinations of them are behind HE. **Figure 19** demonstrates a combination of HE mechanisms.

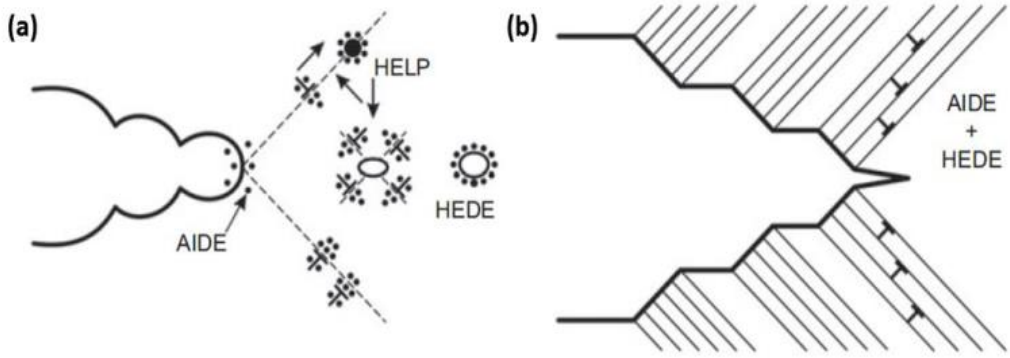

Figure 19. a) AIDE mechanism promoted by HELP and HEDE plus MVC. b) AIDE and HEDE [51].

1.6. High strength steel microstructure and hydrogen embrittlement

High strength steel advancements originated in 1960's for naval applications by ferrite pearlite steels. Hydrogen embrittlement is a serious challenge for several applications including automotive. In hydrogen vehicles, for example, hydrogen could be stored at 10ksi. Tensile tests is the first approach to evaluate the susceptibility of HSS to HE. Michler and Naumann researched the susceptibility of ferritic, pearlitic, bainitic and martensitic samples by tensile testing exposed to hydrogen in gas phase (1450 psi) at room temperature [27]. The could not define a primary parameter for HE however they observed precipitation vulnerable grade as the only sample with minimal macroscopic ductility loss proposing that irreversible traps could be successful means to minimize the vulnerability of bcc steels to HE.

1.7. HE in martensitic high strength steels

Austenizing is defined as cooling to room's temperature very quickly to transform austenite to martensite and consequently yielding martensitic steels. For steels with up to 0.6% carbon, the lath martensite would form, and on the contrary, for steels with carbon percentage above one percent, plate martensite would be produced. Austenite (γ-Fe), the Iron's FCC structured solid solution, transforms to strained-body-centered tetragonal highly carbon saturated form named Martensite. Quenching rate below the critical cooling threshold results in the perlite formation commencing at the grain boundaries. The HSS studies in this report have analogous microstructures after quenching, though cooling results in the formation of different microstructures.

At the as-quenched state 0.4 % CLAS is mainly lath martensite with almost 5% retained austenite dispersed as narrow films amid martensite laths, at packet boundaries and along prior austenite grain boundaries. The mechanical stability of retained austenite under as-quenched state is low. Due to this reason, 4340 for instance, is tempered at 200°C to intensify the retained austenite mechanical stability for high strengths steel purposes. Researchers invested time in making advanced HSS in hydrogen-saturated environments resistant to HE by increasing their strength [62]. Increasing carbides leads to the formation of more robust trapping sites, which diminishes the mobility hydrogen[63].

1.8. Alloying and microstructure impacts of hydrogen embrittlement

Alloying elements expectedly have a great effect of HSS properties, which ultimately determine steels susceptibility to HE. Main factors such as microstructure, grain size and carbide precipitations not only lead to different HE resistance but also they will impact the hydrogen diffusion coefficient[64]. HE causes a significant damage to high strength steels because of hydrogen diffusion. HSLA and Cu containing low carbon steels are evolving for naval applications due to hand in hand high toughness and strength and proper weldability. Less carbon concentration improves the weldability and adding of copper contribute to strength by ageing. Meanwhile each heat treatment method lead to a specific toughness and strength. Thermo-mechanical controlled process and accelerated controlled cooling are used to optimize the microstructural properties. Vanadium (V), titanium (Ti), niobium (Nb) are critical to mechanical properties of HSS and nickel (Ni), copper (Cu), molybdenum (Mo), chromium (Cr) enhances its hardness, toughness and strength for specific application. Takai et al. studied the fracture surface of medium-1400 $\frac{N}{mm^2}$-tensile-

strength carbon steels and investigated the influence of adding Si and Ca on delaying fracture. Through fractography, they revealed that addition of 0.5% Si did not change inter-granular fracture area fraction, however, addition of 1.5% Si and 30ppm Ca delayed the fracture the most [65].

1.9. Microstructural phases: retained austenite, cementite and ε-carbide as a trap

Retained or reverted austenite boost the hydrogen embrittlement. Martensitic carbon steels traps the majority of hydrogen at the as quenched state. Raising the tempering temperature lowers the hydrogen trapping ability. Raising the carbon content translates into higher hydrogen capacity for tempered and as-quenched states. In martensitic steels, dislocation are the main traps. Since retained austenite traps hydrogen in an irreversible manner, it raises the solubility of hydrogen and reduces the diffusivity [66]. Microstructural element of high strength steels could play a very important role in trapping process.

- Hydrogen solubility is high in retained austenite.
- γ/α interface is a strong trap.
- Martensite could contain the hydrogen concentration of the austenite.
- Retained austenite lowers the total diffusivity and permeability of hydrogen in steel and provided austenite surrounds ferrite, hydrogen mobility will significantly diminish.
- Higher binding energy for Hydrogen atom trapping at M_2C should reduce the internal hydrogen embrittlement susceptibility of an UHHS such as AERMET 100.

- The interfaces between ferrite- Cementite demonstrate ineffective hydrogen traps.
- ε-carbide is a transition iron carbide between Fe_2C and Fe_3C which counts as an effective trap for hydrogen in fact better than cementite. Comparing to Fe_3C, ε-carbide is also not thermodynamically stable, and essentially forms first because of this coherency, which diminishes the nucleation activation energy [67, 68].

Yield strength and impurities of the martensitic high strength steels could significantly affect the resistance to hydrogen embrittlement. The influence of martensite type, prior austenite grain size, and its mechanical stability, morphology and amount should be further researched.

1.10. Fractography

Field Emission Scanning Electron Microscope (FESEM) and Transmission Electron Microscopy (TEM) research along with studies on metallographic cracks, demonstrated that a crack occurrence consists of nucleation, growth, and coalescence of voids, leading to creation of dimples on fracture surfaces, with a variety of sizes (10^{-3} m -10^{-7} m) and shapes dependent on the state of stress, type of material, microstructural feature and composition and temperature. Dimple have different shapes under shear stress. Dimples could point in a same direction (tear dimples) or in opposite directions (shear dimples) or get stretched due to plasticity behind crack tips [52].

Robertson et al. utilized a modified TEM to executed deformation experimentations. They applied hydrogen pressures about 20 kPa and revealed that regardless of the material and dislocation type, hydrogen gas increased the dislocation velocity and eliminating it

from TEM ceased the dislocations motion or any crack propagation. This process, however, depends on the purity of the material purity and hydrogen gas pressure [69]. Michalska et al. conducted quantitative fractography on 2205 duplex stainless steel and proved that this approach could reveal a valuable information about the influence of hydrogen embrittlement of duplex steels in addition to mechanical properties. **Figure 20** demonstrates the application of quantitative fractography. It manifests how a ductile fracture surface area with no exposure to hydrogen would transform to a more brittle fracture surface when charged with hydrogen [70].

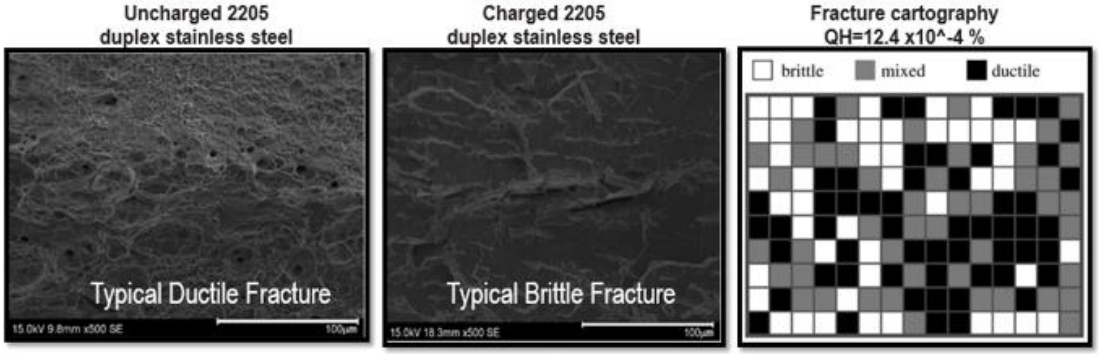

Figure 20. Application of quantitative fractography in the assessment of hydrogen damage of duplex stainless steel [70].

1.11. Nickel Plating for Hydrogen Permeation

Electroplating is an inexpensive way of depositing a thin film on conductive substrates without damaging the substrates. For hydrogen permeation studies, the steel get plated with nickel to prevent oxide layer formation, which could interfere with hydrogen diffusion. The following procedures could be followed to conduct the nickel plating.

1. The steel of varying thickness are to be ground with SiC paper up to 600 grits.

2. Wash sample with distilled water, and ultrasonically clean in acetone and ethanol.
3. One side of the steel sample should be plated with nickel in a Watt's bath containing $NiSO_4$* $6H_2O$ 250 g/l, $NiCl_2$*$6H_2O$ 45 g/l, and H_3BO_3 40 g/l at 333.15 K (60 ̊C). The following procedures will be used to plate one side of the steel. The solution was made using the chemical ratios and was stirred for 30 min to homogenize the solution.
4. Obtain the membrane used for the experiment and place it on top of another arbitrary steel sample.
5. Obtain a glass cylinder and place it on top of the sample.
6. Use the U-shaped clamp to fix the steel membrane on top of the arbitrary sample.
7. Add adequate solution into the cylinder apparatus and submerge the platinum electrode, **Figure 21**.

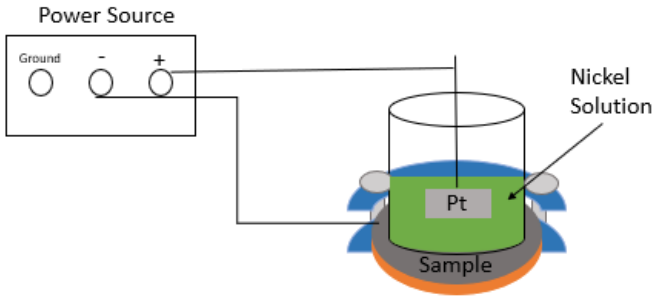

Figure 21. Watt's bath configuration used for nickel plating.

8. The Pt will be connected to the positive terminal and the specimen will be connected to the negative terminal of the power source.
9. The nickel plating will be carried out using a current density of 3 mA/cm^2 for 180 seconds.
10. Rinse the sample with DI water.

The Nickel electroplating solutions may cause sensitization by skin contact. Avoid breathing the vapors of the plating solutions and compounds. The usage of gas masks and chemical gloves is strongly recommended. Goggles for eye care should always be worn.

2. CHARACTERIZATION OF NANOSTRUCTURED BAINITIC STEEL

Nanostructured steel is manufactured by proprietary catalysts including additives such as Niobium, Vanadium, or Aluminum in the smelting process. Conventionally, the addition of such elements, along with hardening and tempering methods enhance the hardness and strength of steel by forming grain sizes which are finer than fine austenitic grain size. In the contrary, nanostructured bainitic high strength steel, due to its ultra-fine grain size, not only retain the ductility typical of lower strength steel formulations, but also achieve a much higher strength, hardness, and toughness typical of traditional high strength steels.

Mechanical properties behavior of such steels and their response to simple heat treatment, may not be explained purely by chemical composition. While grain size does not diminish the significance of chemical composition of steel, it immensely impacts the mechanical performance. Grain size could influence yield strength, elongation, impact strength at a given hardness, machinability, and the ability of high strength steels to be plastically deformed.

Nanostructured bainitic steel has high hardness, elastoplastic deformation and elongation leading to a very high toughness combined with high ductility. Similar high strength steels with similar properties require more complex chemistry in addition to hardening and tempering to deliver similar performance. Such methods, however, could compromise ductility and elongation for higher hardness and elastic modulus, which often yield to moderate to high brittleness.

Discovering the relationships between the ductility and microstructural parameters influencing the strength and of bainitic high strength microstructures is essential to further development of 3rd generation high strength steels. The intricacy of microscopically analyzing such a microstructure goes beyond solely recognizing the existence of two phases, bainitic ferrite and retained austenite. However, collecting data such as hardness and reduced elastic modulus microscopically would add value to understand the mechanical properties of such a material better. This research encompasses data from microstructural properties to strength, and ductility. Literature demonstrating qualitative and quantitative results reveal a strong correlation among tensile strength, hardness, and grain size for various metals and ceramic crystalline structures.

Table 5. Grain size relationships - equiaxed grains, uniform and randomly oriented [71].

Grain Size No.	$\bar{N}_A$ Grains/Unit Area		$\bar{A}$ Average Grain Area		$\bar{d}$ Average Diameter		$\bar{\ell}$ Mean Intercept		$\bar{N}_L$
G	No./in.^{2} at 100X	No./mm^2 at 1X	mm^2	μm^2	mm	μm	mm	μm	No./mm
00	0.25	3.88	0.2581	258064	0.5080	508.0	0.4525	452.5	2.21
0	0.50	7.75	0.1290	129032	0.3592	359.2	0.3200	320.0	3.12
0.5	0.71	10.96	0.0912	91239	0.3021	302.1	0.2691	269.1	3.72
1.0	1.00	15.50	0.0645	64516	0.2540	254.0	0.2263	226.3	4.42
1.5	1.41	21.92	0.0456	45620	0.2136	213.6	0.1903	190.3	5.26
2.0	2.00	31.00	0.0323	32258	0.1796	179.6	0.1600	160.0	6.25
2.5	2.83	43.84	0.0228	22810	0.1510	151.0	0.1345	134.5	7.43
3.0	4.00	62.00	0.0161	16129	0.1270	127.0	0.1131	113.1	8.84
3.5	5.66	87.68	0.0114	11405	0.1068	106.8	0.0951	95.1	10.51
4.0	8.00	124.00	0.00806	8065	0.0898	89.8	0.0800	80.0	12.50
4.5	11.31	175.36	0.00570	5703	0.0755	75.5	0.0673	67.3	14.87
5.0	16.00	248.00	0.00403	4032	0.0635	63.5	0.0566	56.6	17.68
5.5	22.63	350.73	0.00285	2851	0.0534	53.4	0.0476	47.6	21.02
6.0	32.00	496.00	0.00202	2016	0.0449	44.9	0.0400	40.0	25.00
6.5	45.25	701.45	0.00143	1426	0.0378	37.8	0.0336	33.6	29.73
7.0	64.00	992.00	0.00101	1008	0.0318	31.8	0.0283	28.3	35.36
7.5	90.51	1402.9	0.00071	713	0.0267	26.7	0.0238	23.8	42.04
8.0	128.00	1984.0	0.00050	504	0.0225	22.5	0.0200	20.0	50.00
8.5	181.02	2805.8	0.00036	356	0.0189	18.9	0.0168	16.8	59.46
9.0	256.00	3968.0	0.00025	252	0.0159	15.9	0.0141	14.1	70.71
9.5	362.04	5611.6	0.00018	178	0.0133	13.3	0.0119	11.9	84.09
10.0	512.00	7936.0	0.00013	126	0.0112	11.2	0.0100	10.0	100.0
10.5	724.08	11223.2	0.000089	89.1	0.0094	9.4	0.0084	8.4	118.9
11.0	1024.00	15872.0	0.000063	63.0	0.0079	7.9	0.0071	7.1	141.4
11.5	1448.15	22446.4	0.000045	44.6	0.0067	6.7	0.0060	5.9	168.2
12.0	2048.00	31744.1	0.000032	31.5	0.0056	5.6	0.0050	5.0	200.0
12.5	2896.31	44892.9	0.000022	22.3	0.0047	4.7	0.0042	4.2	237.8
13.0	4096.00	63488.1	0.000016	15.8	0.0040	4.0	0.0035	3.5	282.8
13.5	5792.62	89785.8	0.000011	11.1	0.0033	3.3	0.0030	3.0	336.4
14.0	8192.00	126976.3	0.000008	7.9	0.0028	2.8	0.0025	2.5	400.0

The standard test methods to determine average grain size is issued under the fixed designation E112, **Table 10**. This standard was also approved for use by agencies of the US Department of Defense. It is known that the numbered fracture grain size series is in consensus with the correspondingly numbered ASTM grain sizes, Error! Reference source n ot found. . The smallest average diameter is shown group size no.14 and 2.8μm.

2.1 Microstructural characterization

Isothermal transformation at low temperatures (125–325 C) paved the path to make lower bainitic nanostructured steels. The development process is relatively challenging and it suggests the application of the detailed phase transformation theory and metallurgical facts [23, 72, 73]. The nanostructured bainitic steels, studied in this research, include ultrafine bainitic ferrite plates along with retained austenite as a dispersed second phase. Retained austenite shows two unique morphologies, either resembling thin films between the plates of ferrite (nano-size), and blocks separating bainitic sheaves defined as groups of bainitic ferrite plates having a common crystallographic orientation. This diverse microstructure, with a robust composite character, provides an outstanding balance of mechanical properties[74, 75]. Strength of the nanostructured bainitic high strength steels mainly stems from the contribution the ferritic matrix (high fraction of thin bainitic ferrite plates). Moreover, this class of steel provides great ductility by the amount and nature of retained austenite [74, 76, 77], a ductile phase compared to bainitic ferrite.

We utilized X-ray powder diffraction and verified the existence of austenite and bainitic ferrite in the microstructure of nanostructured steels. We polished and etched the metallographic nanostructured bainitic steel specimens with two volume percent nital

solution. Subsequently we used scanning electron microscope to discover the microstructures, **Figure 23**, **Figure 25** and **Figure 28**. One of the most important factors in analyzing the nanostructured bainitic steels is austenite content and its morphology. Atomic force spectroscopy (AFM) was subsequently used to confirm the SEM images and capture the features of these nanostructured bainitic steel microstructures.

We used a tip of 10 nm to reveal the finest features. **Figure 22**, **Figure 24**, **Figure 26** and **Figure 27**show all the three microstructures in 2D and 3D. The 1000 MPa, 1300 MPa, 1600 MPa and 2000 MPa steels have 39 percent, 55 percent, 68 percent and 73 percent retained austenite. The 2000 MPa micrograph clearly illustrates very fine and thin needle-shaped bainitic sheaves structures along with islands of austenitic microfilms and blocks. The 1300 MPa and 1000 MPa steels both have granular shaped austenitic blocks larger than the ones in 2000 MPa steel. The 1300 MPa austenitic blocks are relatively smaller and more connected than the 1000 MPa steel. The color bar represents the elevation topography in nm. The gold colored features represent the austenitic phase spread either as granular islands of blocks or thin films. The brown regions, on the other hand, refers to the bainitic ferrite phase. AFM images shows a better austenitic phase distributions in all microstructures and evidently reveal the size of austenitic and bainitic grain size quantified by the Bruker software (NanoScope 1.8) and line method. All microstructures seem to have the average bainitic-ferrite grain size of 35±3nm, while their austenitic grain size and morphology vary between 200±5nm to 3±0.5μm. Mean free path, defined as an area composed of bainitic ferrite in 1000 Mpa, 1300 Mpa and 2000 Mpa nanostructured bainitic steel were quantified as 8.95, 5.71, 4.1 μm^{-2} respectively.

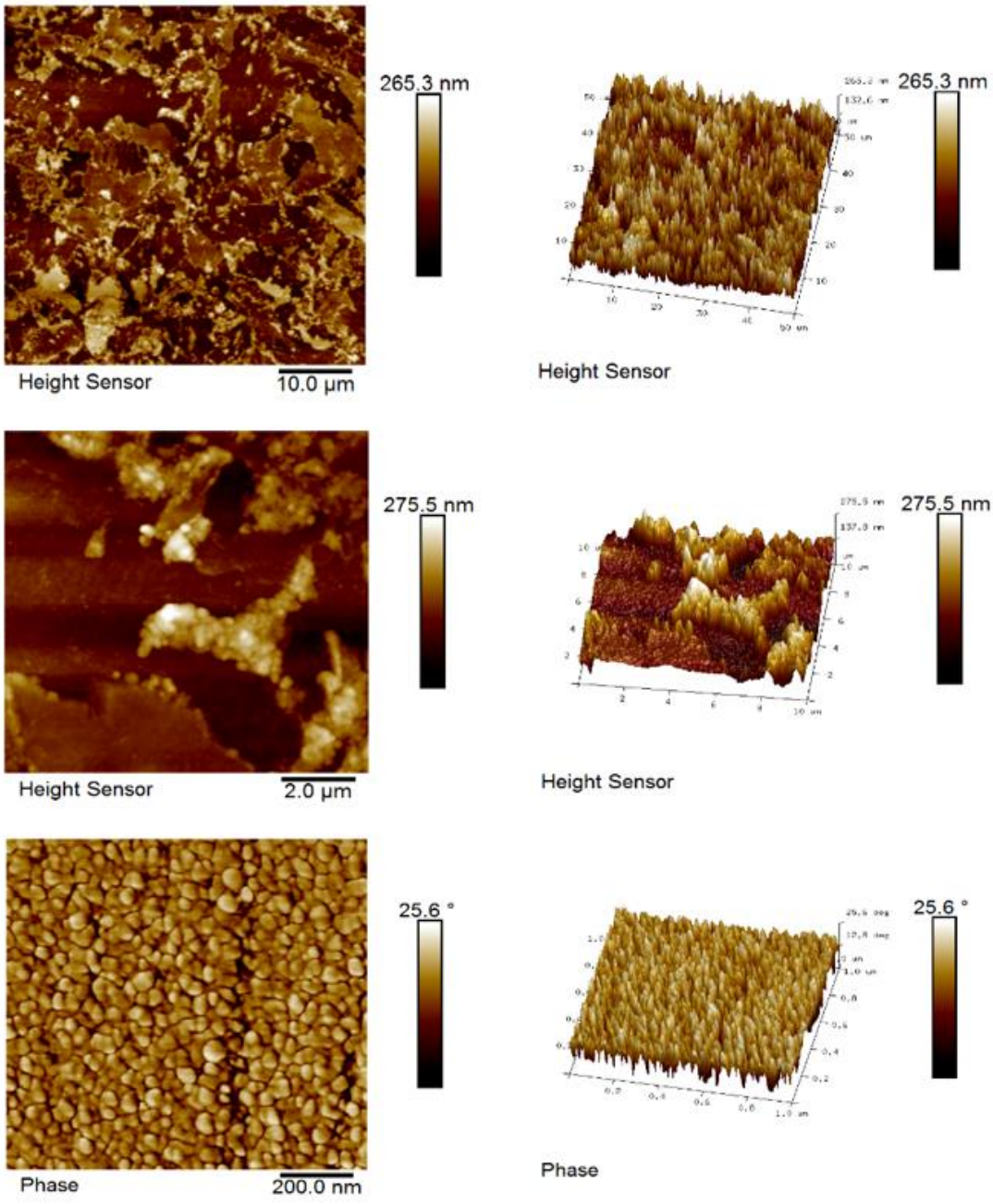

Figure 22. 1000 MPa nanostructured steel captured by AFM.

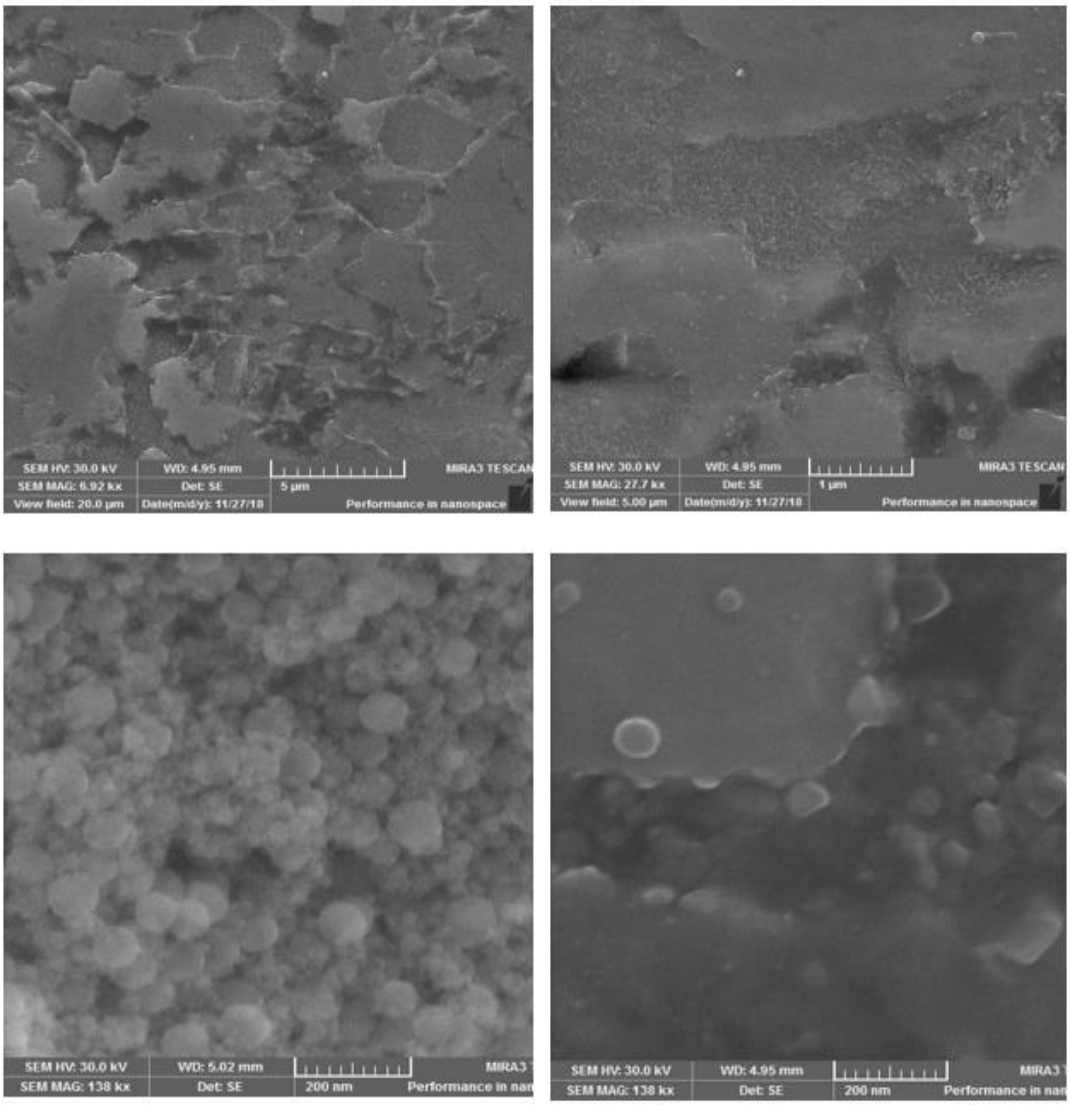

Figure 23. Microstructure of the 1000 MPa nanostructure high strength steel.

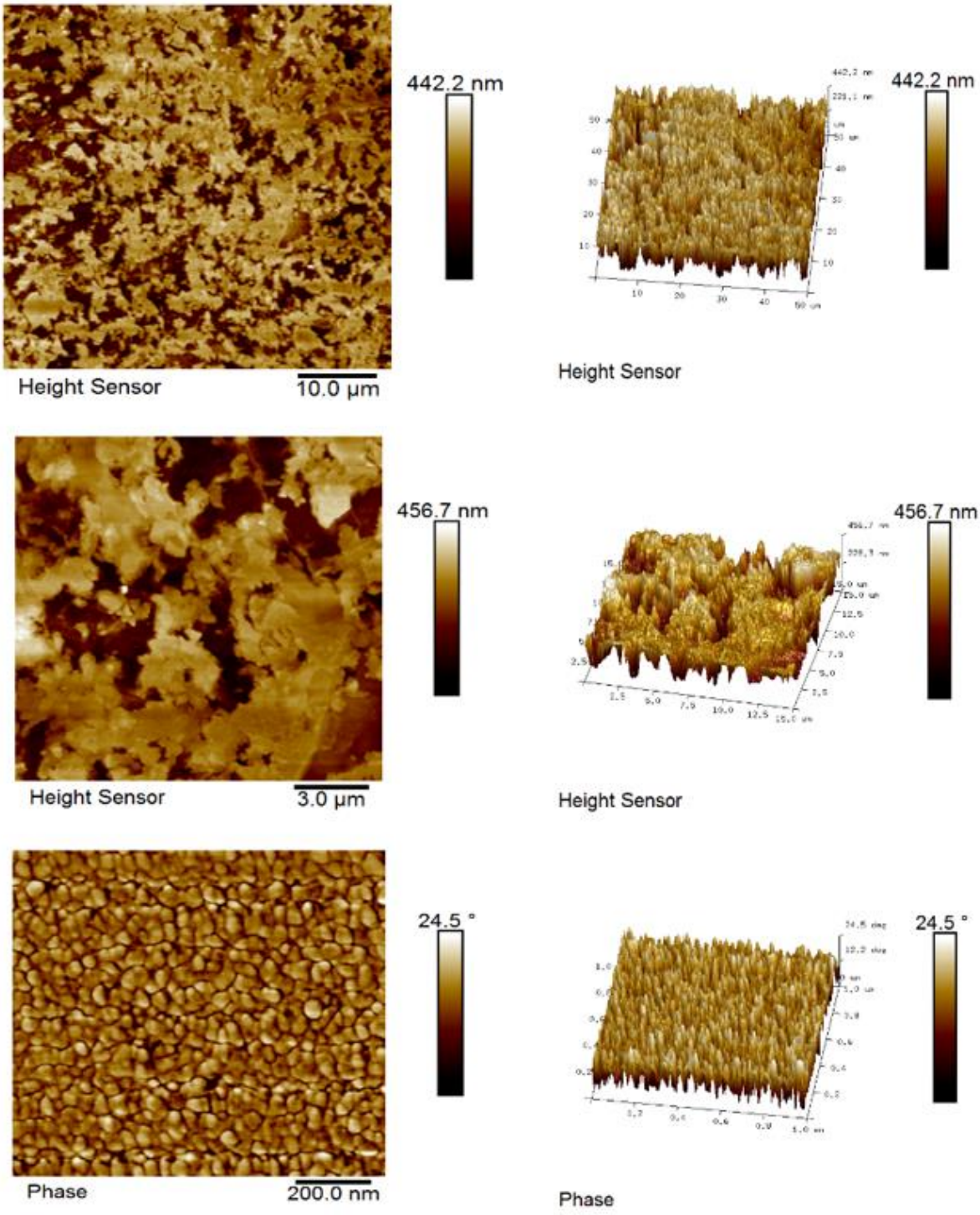

Figure 24. 1300 MPa nanostructured steel captured by AFM.

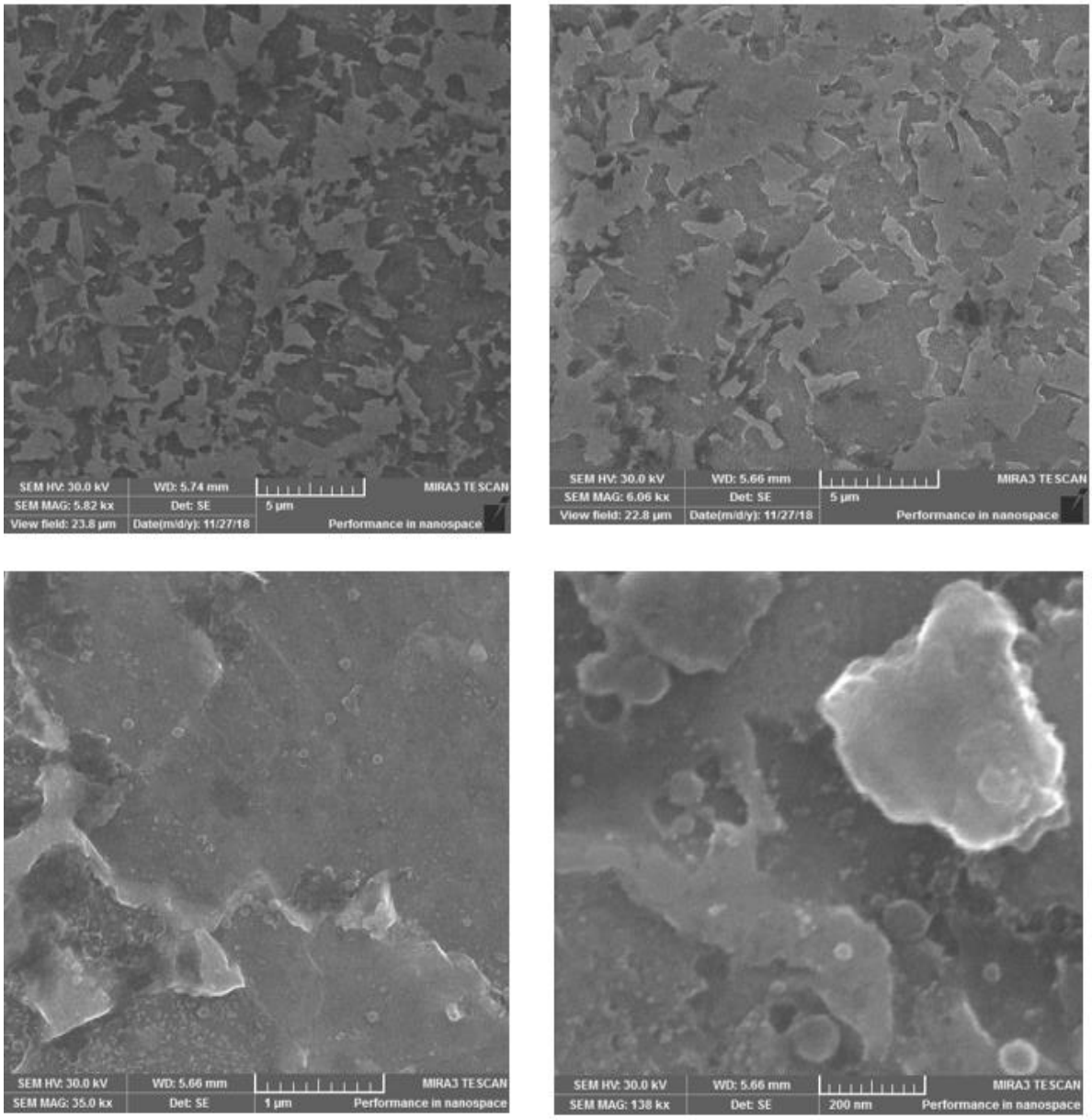

Figure 25. Microstructure of the 1300 MPa nanostructure high strength steel.

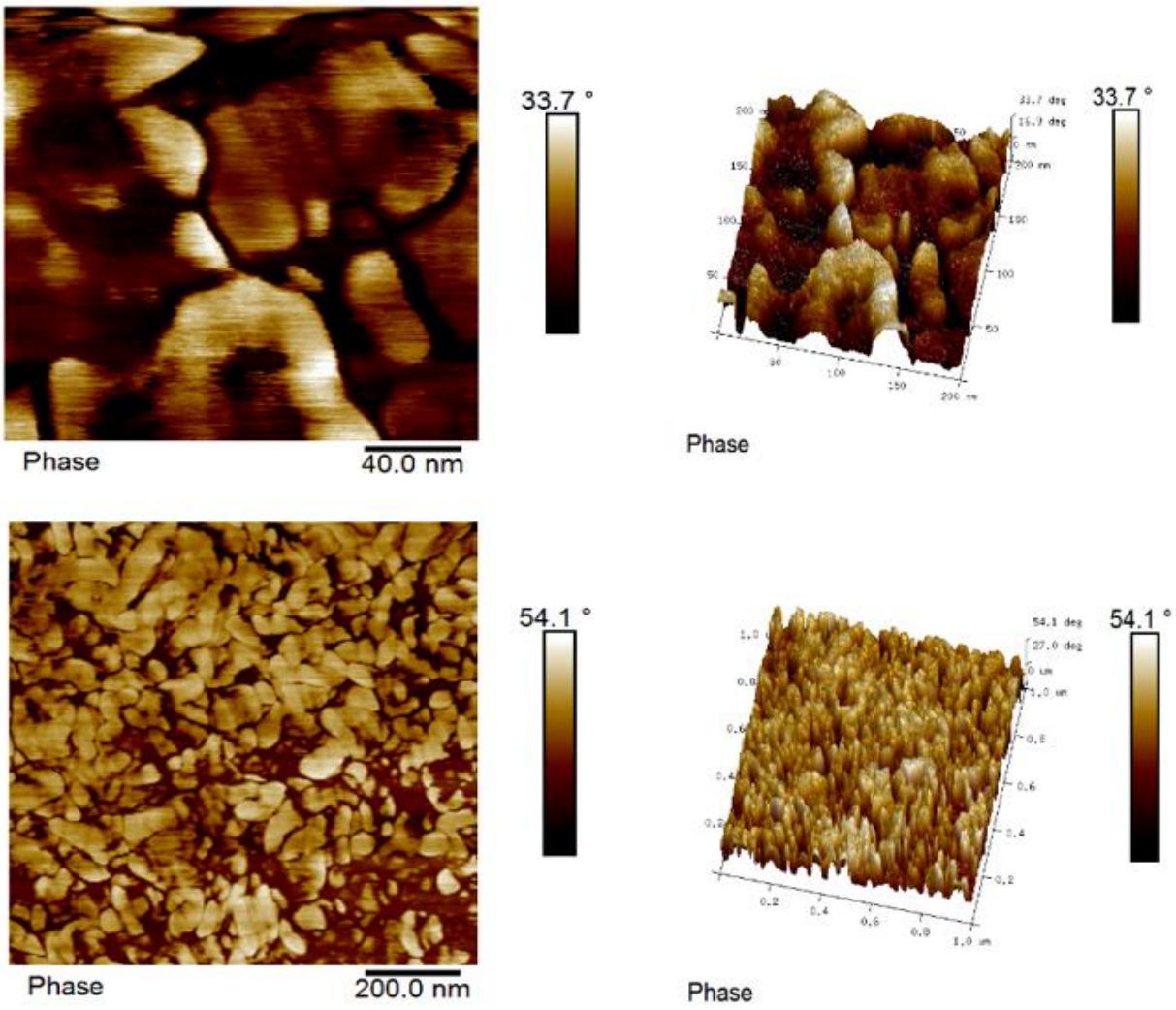

Figure 26. 1600 MPa nanostructured steel captured by AFM.

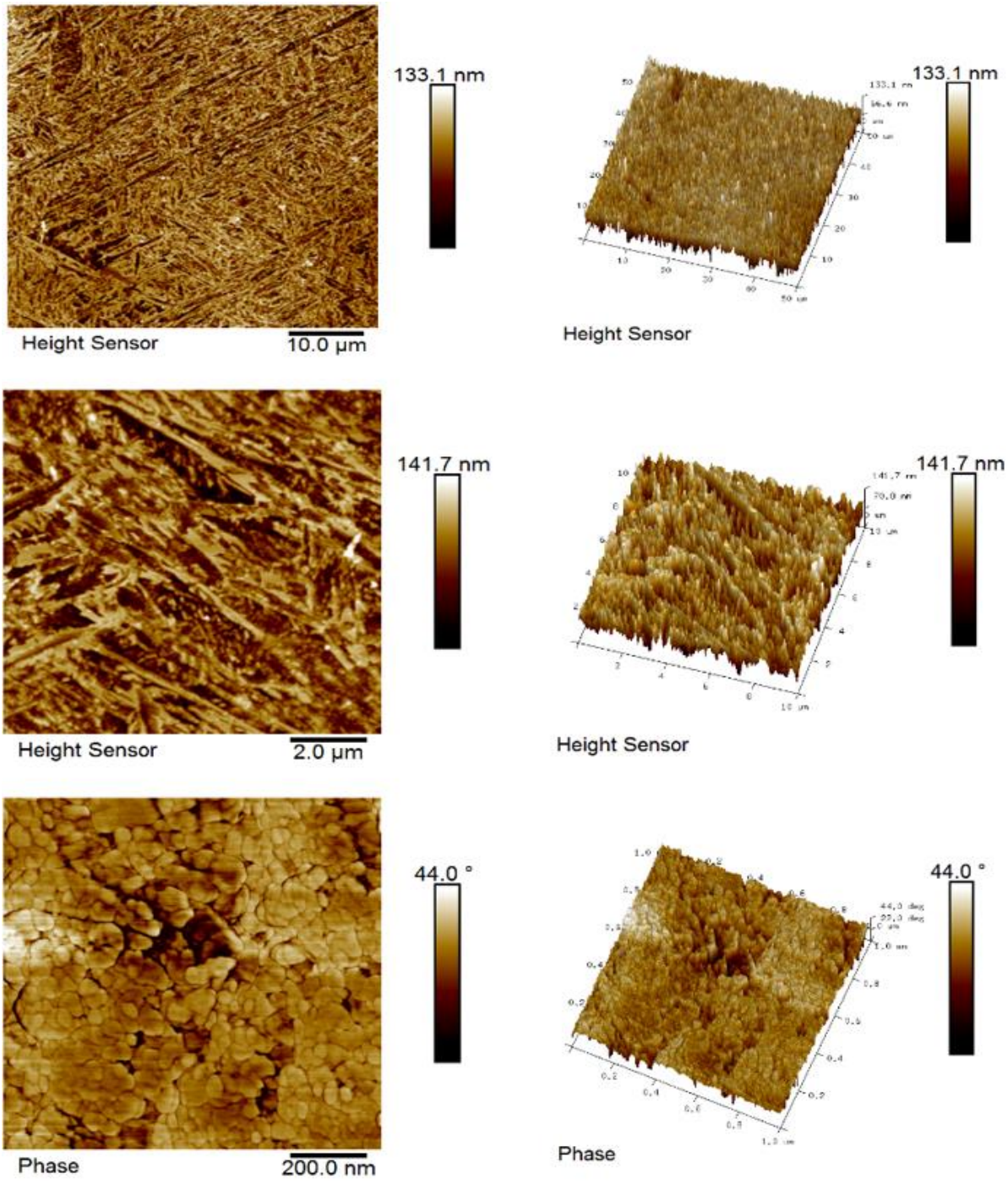

Figure 27. 2000 MPa nanostructured high strength steel captured by AFM.

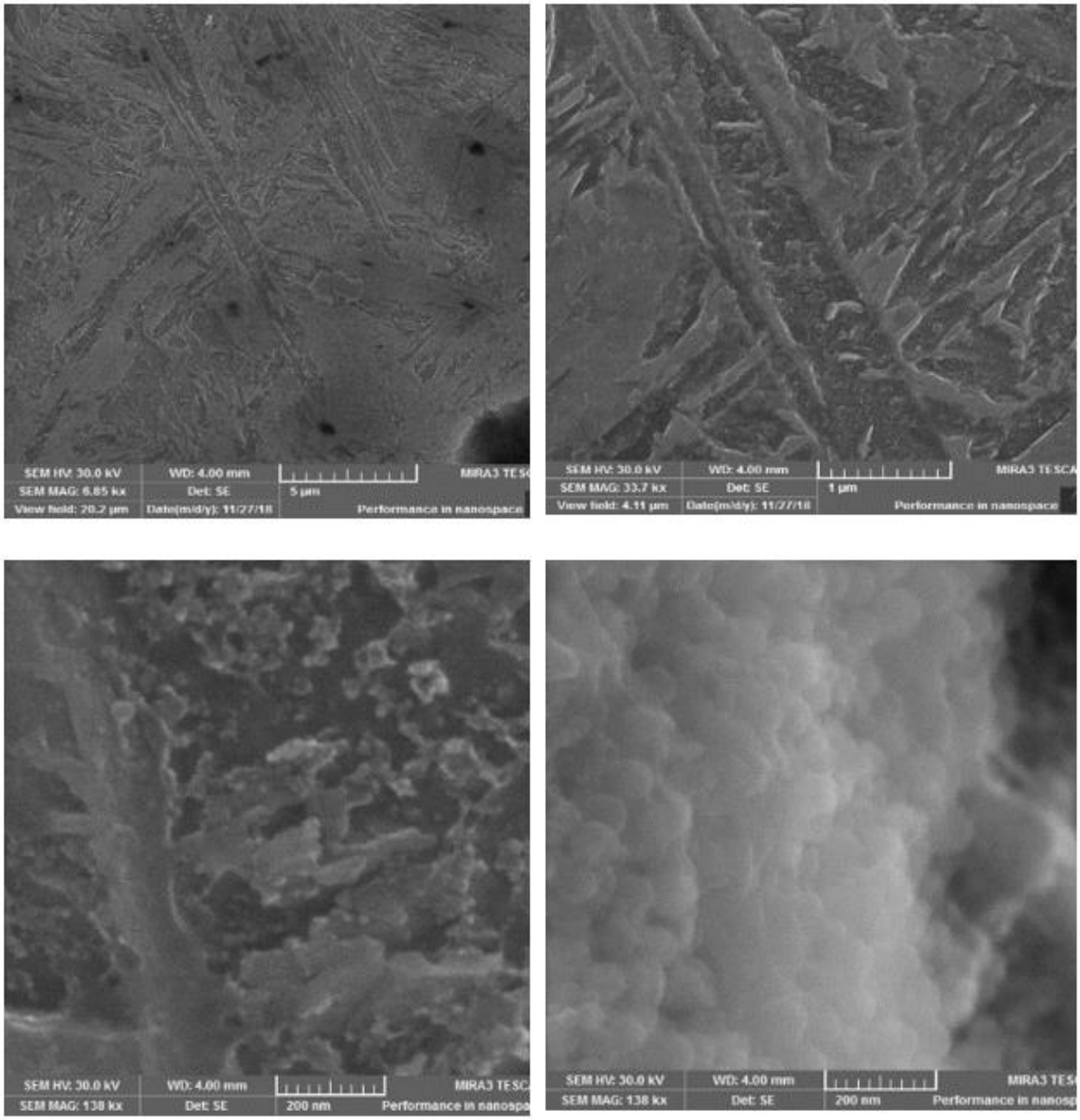

Figure 28. Microstructure of the 2000 MPa nanostructure high strength steel.

2.2 Mechanical properties and chemical composition

Table 6 and **Table 7** show the chemical and mechanical properties of the nanostructured steels by the manufacturer. Higher strength steels have higher carbon equivalent number and specifically are richer in C, Ni, Cr, Cu and Mo. Each alloy is named after its UTS in MPa.

Table 6. Nanostructured high strength steel chemical composition.

Alloy	C	Si	Mn	Ni	Cr	P	S	Cu	Mo	CE
1000 MPa	0.15	0.70	1.60	1.10	0.50	0.025	0.02	1.80	0.25	0.40
1300 MPa	0.2	0.70	1.60	1.30	0.60	0.025	0.02	2.10	0.30	0.48
1600 MPa	0.35	0.70	1.60	1.30	0.60	0.025	0.02	2.10	0.35	0.63
2000 MPa	0.47	0.70	1.60	1.30	0.80	0.025	0.02	2.10	0.45	0.77

Table 7. Mechanical properties of nanostructured high strength steels.

Alloy	YTS (Mpa)	UTS (Mpa)	Elongation (%)	Reduction in area (%)	Hardness (HRC)
1000 MPa	750	900 - 1000	13	40	32 - 37
1300 MPa	900	1100 - 1300	13	35	37 - 42
1600 MPa	1200	1500 - 1700	10	30	47 - 51
2000 MPa	1400	1900 - 2100	11	25	56 - 60

2.3 Hardness

Nanostructured bainitic steel samples are reported to have the hardness and ultimate tensile strength by the manufacturer. **Figure 29** demonstrates the hardness properties versus tensile collected macroscopically. Hardness measurement of the 2000 MPa, 1600 MPa, 1300 MPa and 1000MPa nanostructured bainitic steel was conducted by a nano-indenter.

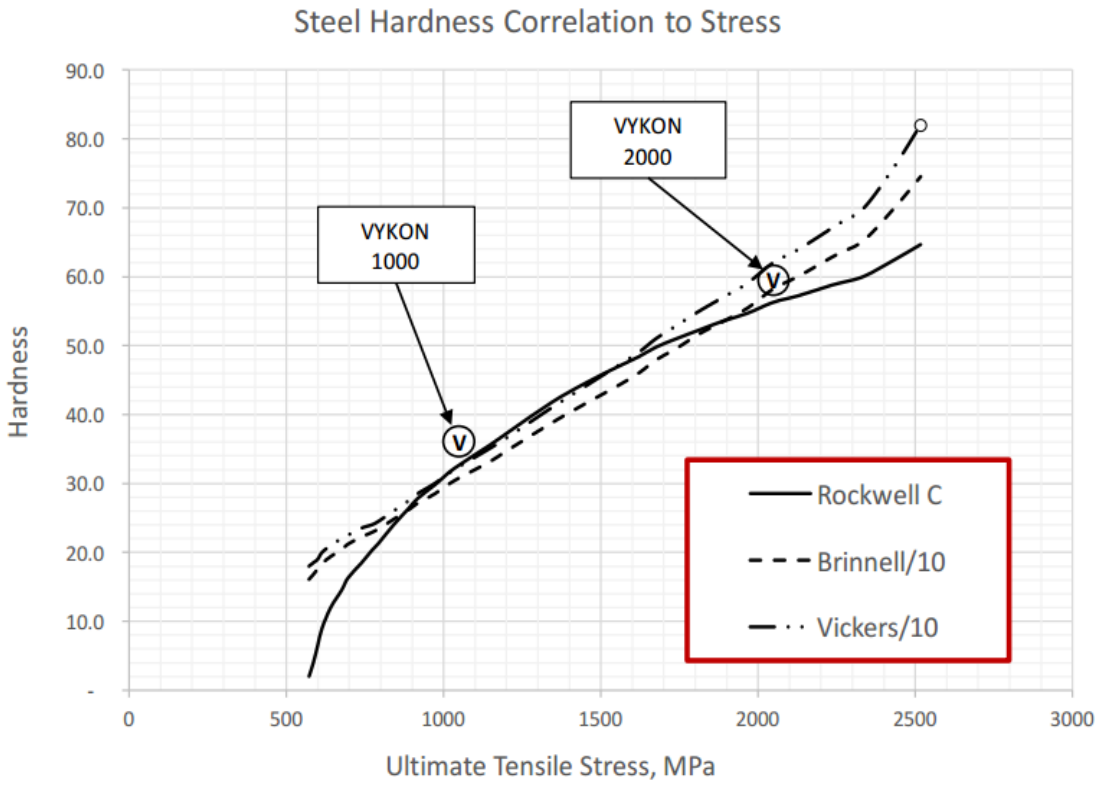

Figure 29. Hardness versus Ultimate Tensile Strength in MPa.

2.3.1 Nano-indentation

Researchers managed to collect reliable hardness data in nanostructured bainitic steels on the flat austenite phase. They found out the Young's modulus of austenite and bainitic ferrite both are close to 180 GPa [78]. The ductility of nanostructured bainite is enhanced due to increased bainitic treatment temperature while its elongation is improved due to higher damage resistance or moderate work hardening. In this study, we used indentation test where a probe is driven into a sample and consequently withdrawn by decreasing the applied force. The applied load (P) and depth of penetration (h**)** into the sample are uninterruptedly monitored and a displacement versus load plot is produced. The contact area is calculated from the probe area function A(hc) in which hc, the contact depth, is found with:

$$h_c = h_{max} - \varepsilon \frac{P_{max}}{S} \tag{15}$$

To consider for edge effects, the deflection of the surface at the contact perimeter is projected by assuming the geometric constant as 0.75. **Figure 30** shows the schematic of the cross section area and demonstrate the relationship of hc, P, A and h**.**

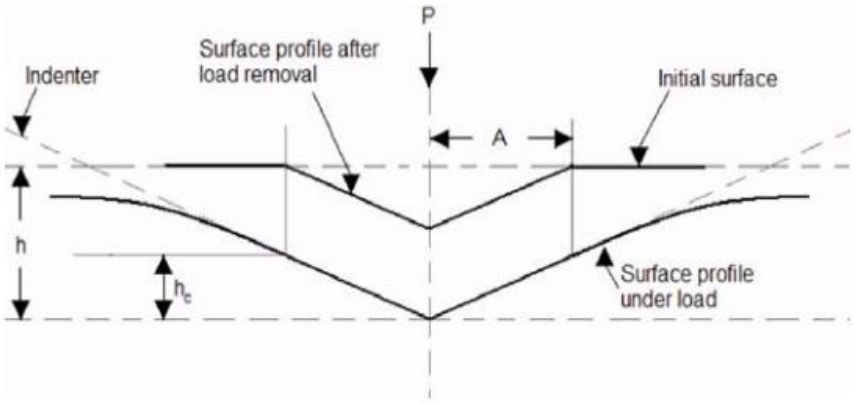

Figure 30. Schematic of nanoindentation (Trio Scan Manual).

In the nanoindentation test, the reduced modulus, related to the modulus of elasticity E**,** is reported. Reduced modulus defined as

$$\frac{1}{E_r} = \frac{1-v^2}{E}_{\text{sample}} + \frac{1-v^2}{E}_{\text{indenter}} \tag{16}$$

The properties of a standard diamond indenter probe are $E_{indenter}$ = 1140 GPa and $v_{indenter}$ =0.07. Poisson's ratio for most materials could vary between 0 and 0.5. Hardens is also defined as the max indentation load divided by the projected contact area at that load.

$$H = \frac{P_{max}}{A} \tag{17}$$

The reduced modulus could be written as:

$$E_r = \frac{S\sqrt{\pi}}{2\sqrt{A}} \tag{18}$$

In which S refers to the stiffness of the unloading curve and the projected contact area is A.

$$\mathrm{E_r} = \frac{\sqrt{\pi}}{2\sqrt{\mathrm{Ah_c}}} S \tag{19}$$

In which E_r is reduced modulus, A(hc) is contact area, and S represents stiffness. The hardness field is populated when the fit is executed and is calculated with the equation:

$$\mathrm{H} = \frac{\mathrm{P_{max}}}{\mathrm{Ah_c}} \tag{20}$$

The Contact depth is calculated with the equation:

$$\mathrm{h_c} = \mathrm{h_{max}} - 0.75 \frac{\mathrm{P_{max}}}{\mathrm{s}} \tag{21}$$

Figure 31 illustrates the heat map of hardness and reduced elastic modules and hardness, both in GPa, of 1600 MPa nanostructured steel after conducting 148 indents with the applied 10000 μN force. These heat maps are helpful to see the spatial spread of properties. **Figure 32** offers the bivariate fit of hardness by the reduced modulus in the 1600 MPa nanostructured steel. This statistical analysis proved the average hardness as 9.3 GPa and reduced modules as 184 GPa. A bivariate normal ellipse with probability of 0.9 is plotted to filter out the outliers. In addition, a linear fit for hardness is shown in terms of the reduced modulus. Similarly, **Figure 33** demonstrate the heat map of hardness and reduced

elastic modules and hardness, both in GPa, of 2000 MPa nanostructured steel after conducting 148 indents with the applied 10000 µN force. Unlike

Figure 31, and contrary to researchers reported [78], the 2000 MPa nanostructured steel have more variation of reduced modules. **Figure 34** also illustrate a statistical analysis in which the average hardness is 9.9 GPa and average reduced modulus is 213 GPa. The bivariate normal ellipse with probability of 0.9, plotted for the , contains higher data inside and therefore we have a higher correlation factor of 0.9. Additionally, we included a linear fit for hardness in terms of the reduced modulus as well. In a similar effort and after 94 indents, we plots the hardness distribution of all the nanostructured specimens in 10 quantiles, **Figure 35**. All hardness distributions, except the 1300 MPa steel, follow a normal distribution.

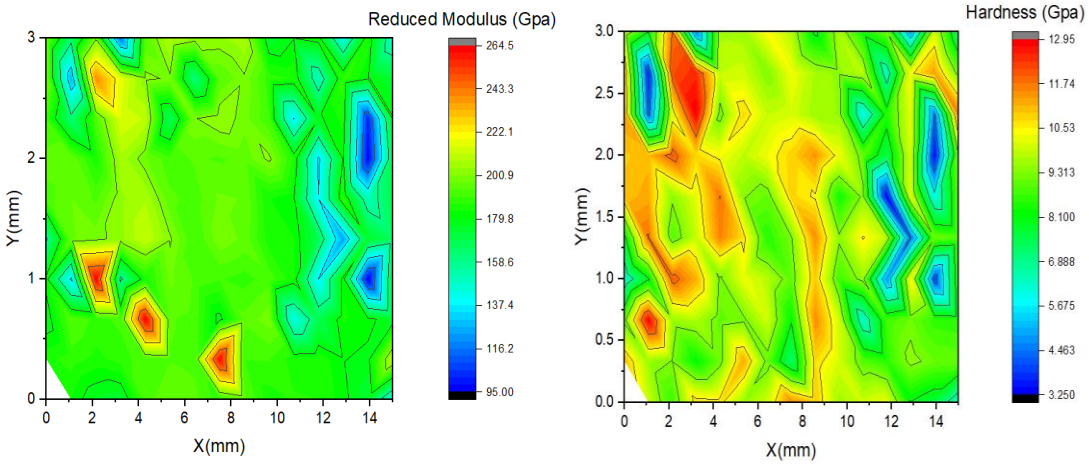

Figure 31. Hardness and Elastic reduced modules of 1600 MPa nanostructured, 148 indents - 10000 µN force.

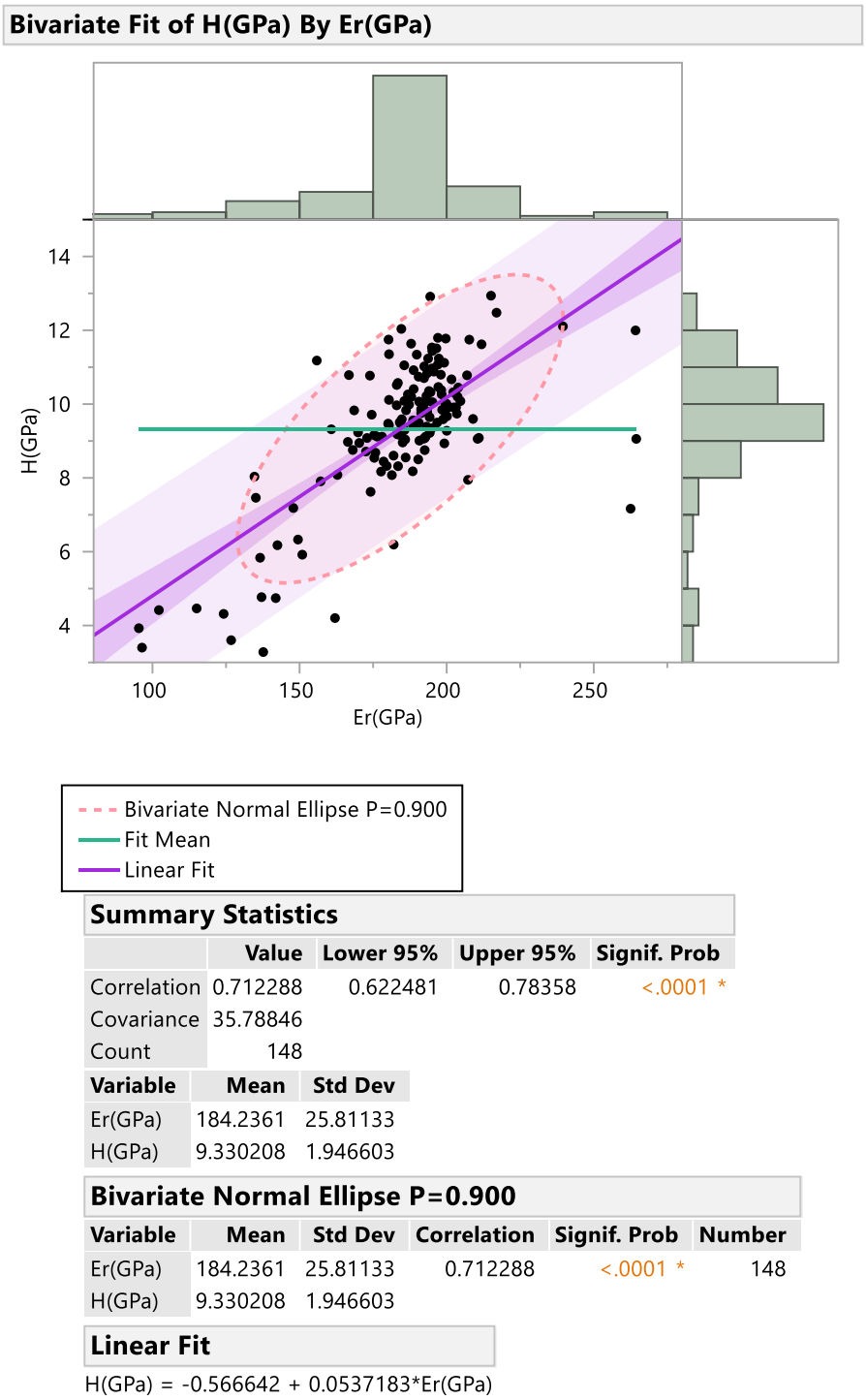

Figure 32. 1600 MPa nanostructured statistical analysis of elastic reduced modulus and hardness.

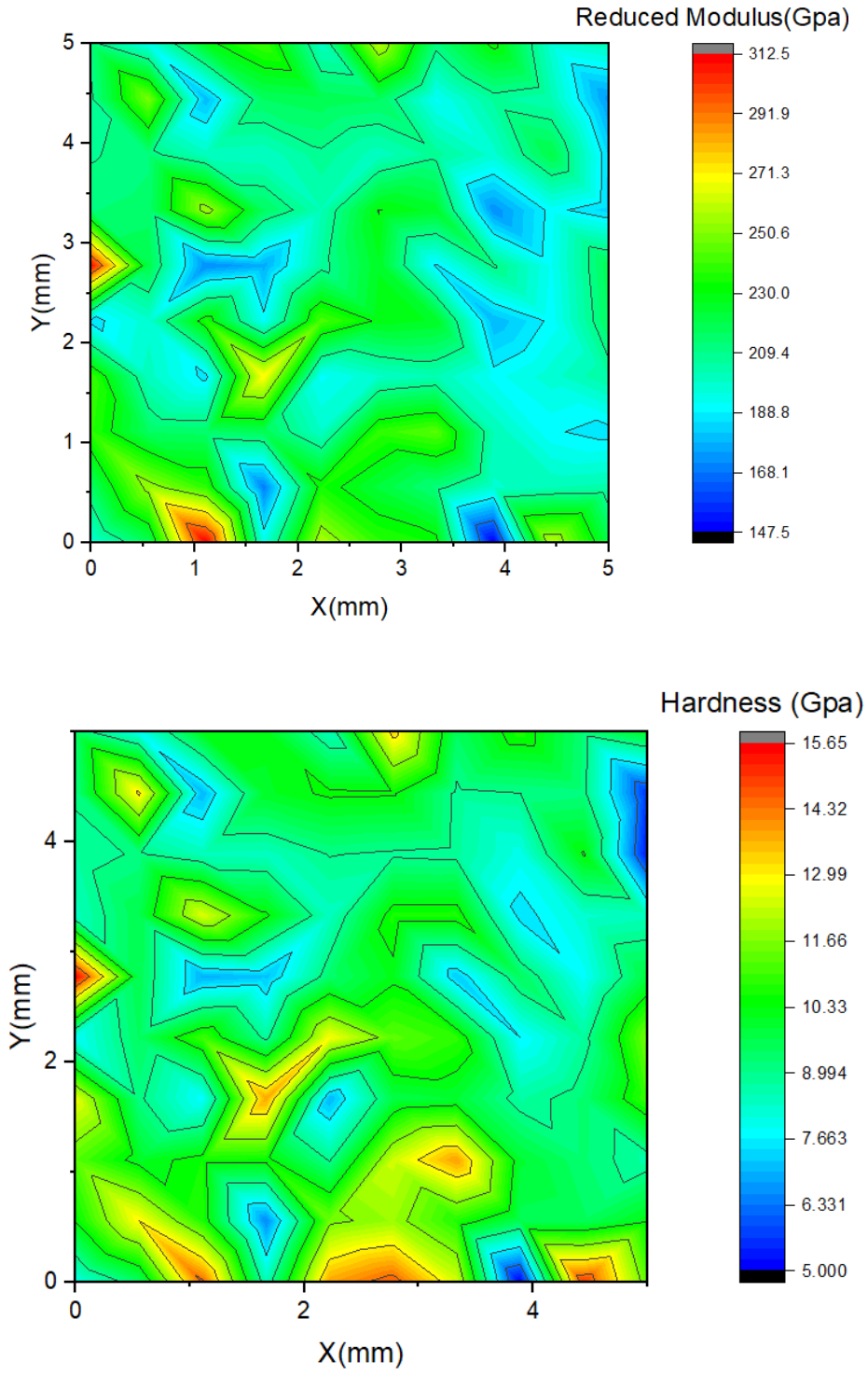

Figure 33. Hardness and elastic reduced modules of the 2000 MPa nanostructured, 148 indents-10000 µN force.

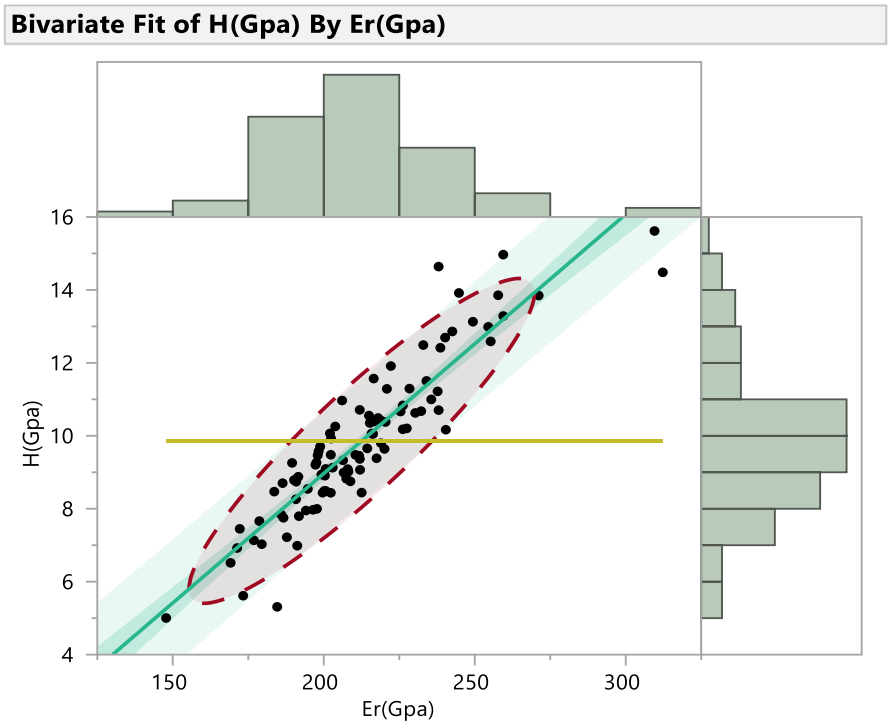

Summary Statistics

	Value	Lower 95%	Upper 95%	Signif. Prob
Correlation	0.912793	0.872872	0.940576	<.0001*
Covariance	50.54186			
Count	100			

Variable	Mean	Std Dev
Er(Gpa)	212.5625	26.67315
H(Gpa)	9.860981	2.075891

Bivariate Normal Ellipse P=0.900

Variable	Mean	Std Dev	Correlation	Signif. Prob	Number
Er(Gpa)	212.5625	26.67315	0.912793	<.0001*	100
H(Gpa)	9.860981	2.075891			

Linear Fit

H(Gpa) = -5.239443 + 0.0710399*Er(Gpa)

Figure 34. 2000 MPa nanostructured steel statistical analysis of elastic reduced modulus and hardness - 10000 μN force.

Hardness Distribution

1000 MPa Steel

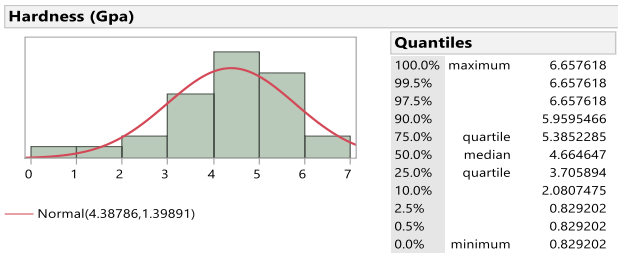

Quantiles		
100.0%	maximum	6.657618
99.5%		6.657618
97.5%		6.657618
90.0%		5.9595466
75.0%	quartile	5.3852285
50.0%	median	4.664647
25.0%	quartile	3.705894
10.0%		2.0807475
2.5%		0.829202
0.5%		0.829202
0.0%	minimum	0.829202

1300 MPa Steel

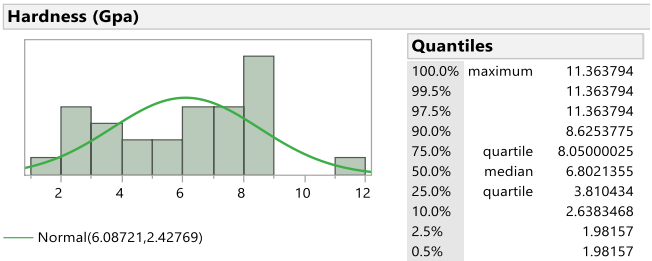

Quantiles		
100.0%	maximum	11.363794
99.5%		11.363794
97.5%		11.363794
90.0%		8.6253775
75.0%	quartile	8.05000025
50.0%	median	6.8021355
25.0%	quartile	3.810434
10.0%		2.6383468
2.5%		1.98157
0.5%		1.98157
0.0%	minimum	1.98157

1600 MPa Steel

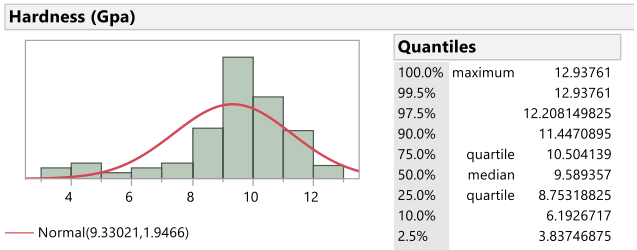

Quantiles		
100.0%	maximum	12.93761
99.5%		12.93761
97.5%		12.208149825
90.0%		11.4470895
75.0%	quartile	10.504139
50.0%	median	9.589357
25.0%	quartile	8.75318825
10.0%		6.1926717
2.5%		3.83746875
0.5%		3.280852
0.0%	minimum	3.280852

2000 MPa Steel

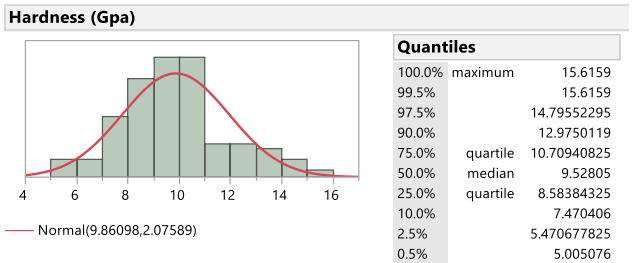

Quantiles		
100.0%	maximum	15.6159
99.5%		15.6159
97.5%		14.79552295
90.0%		12.9750119
75.0%	quartile	10.70940825
50.0%	median	9.52805
25.0%	quartile	8.58384325
10.0%		7.470406
2.5%		5.470677825
0.5%		5.005076
0.0%	minimum	5.005076

Figure 35. Hardness distribution nanostructured steels, 10000-µN force.

3. HYDROGEN PERMEATION OF NANOSTRUCTURED BAINITIC STEEL

Characterization of nanostructured bainitic high strength steel revealed austenitic and bainitic-ferritic constituents. Hydrogen diffuses through austenite slower than bainitic ferrite. Discovering the effective hydrogen diffusion coefficient, subsurface hydrogen concertation and number of traps of such a microstructure leads to a deeper understanding of the role of retained austenite, as the dominant trap in such microstructures. Devanathan–Stachurski hydrogen permeation experiments determined the permeation parameters and subsequently numbers of reversible and irreversible traps. Volume of the retained austenite correlated well with the total number of traps and the mean free path.

Lower mean free path, higher austenite content and trap density and more importantly finer dispersed distribution of films of retained austenite alongside with thin plates of bainitic ferrite satisfied percolation through the austenite. Therefore, permeation experiments demonstrated the lowest diffusivity in 2000 Mpa microstructure between all the bainitic high strength membranes. On the contrary, combination of granular morphology and smaller volume of retained austenite triggered the loss of percolation and yielded to the lowest diffusivity for 1000 Mpa microstructure. Higher volume of the retained austenite in isolation in the nanostructured bainitic steel does not produce lower diffusivity. Connectivity of the trap constituent morphology substantially affects the percolation of hydrogen and diffusion phenomena in this class of high strength steel.

Third generation nanostructured bainitic advanced high strength steel provides a combination of very high strength and 11-14% elongation. Bainite could have bainitic ferrite sheaves separated by untransformed austenite or cementite. Each bainitic sheaf has sub-units which are connected in three dimensions [79]. Such materials could extend the service life and overcome the current application challenges of high strength steels in many industries such as aerospace, oil and gas, nuclear, auto and defense. Ubiquitous atomic hydrogen is either available in the operational environment or is produced due to maintenance protective measures such cathodic protection. The hydrogen atom's diffusion into the steel has an utmost significance since it could entail adverse impacts on the materials operability envelop.

The initial step for revealing the extent of impact of atomic hydrogen penetration to nanostructured bainitic steel is to understand the microstructural constituents, phases, grain boundaries and size and permeation parameters; which directly would influence the diffusion of hydrogen phenomenon. Hydrogen atom could interact and be trapped in various steel microstructural features such as inclusions, dislocation, grain boundaries and micro-voids. After entrapment, the degree of energy required for hydrogen to regain its diffusion would vary based on the microstructural constituent binding energy (E_b) and the density of trap sites (N_T) per unit volume [80, 81]. In fact, trap strength will dictate the extent of diffusion delay. E_b and N_T could be obtained from Devanathan–Stachurski cell experiment and subsequently from the first and second transition curves; number of reversible and irreversible traps could be quantified.

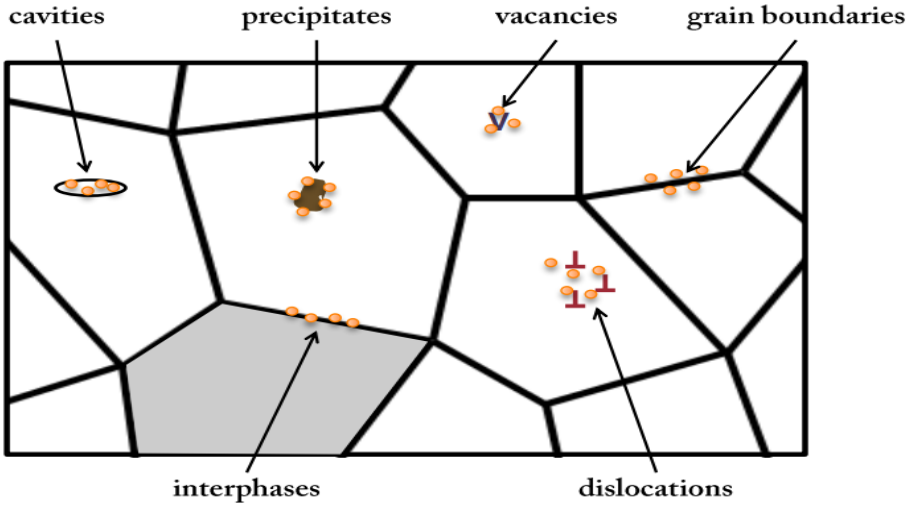

Figure 36. Stages of hydrogen interactions with steel [82].

The delivery of hydrogen to critical regions of microstructure, such as a crack tip, is dependent on how diffusion takes place. Studying hydrogen diffusion of nanostructured bainitic steels adjusts the engineering expectation to its true extended mechanical properties. Hydrogen atom could interact and be trapped in various steel microstructural features such as inclusions, dislocation, grain boundaries and micro-voids. These features will reduce the mobility of hydrogen by acting as traps.

Dislocations, grain boundaries, and micro voids that have low trap binding energies are considered reversible traps. Grain boundaries can either decrease the hydrogen mobility by acting as reversible hydrogen trapping sites at nodes and junction locations or raise hydrogen diffusion by facilitating quicker paths for diffusion [83-86]. Some researchers concluded that there is an optimal value of grain size for max hydrogen diffusion [87]. Irreversible traps range from non-metallic precipitates and inclusions such as Al_2O_3, complex (Fe, MnS) or double oxide $FeO.Al_2O_3$ inclusions, mixed compounds containing

Al-Mg-Ca-O, Si-ferric carbide. However, there was not a consensus on recognizing MnS as irreversible trap [88-90]. Vanadium, Titanium and Niobium precipitates are irreversible traps [91-93]. Retained austenite reduces the overall diffusivity and permeability of hydrogen through the steel since hydrogen has a higher solubility in retained austenite.

Ferrite austenite interfaces, in essence, could also be strong trap; especially if ferrite fully surrounds austenite, hydrogen mobility is greatly reduced. Cementite-ferrite interfaces, however, represent ineffective traps for hydrogen. In fact, a reversible trap is defined when hydrogen capture and release is sufficiently high to allow match the hydrogen atom relaxation time for a hydrogen atom to diffuse in the metal. Reversible traps poses a small interaction energy and short residence time, whereas irreversible traps do not release hydrogen without receiving thermal energy [44]. The irreversible trapping is responsible for a greater decrease in the effective diffusivity than the reversible trapping. A trap with a binding energy of 100 kJ/mol is considered irreversible at ambient temperature but becomes reversible at a sufficiently high temperature [68]. The purpose of this study is to investigate the diffusion of hydrogen in nanostructured bainitic steels with various austenite and bainitic ferrite content.

3.1 Percolation theory

Irregularities and heterogeneities of phase distribution in a lattice could lead to a disordered hydrogen diffusion. Provided a disordered medium of in a microstructure is a percolation lattice, and each phase is allocated a diffusivity coefficient, we will be able to study the hydrogen diffusion when merely a fraction of all sites influencing the diffusion process.

The hydrogen atom is only able to move from one occupied site of the lattice to a nearest neighbor that is occupied. Nanostructured bainitic advanced high strength steel consists of retained austenite and bainitic ferrite knowing that the diffusion in ferrite is faster than austenite. Heat treatment would determine the austenite content which its morphology along with its volume impact the hydrogen diffusion in nanostructured bainitic advanced high strength steel.

Percolation through austenite, as a barrier, is more difficult for hydrogen in a two-phase structure, especially when austenite fraction is above the percolation threshold. Hydrogen percolation could simplistically be explained to occur under three scenarios [94].

First is the case where austenitic films influence the diffusion of hydrogen the most in which the J_p denotes the flux in the microstructure and J_γ is inversely proportional to austenite films thickness. The thickness of austenite, which is proportional to austenite volume, illustrates the austenite concertation gradient in a defined boundary.

Second scenario could take place where austenite and ferrite are exposed to the hydrogen directly in which, in a unit area, the net flux is J_{op}, A is ferrite occupied surface area and $\phi = J_\alpha/J_\gamma$. Third case is where austenite content drops below the percolation threshold. The fluxes typically depend on diffusion coefficients. In bainitic high strength steels, ferrite and austenite have the diffusivity of 1.26×10^{-7} cm^2/s [95] and 2.65×10^{-12} cm^2/s [96] respectively. We used three as received samples and characterized the microstructural phases by scanning electron microscope, atomic force microscopy and wavelength-dispersive X-ray spectroscopy. Consequently, we used Devanathan cell to calculate the permeation parameters such as diffusivity, subsurface hydrogen

concentration. Finally, we quantified the binding energy, activation energy along with total, reversible and irreversible traps.

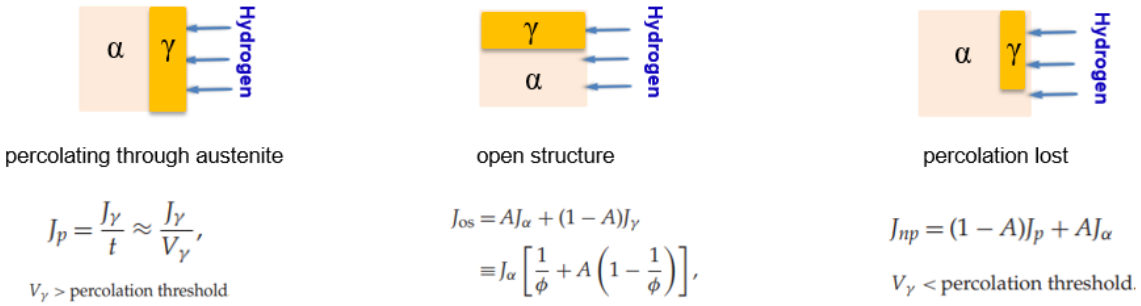

Figure 37. Three scenarios of hydrogen diffusion in a two-phase mixture of ferrite and austenite [94].

3.2 Permeation method

The ASTM G148 − 97 standard approach was used as a guideline to quantify the hydrogen permeation flux through thin nanostructured bainitic steel membranes [97]. The steel membranes' thickness varied between 0.15 mm to 0.2 mm. These membranes were prepared from the steel sheets provided by the manufacturer and cut by EDM. Since EDM cut could introduce hydrogen to the membranes, we baked them based on ASTM B 850-98 for 8 to 22 hours at 200˚C. Subsequently, we polished both sides of the steel membranes by SiC paper up to 600 grits; we washed them with distilled water, and ultrasonically cleaned them in acetone and ethanol.

The detection face of the membrane was plated with nickel (Ni) in a Watt's bath containing $NiSO_4$. $6H_2O$ 250 g/l, $NiCl_2.6H_2O$ 45 g/l, and H_3BO_3 40 g/l at 333.15 K (60 ˚C). This step is to eliminate flux-limiting surface impedances and to guarantee the consistency of the hydrogen oxidation current. Once proper nickel plating was achieved,

we rinsed the membranes with DI water. The plating process by a current density of 3mA/cm^3 for 10 minutes was done as a crucial step to prevent any interference with hydrogen diffusion. Eventually the steel membrane was located and sealed between both electrochemical cells, **Figure 38**.

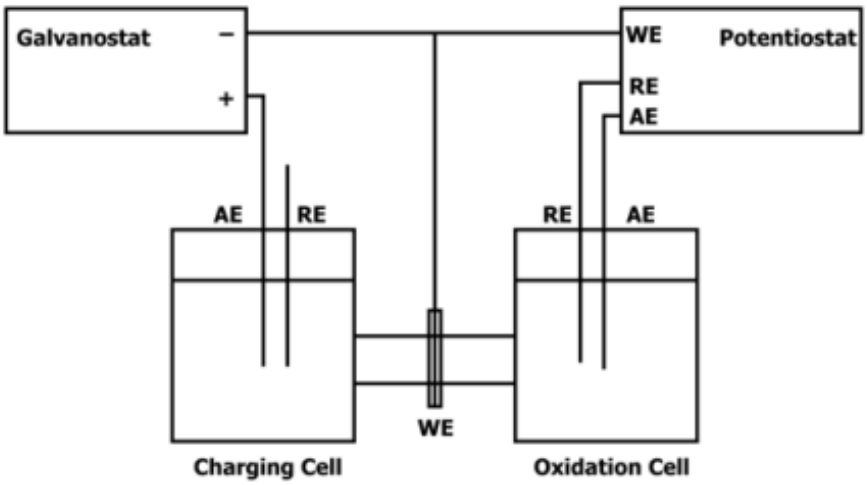

Figure 38. Devanathan–Stachurski hydrogen permeation experimental set up [97].

An area of 28 cm^2 was exposed to each electrolyte inside the cells. In order to initiate the permeation experiment, we ought to establish a reference current in the oxidation cell. We poured the prepared 0.1 M NaOH solution into the hydrogen oxidation cell. The deaeration of 0.1 M NaOH solution started by research grade N_2 gas and continues through the duration of the test. We waited until the current decayed to a stable value in range of 25 - 50 μA while maintaining potential of the steel membranes at 0.3 V SCE.

This potential has been ensured to be proper through a potentiodynamic test for nanostructured bainitic steels. After we observed the stability of the background current, a solution for composed on 0.1 M NaOH and 10 g/L of $Na_2S{\cdot}9H_2O$ prepared and poured

into cathodic cell. We maintained the nitrogen flow in hydrogen charging cell during the hydrogen permeation test. We catholically polarized the NB AHSS steel membrane in the hydrogen-charging cell with the current density of 3mA cm^{-2} at room temperature.

3.3 Diffusion parameters

The key parameters after performing conducting the hydrogen permeation experiment across different steel membranes are shown in **Figure 1** and **Table 1**. The steady-state molar flux of hydrogen, J_{ss} ($mol.cm^{-2}\ s^{-1}$) could be obtained from equation 1:

$$J = \frac{I_{ss}}{nF} \tag{22}$$

where the steady-state current density ($A.cm^{-2}$) is shown by I_{ss}, n is the number of electrons transferred in the electrochemical reaction, and F is Faraday's constant. The hydrogen permeation rate Q ($mol.cm^{-1}.s^{-1}$) on the other hand could be achieved by equation 2:

$$Q = J_{ss}L \tag{23}$$

with L denoting the thickness of the specimen (cm). Another important parameters of interest is the effective diffusivity. This parameter imply irreversible and irreversible traps. This parameter was calculated using equation 3 shown below:

$$D_{eff} = \frac{L^2}{6t_{lag}} \tag{24}$$

The experimental data may also be compared with theoretical models such as Fick's second law represented by the following relationship:

$$\frac{J(t)}{J_{ss}} = 1 + 2\sum_{n=1}^{\infty}(-1)^n \exp(-n^2\pi^2 \times \frac{D_{eff}\, t}{L^2}) \quad (25)$$

where the t_{lag} is a parameter indicating the time (s) it takes current to reach 63% of the steady-state current. Assuming Fick's first law is applicable, C_0 the sub-surface concentration of hydrogen in the charging cathode (mol/cm^3) may be determined from the following calculation [98].

$$C_0 = \frac{Q}{D_{eff}} \quad (26)$$

3.4 Total, reversible and irreversible traps

D_0 is 7.23× 10^{-4} cm^2s^{-1} and E_L *is* 5690 J/mol (barrier of energy for hydrogen jumps) [99]. The trapping parameters N_T, the number of trapping sites per unit volume, and E_b, the binding energy per mol of traps, can be predictable by using equation 6. N_l is the number of lattice sites per unit volume in the metal and is quantified as 5.2× 10^{23} per cm^3 at room temperature. Provided D_{eff} is plotted on a logarithmic scale against the inverse of the temperature, the values would be on a straight line. We write the equation for this line as $D_{eff} = Ae^{(\frac{-B}{RT})}$. Comparing this expression with equation (6) yields the following relations:

$$D_L = D_0 \exp \frac{-E_L}{RT} \quad (27)$$

$$D_{eff} = D_0 \frac{N_l}{N_T} \exp \frac{-(E_b + E_L)}{RT} \quad (28)$$

$$E_b = \Delta E_a - E_L \quad (29)$$

Where E_b shows the binding energy and ΔE_a is the activation energy (E_b+E_L). The microstructural number of traps (N) is obtained by hydrogen binding energy (E_b) and the trap density. Some recent mathematical equations facilitate the number of traps to be calculated through the direct use of the values of the diffusivity and the hydrogen subsurface concentration [98, 100] . C_0 represents the subsurface concentration, D_L is the lattice diffusivity of hydrogen in αFe = 1.28×10^{-4} cm^2/s and D_{eff} is the effective diffusivity and N_A is Avogadro's number (6.022×10^{23}).

$$N_T = \frac{C_0}{3}\left(\frac{D_L}{D_{eff}} - 1\right) N_A \quad (30)$$

Furthermore, by using equations 10 and 11, the trap densities of the reversible and irreversible traps may be determined. Where $N_{t,ir}$ and $N_{t,re}$ are the irreversible and reversible hydrogen trap densities respectively and $N_{t,1}$ and $N_{t.2}$ are the hydrogen trap densities of the first and second transient respectively.

$$N_{t,re} = N_{t,2} \quad (31)$$

$$N_{t,ir} = N_{t,1} - N_{t,2} \quad (32)$$

3.5 Results and discussion

Figure 39 shows the plots of current density in ($\mu A/cm^2$) versus time in seconds normalized at different temperatures. These plots are offering valuable information about the permeation parameters such as diffusivity, subsurface hydrogen concertation, flux, permeability, trap density and distribution in the 1000 Mpa, 1300 Mpa and 2000 Mpa nanostructured bainitic steels. Using equation 1, 2, 3 and 5 allow finding the diffusivity, subsurface hydrogen concertation, flux and permeability from the 20 ℃ curve for each microstructure. The 2000 MPa steel showed an order of magnitude lower effective diffusivity than the 1300 MPa and 1000 MPa steels. This could be due to the higher concertation of austenite in 2000 Mpa steel relative to 1300 Mpa and 1000 Mpa steels. Furthermore, the 2000 Mpa microstructure has a dispersed and very dense distribution of smaller austenitic grains shown in forms of sheathes and very small blocks. This results in a lower mean free path and therefore lower effective diffusivity in the 2000 Mpa steel. Effective diffusion coefficient is inversely related to the apparent hydrogen solubility. The data confirms that the Mpa 1000 has the lowest apparent hydrogen solubility since it has the highest diffusivity between three samples. **Table 8** detailed the effective diffusion coefficient (cm^2/s), subsurface hydrogen concertation (mol/cm^3), flux ($mol/cm^2.s$) and permeability (mol/cm.s) of three classes of nanostructured bainitic advanced high strength steels.

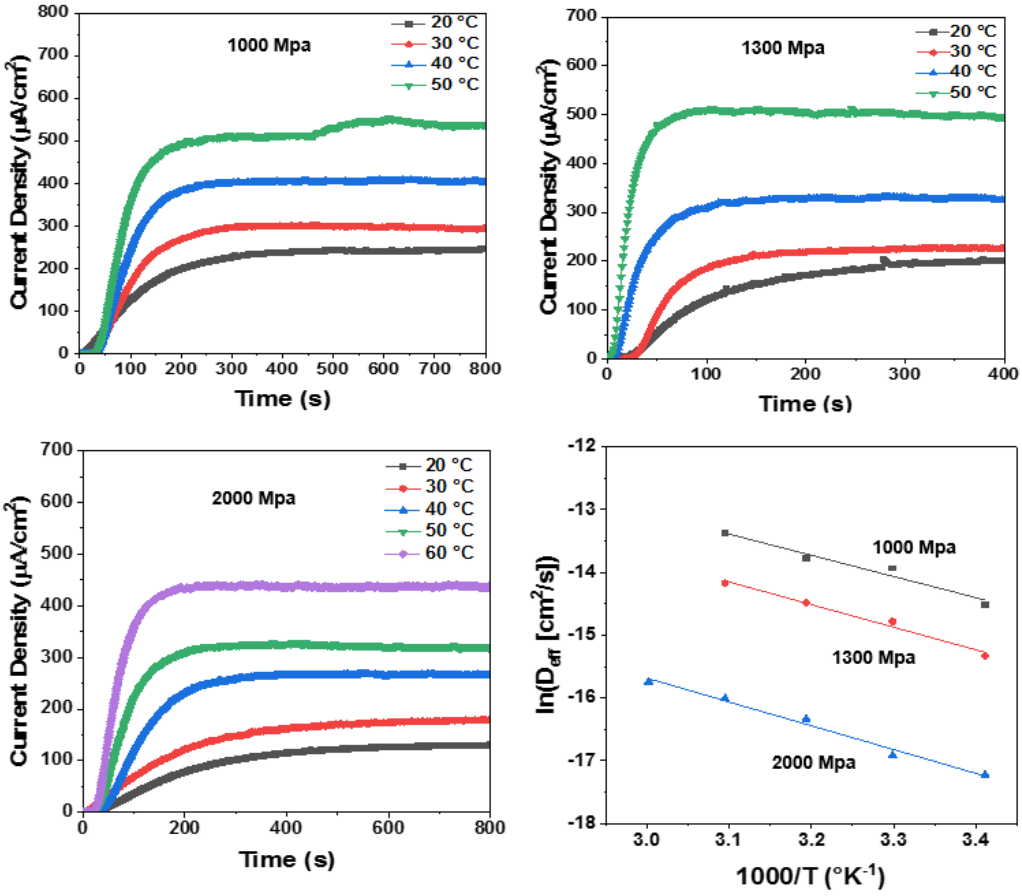

Figure 39. Effective diffusivities to calculate the activation for bonding energy of 1000 MPa, 1300 MPa and 2000 MPa.

Table 8. Effective diffusivity, subsurface hydrogen concentration, flux and permeability.

Samples at 20 °C	D_{eff} (cm^2/s)	C_0 (mol/cm^3)	J (mol/cm^2 s)	Q (mol/cm s)
1000 MPa	$6.45 \times 10^{-7} \pm (0.12)$	$4.24 \times 10^{-5} \pm (0.15)$	$1.24 \times 10^{-9} \pm (0.05)$	$2.74 \times 10^{-11} \pm (0.07)$
1300 MPa	$3.13 \times 10^{-7} \pm (0.04)$	$4.27 \times 10^{-5} \pm (0.04)$	$1.03 \times 10^{-9} \pm (0.01)$	$1.34 \times 10^{-11} \pm (0.03)$
2000 MPa	$4.23 \times 10^{-8} \pm (0.87)$	$1.08 \times 10^{-4} \pm (0.05)$	$6.54 \times 10^{-10} \pm (0.27)$	$4.58 \times 10^{-12} \pm (0.27)$

The 2000 Mpa steel showed an order of magnitude lower effective diffusivity than the 1300 Mpa and 1000 Mpa steels. This could be due to the higher concertation of austenite in 2000 Mpa steel relative to 1300 Mpa and 1000 Mpa steels. Furthermore, the 2000 Mpa microstructure has a dispersed and very dense distribution of smaller austenitic grains shown in forms of sheathes and very small blocks. This results in a lower mean free path and therefore lower effective diffusivity in the 2000 Mpa steel. Effective diffusion coefficient is inversely related to the apparent hydrogen solubility.

The data confirms that the MPa 1000 has the lowest apparent hydrogen solubility since it has the highest diffusivity between three samples. Before the current density reaches a steady state at room temperature (grey lines in **Figure 39**, we can observe that 1000 MPa steel has a steeper slope than the 2000 and 1300 MPa steels. We applied a same current density to all samples and we are observing that we are receiving hydrogen on the oxidation side at different rate hence the slopes vary. Steeper slope implies we received hydrogen in a less fraction of time.

This could happen due to less number traps in the microstructure and higher effective diffusivity coefficient. Therefore, we proceeded to calculate the total traps. By conducting the permeation test at various temperatures and plotting the effective diffusivities against the inverse of temperature, we obtained the binding and activation energy for the 2000 MPa, 1300 MPa and 1000 MPa steels. Data show that the 2000 MPa has the highest binding energy and activation energy in J/mol, **Table 9**.

Table 9. Binding energy and activation energy.

Samples	E_b (J/mol)	ΔE_a (J/mol)
1000 MPa	28018	22328
1300 MPa	29923	24230
2000 MPa	31468	25779

The main reason is due to the higher austenite content and its dense microstructure as well as the smallest mean free path relative to other microstructures. By rearranging equation 7, we obtained the total number of traps, **Table 10**. It is important to mention we used equation 9 as well to calculate the total number of traps through the subsurface hydrogen concertation and found out that we could have a same order of magnitude number of traps and trend, however, we think finding traps through the microstructure specific binding and activation energy delivers a more representative trap density.

Table 10. Trap densities calculated from activation energies.

Samples at 20 °C	N_T (cm^{-3})	$N_{T,\,Rev}$ (cm^{-3})	$N_{T,\,Irr}$ (cm^{-3})
1000 MPa	1.93×10^{21} (±0.12)	1.63×10^{21} (±0.19)	3.02×10^{20} (±0.13)
1300 MPa	6.37×10^{21} (±0.31)	4.82×10^{21} (±0.25)	1.54×10^{21} (±0.32)
2000 MPa	9.82×10^{22} (±0.16)	6.35×10^{22} (±0.21)	3.47×10^{22} (±0.09)

After capturing the permeation parameters in **Table 9**, we repeated another cycle of permeation experiment after the first one and calculated the reversible and irreversible

traps by equation 10 and 11, **Table 10**. The 2000 MPa consistently showed to have one order of magnitude higher number of traps. This could be due to the higher interface of bainitic ferrite and austenite as strong traps. The 1000 MPa and 1300 MPa steels showed to have an order of magnitude less traps density, relative to 2000 MPa steel. The reason directly is related to the higher percentage of bainitic ferrite and less austenite content. It is evident that the irreversible traps have less impact on hydrogen diffusion in nanostructured bainitic steels.

4. HYDROGEN EMBRITTLEMENT OF NANOSTRUCTURED STEEL, A NON-LINEAR FRACTURE MECHANICS APPROACH

Many fracture mechanics testing approaches to evaluate stress corrosion cracking (SCC) fracture toughness for high strength low alloy steels using through the elastic plastic approach (J integral method) [101, 102]. Nevertheless, the notched tensile SSRT determines the force required for crack extension by J integral until an unstable fracture initiates[103]. Using a notched round tensile specimen in a SSRT load frame could deliver the J_I required for crack propagation. J_I could be calculated with recording load and extension provided through notched tensile SSRT (see appendix 1 and 2). The individual J_I or K_I values could be obtained from the ratio of the maximum load of the notch specimen (σ_{NTS}) to yield strength $\sigma_{y:}$ $R = \frac{\sigma_{NTS}}{\sigma_y}$

$$0 < R \leq 2 \quad K_I = \sigma_{NTS} D^{0.5} \left[2\left(\frac{d}{D}\right)^4 \left(1 - \frac{d}{D}\right) + 0.364 \left(\frac{D}{d}\right)\left(1 - \frac{d}{D}\right)^2 \right]^{0.5} \tag{33}$$

$$R > 2 \quad J_{I,i} = \frac{(L_0 + \delta_i)\left(\frac{3\pi R_0^2 \delta_i^2 E_y}{2L_0} + P_i \delta_i\right)}{2L_0 r_0^2} \tag{34}$$

$$K_{IC} = \sqrt{\frac{J_{IC} E_y}{1 - \upsilon^2}} \tag{35}$$

L_0 is initial gage length, R_0 shows initial radius, r_0 demonstrates radius at the notch, D is the gage diameter and d denotes notch diameter. This equation stems from many studies on the J_I integral values for notch tensile specimens [104-106].

4.1. 1600 MPa nanostructured steel susceptibility to sulfide corrosion cracking

The susceptibility of a high strength low alloy nanostructured steel to sulfide stress corrosion cracking (SSCC) resistance is assessed. Notch Tensile Slow Strain Rate Testing (NTSSRT) method is used to evaluate the threshold stress intensity values (K_{ISSCC}). The objective of this study is to understand the effect of the microstructure and chemical composition on the susceptibility to SSCC; the control condition is a conventional low alloy carbon steel with a tempered martensitic microstructure.

The tests were performed in a brine with 1% NaCl buffered at pH 4.5 with H_2S gas with 1% to 100% (mol %) balance N_2 at room conditions. The nanostructured steel results in the K_{ISSCC} parameter are: 107 Ksi $in^{0.5}$ at 1% H_2S to 42 Ksi $in^{0.5}$ at 100% H_2S. The control condition exhibited 22 Ksi $in^{0.5}$ at 100% H_2S. The evaluation of the relative crack propagation energy suggest that the nanostructured ferrite grains exhibit a much lower susceptibility to SSCC than the tempered martensitic microstructure.

The susceptibility of a high strength low alloy nanostructured steel to sulfide stress corrosion cracking (SSCC) resistance is assessed. Notch Tensile Slow Strain Rate Testing (NTSSRT) method is used to evaluate the threshold stress intensity values (K_{ISSCC}). The objective of this study is to understand the effect of the microstructure and chemical composition on the susceptibility to SSCC; the control condition is a conventional low alloy carbon steel with a tempered martensitic microstructure.

The tests were performed in a brine with 1% NaCl buffered at pH 4.5 with H_2S gas with 1% to 100% (mol %) balance N_2 at room conditions. The nanostructured steel results in the K_{ISSCC} parameter are: 107 Ksi $in^{0.5}$ at 1% H_2S to 42 Ksi $in^{0.5}$ at 100% H_2S. The control condition exhibited 22 Ksi $in^{0.5}$ at 100% H_2S. The evaluation of the relative crack propagation energy suggest that the nanostructured ferrite grains exhibit a much lower susceptibility to SSCC than the tempered martensitic microstructures[107-110]. In the oil & gas industry, one of the more severe form of environmentally assisted cracking found is the sulfide stress corrosion cracking (SSCC), in which H_2S contained in sour environments, mediates to enhance the permeated hydrogen which plays an important role in the crack initiation and propagation [111-114].

The susceptibility to SSCC depends on the microstructural characteristics of the material. In materials, such as carbon steels martensitic structures product of heat treatment such as quenching are typically found to be more susceptible to SSCC [115-117]. Hence, the focus of the development of SSCC resistant high strength steels has been the control of the microstructural features [117-120]. The objective of the present study is to evaluate the susceptibility of a novel high strength low alloy nanostructured steel to sulfide cracking resistance (SSCC). The relative effect of the steel structure on the susceptibility to SSCC is studied by comparing with a control condition, which is a conventional low alloy carbon steel with a tempered martensitic microstructure.

4.1.1 Experimental methodology

The use of the fracture mechanics description of the conditions for the onset of crack propagation has been widely used to describe HEC susceptibility in a number of alloy-

environment systems [111, 121, 122]. This approach provides a quantitative assessment of the SSCC susceptibility by the experimental evaluation of either the threshold stress intensity parameter, K_{ISSCC}, by means of suitable experimental method [104, 123, 124].
In the present study, the evaluation of the K_{ISSCC} values is through using notch tensile specimens in combination with the slow strain rate technique. The round notch tensile specimens (NTS) is described in the literature as a cost effective and rapid method that can provide a conservative (yet oftentimes realistic) estimate of the K_{th} value for metallic materials [125].

In general, the proposed NTS methodology measures the crack extension force defined by means of the J integral up to the point where unstable fracture occurs [103, 126]. The measurement of the J value required to propagate such cracks is accomplished by testing a round tensile specimen, in which a notch of a given radius and depth is machine in the gage section, under constant extension rate up to the point of failure due to plastic instability (necking). The use of the NTS method to assess the threshold fracture toughness for environmentally assisted cracking, as K_{ISSCC}, appears in the literature by either constant load or by applying a slow strain extension rate [104, 127, 128]. However, it has experienced the intrinsic limitation that the calculation methods for the estimation of the K_{ISSCC} are reliable only if the fracture and crack propagation during testing occurs in regime were elastic linear fracture mechanics apply [105, 106]. Using the ISO 15156 standard a series of possible sour environments of different severity depending on brine pH and H_2S [129] was used as the basis of the experimental test matrix developed to evaluate the susceptibility to SSCC, **Table 11**.

Table 11. Experimental test matrix for nanostructured steel susceptibility to SSCC.

Test condition	H_2S Partial pressure	SSCC regions covered according to ISO 15156
Air Test	None	Inert in relation to SSCC
Brine at pH 4.5	1-100 Kpa	1, 2 and 3

In our experiments, we used a brine at pH 4.5 to evaluate high strength steels simulating the characteristics of sour environment associated with oil wells producing conditions as described in the ISO 15156 document [129], which are between the most severe conditions behind SSCC. To have a more precise control over the H_2S activity at low molar gas content, the tests solution was modified by introducing sulfide-bearing species that will produce the same compound activity as in the corresponding sour environment. **Table 12** describes the composition of the brines used in the present work. The NTS specimens used were fabricated from the steel specimens, following the specifications shown in **Figure 40**. Both smooth and notched specimens were produced, the notch was done up to a depth of 10% of the gage diameter (0.112") with 60° the method described in the literature[130]. The NTSSRT experiments in this study were performed at a strain rate of 10^{-6} s^{-1} following the recommended values suggested in the literature for evaluating SSCC susceptibility in high strength steels. The experiments performed simulating the sour service conditions using the pre conditioning protocol indicated by the NACE TM0177-2016 standard using high purity N_2 gas to ensure brine deaeration [131].

Table 12. Composition of the test brine used in the evaluation of 1600Mpa nanostructured steel SSCC susceptibility.

Species concentration	1% mol H_2S gas phase (g/l)	10% mol H_2S gas phase (g/l)	100% mol H_2S gas phase (g/l)
NaCl	10.10	10.10	10.10
HCl	1.02	1.02	1.02
$Na[C_2H_3O_2]$	4.04	4.04	4.04
Na_2S	0.17	0.83	10.00
$C_2H_4O_2$	0.59	2.95	34.56

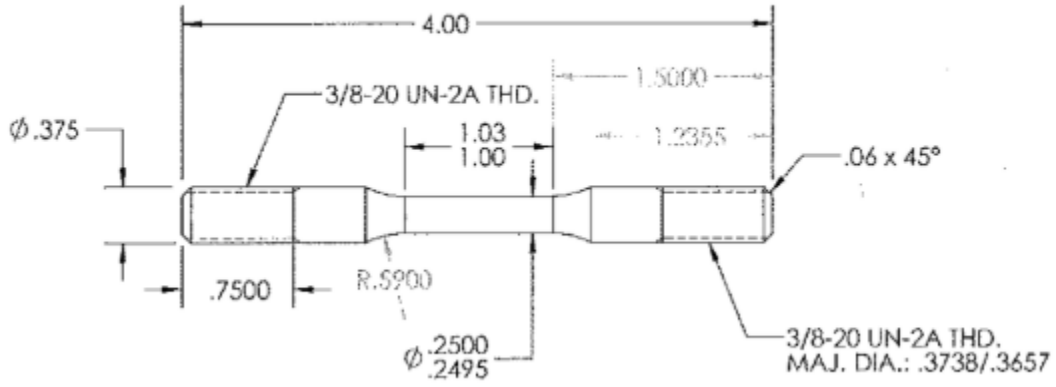

Figure 40. Dimension and tolerances of the notched tensile specimen configuration.

The NTSSRT experiments were carried out in the test frame with a capacity of 10000 lbs. This machine uses a digital stepper motor control to ensure steady extension rate through the experiment. The brine exposed to the test specimens is in a Plexiglas cell designed for H_2S testing. **Figure 41** demonstrates the test cell configuration.

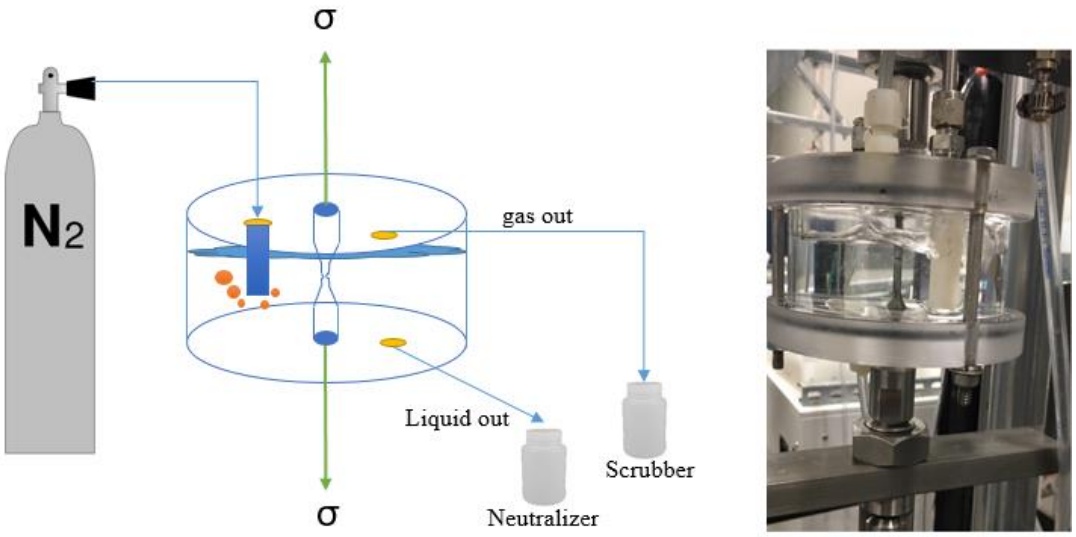

Figure 41. Test cell used in the experiments involving sour test brine.

4.1.2 Results and discussion

The nanostructured steel used in this study exhibit very high tensile strength around 1600 MPa (145 Ksi) of yield point strength together with excellent plasticity above 11% of deformation [132]. For control tests an API C110 high strength carbon steel was used, this steel exhibits a yield stress of 115 Ksi. SEM microscope was used to characterize the structure of the nano-structured steel after etching the sample. **Figure 42** shows the typical structure feature of this material. The microstructural analysis performed suggest that the nanostructured steel presents a fine bainitic structure with austenite finely dispersed within an acicular matrix structure. To establish a control condition, a number of tests were performed in the air at room condition without the presence of H_2S saturated brines. The experiments conducted in this relative inert environment are both notched and smooth; the stress strain resulting response.

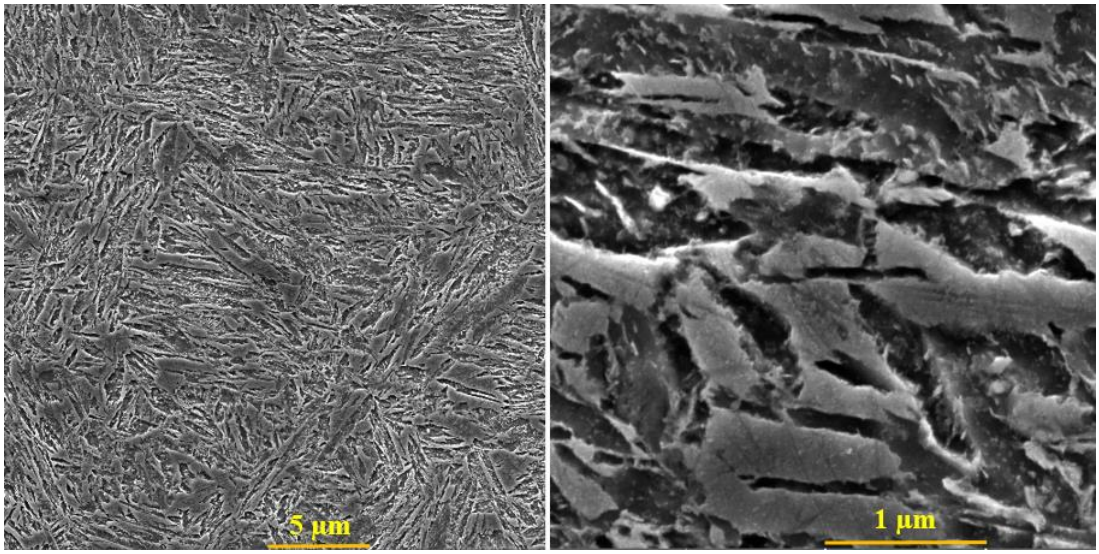

Figure 42. SEM images of the 1600 MPa nano-structured steel microstructure.

Table 13 details the results on the smooth tensile specimen in the air at room condition and indicates a nominal yield strength of 150 Ksi (1034 MPa) and an elongation of 12% of the original gauge length. The test performed with the specimen with a 10% notch suggest that the 1600 MPa nanostructured steel has a large capacity for strain hardening induced by the triaxle stress state due to the presence of the notch, **Figure 43**.

The analysis of the several notched tensile test performed on the 1600MPa nanostructured steel specimens in the air at room conditions, shows that ratio of the break stress to yield strength ($R=\sigma_b/\sigma_y$) s R=14, which is consistent with the expectation of large strain hardening due to concentrate plastic deformation at the notch. The analysis of the NTSSRT results for the 1600MPa nanostructured steel in the air at room condition was done using the J_{Ic} average method as indicated by the criterion described in the literature[105, 127, 133, 134].

Table 13. J_{ic} values obtained by the evaluation of the NTSSRT experiments on the 1600 MPa nanostructured steel in the air at room conditions.

Air test #	**Notch (%)**	**KI (ksi $in^{0.5}$)**
1	10	154
2	10	153
3	10	164
4	10	169
	average	162±6

The results of the different stress versus strain curves resulting from the NTSSRT experiments performed on the 1% NaCl brine under the different aqueous H_2S concentrations shown in **Figure 44**. Increase of H_2S content in the test brine reduces the fracture strength and elongation, which translates to loss of plasticity in the 1600Mpa nanostructured steel. However, we observed that for the H_2S concentrations of 10% and higher, the 1600 Mpa nanostructured steel exhibits an apparent increase in the strain hardening as shown by the steeper slope of the stress – strain curve. This effect can be due to the higher hydrogen diffusion rate. Further research is needed to measure the diffused hydrogen content. The effect of the H_2S content in the tests brine reduces the ratio of the break stress to tensile strength for the 1600Mpa nanostructured steel from R=14 in the air, to R=7 at 1% H_2S down to R=4 at 100% H_2S. The energy required to propagate a crack consistently decreases with the H_2S content in the brine. This behavior is consistent with

the expected effect of the embrittlement of the material due to hydrogen penetration. The evaluation of the fracture surfaces after testing shown in **Figure 6**, present the typical indications that crack propagation by SSCC occurred, although the transgranular evidence is found at higher magnification. From the J_I values shown in **Figure 44**, the K_{ISSCC} values for the 1600 MPa nanostructured steel can be estimated using the J_{ic} average method. Following the methodology proposed the results of the effect of the H_2S content in the test brine on the K_{ISSCC} values for the 1600 MPa nanostructured steel evaluated are shown in **Figure 18**.

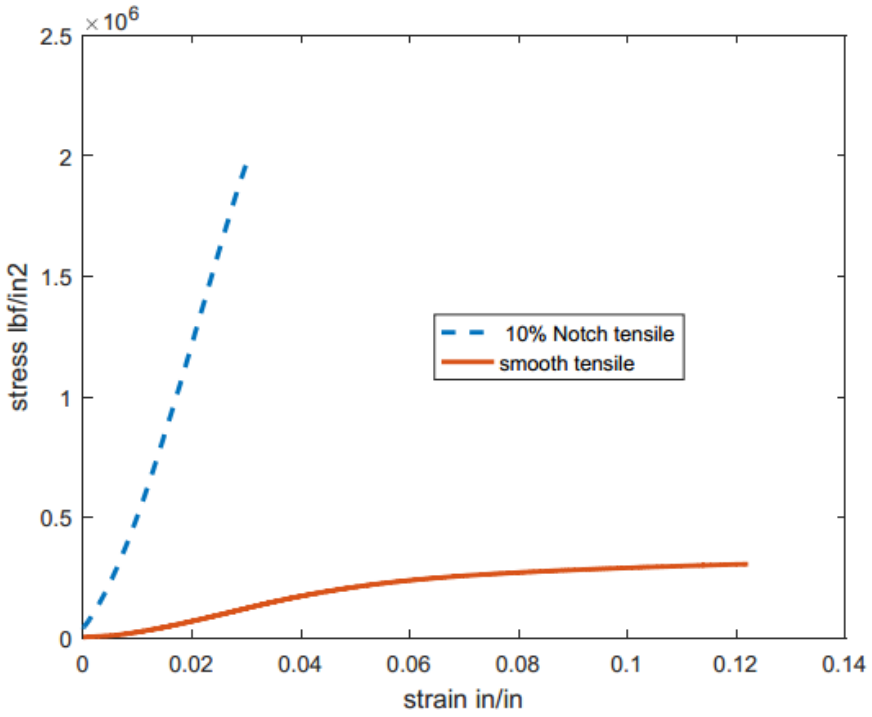

Figure 43. Stress strain curves for the 1600MPa nanostructured steel in air at room conditions showing the comparative effect of the notch on the resulting mechanical resistance.

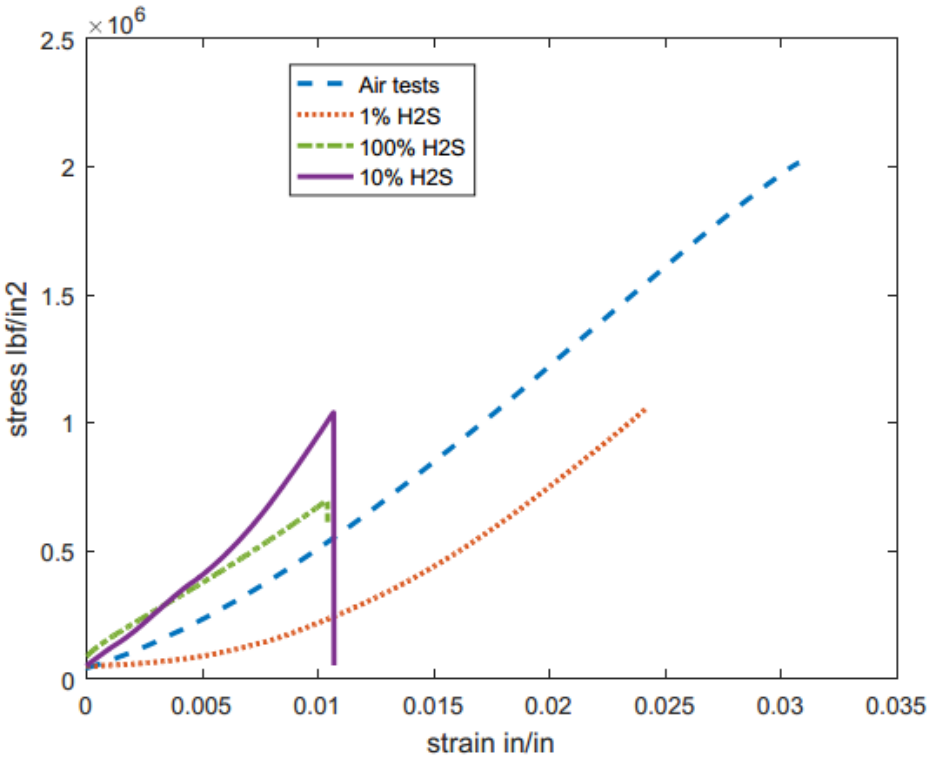

Figure 44. Effect of the H_2S content on the test brine on the stress – strain response from the NTSSRT experiments, (1 bar, 25°C).

The 1600Mpa nanostructured steel tested represents a new class of materials that have not been previously tested for SSCC susceptibility, hence to give an idea of the relative importance of the K_{ISSCC} values, shown in

Table 14, in terms of the performance is necessary to establish a comparison with another steel whose degree of susceptibility is known. Based on the Oil Country Tubular grade (OCTG) steel information available in the literature [112, 121, 135], the closest material in terms of mechanical performance to the 1600Mpa nanostructured steel is the API grade C110

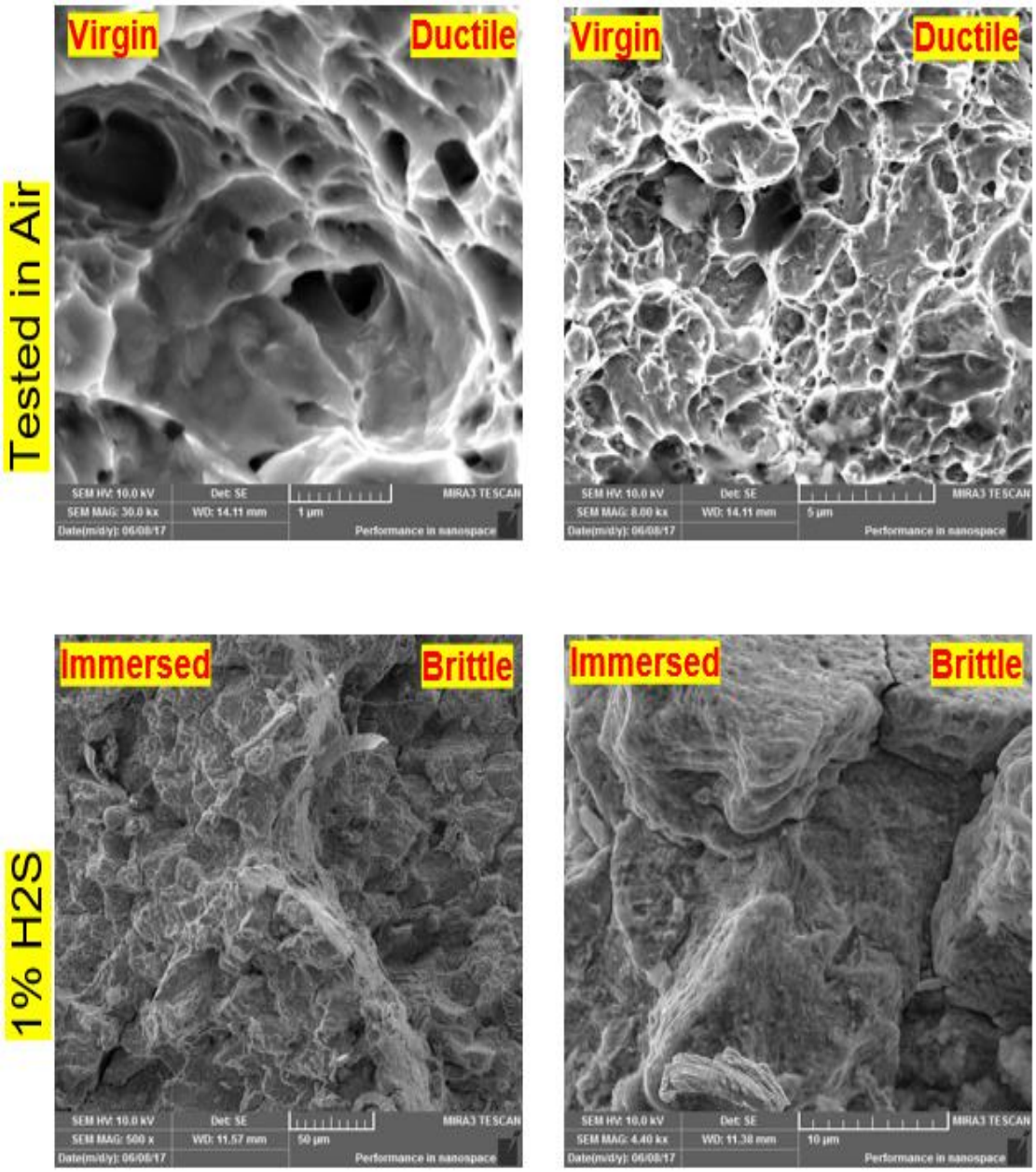

Figure 45. SEM images of fractures surfaces of the notch tensile specimen after failure.

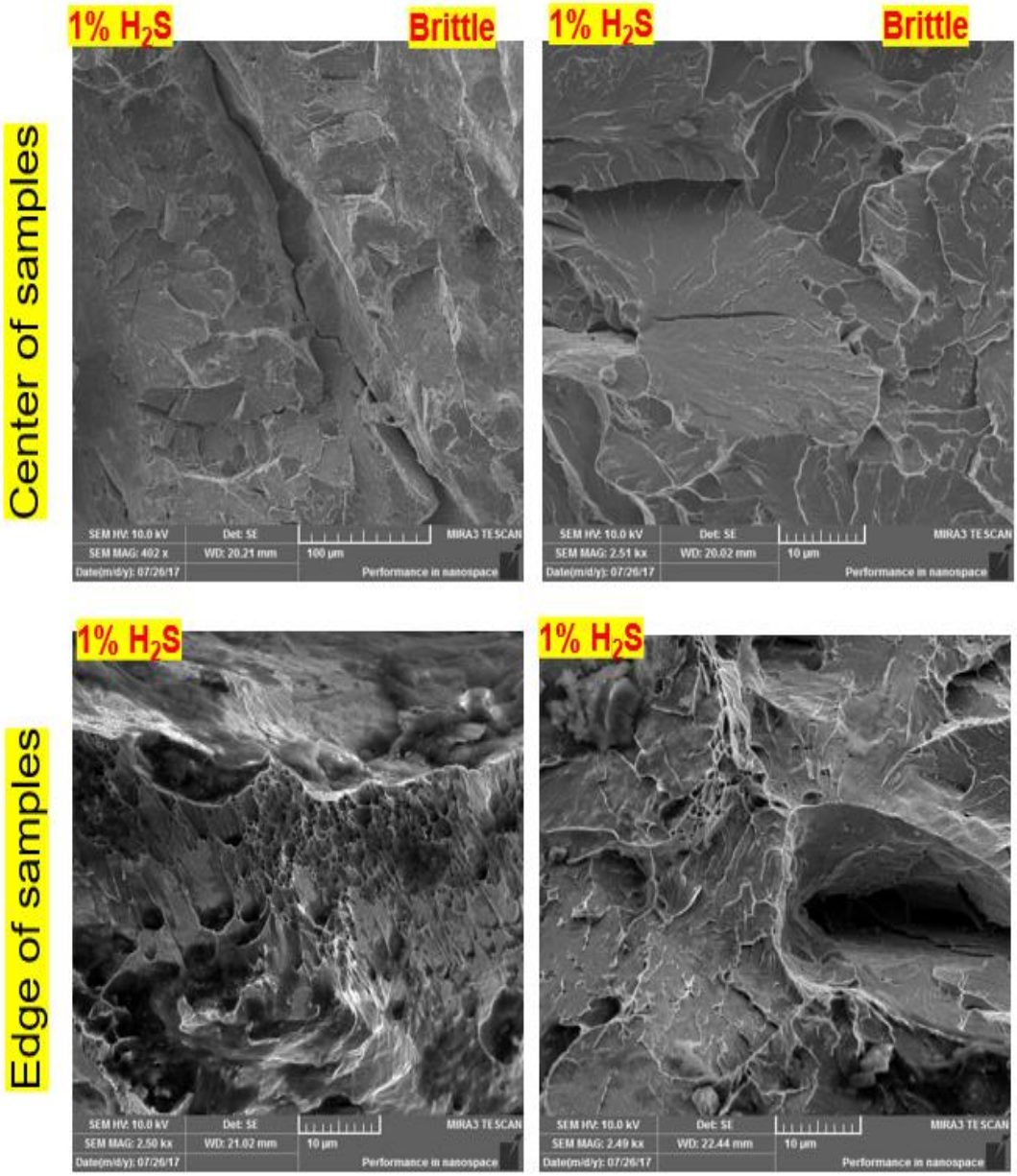

Figure 46. Center and edge of fracture surfaces of the notch tensile specimen after failure exposed to 1% H_2S.

Table 14. Effect of the H_2S content in the test brine on the KISSCC values using the NTSSRT method for the 1600 MPa nanostructured steel evaluated at room conditions.

Test condition	Notch (%)	K_{SSCC} (ksi inch$^{0.5}$)
pH 4.5-1% H_2S	10	107 ± 11
pH 4.5-10% H_2S	10	58 ± 7
pH 4.5-100% H_2S	10	42 ± 4

This steel grade is generally considered a sour service grade steel for the yield strength range up to 110- 120 ksi within the limitations imposed by the ISO 151516 standard[129]. The API C110 OCTG grade is a micro alloyed quench and double tempered steel, the susceptibility to SSCC of the C110 has been studied extensively in the literature [112, 114, 117, 121] either by the conventional NACE D method or the NTSSRT technique [135]. **Figure 47** illustrates the comparison between both materials, by showing the effect of the aqueous H_2S activity on the K_{ISSCC} values reported for the C110 grade steel by both methods with the results of the present study for the nanostructured steel (1600 MPa). The results presented in Figure 47for both steels are in brines at pH 4.5

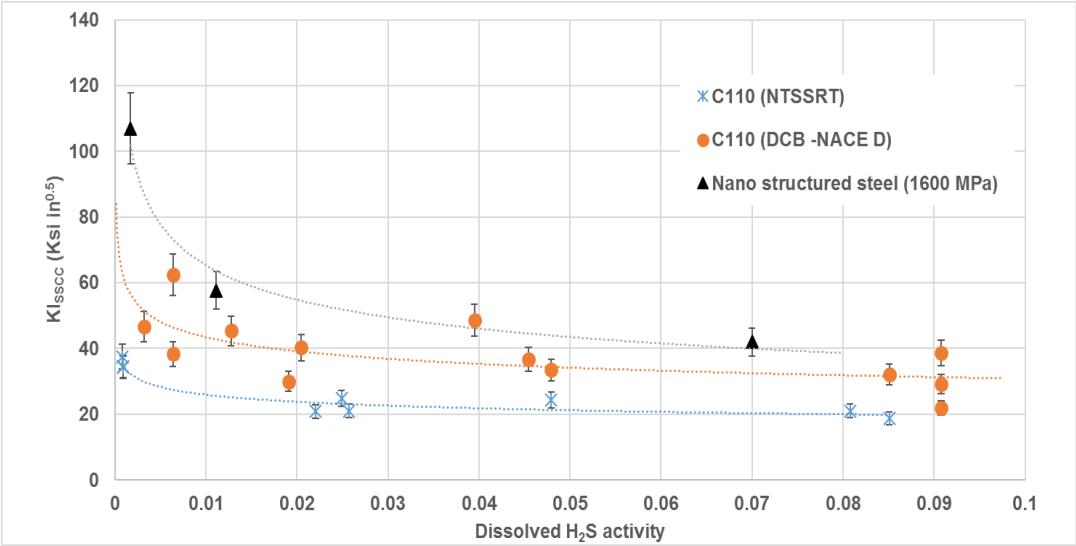

Figure 47. Effect of the dissolved H_2S activity on the KI_{SSCC} values for the C110 and the1600Mpa nanostructured steel in 1% NaCl brine at pH 4.5 in room conditions. The K_{ISSCC} values from DCB method D for C110 are reported in the literature [141].

4.2. 2000 MPa nanostructured steel susceptibility to hydrogen embrittlement

High strength steel is generally more susceptible to hydrogen embrittlement. As-quenched martensitic structure, due to its dense microstructure , appears to have the low hydrogen diffusivity and be most prone to hydrogen embrittlement [136, 137]. However, tempered bainite has a very high resistance against the hydrogen-induced ductility loss when compared to normalised ferrite/pearlite, quenched and tempered martensite and untempered martensite [138, 139]. Carbides in Bainite slow down hydrogen transport therefore specimens with fine carbides demonstrated highest hydrogen content[140]. The 2000 Mpa steel has a bainitic microstructure induced in a 0.47% C Fe–C alloy by a proprietary heat treatment including post tempering. Smooth specimens would behave differently compared with notched specimens. This section investigates the quantitative relationship between the fracture stress and hydrogen exposure time for both smooth and

notched specimens of 2000 MPa by means of slow strain rate tests. The effect of hydrogen on the fracture behavior of the steel is discussed. The susceptibility of various high strength steel microstructures were described previously. Hydrogen permeation tests showed that 2000 MPa specimens have the lowest effective diffusivity.

4.1.1 Experimental methodology

The 2000 MPa sheets in as received condition was cut by waterjet and then machined. 2.75in long tensile specimens with 1in gage length were prepared. **Figure 48** shows the dimensions of the sample. Smooth specimen has the gage diameter of 0.123" and 20 percent notched specimens had the gage diameter of 0.098" with 60°. We used electrochemical charging to introduce hydrogen to the samples. **Figure 49** shows the notched tensile specimen charging. Hydrogen was introduced by galvanostatic charging using 10 g /L sodium sulfide and 0.1 M sodium hydroxide as the solution. The specimens were pre-charged for 1, 24 and 48 hours at a current density of 3 mA/cm^2, before the actual NT-SSRT starts. Notched tensile specimens, which because of notch locally introduction of a triaxial stress state, were utilized to control the initiation of crack. Notched tensile SSRT experiments were conducted by strain rate of 10^{-6} s^{-1}. This specific geometrical discontinuity lead into a local stress concentration.

4.1.2 Results and discussion

The susceptibility of these specimens to hydrogen embrittlement is assessed by SSRT tests in situ hydrogen pre-charged specimens. Hydrogen embrittlement index was calculated for 1hr, 24hr and 48hr charging periods.

Loss in ductility in terms of J and ultimate tensile strength of the specimens were compared and correlated with the duration of charging. **Figure 53** shows the stress strain curve and the verified mechanical proprieties. Yield stress is 200 Ksi and modulus is $1.1x10^7$ psi.

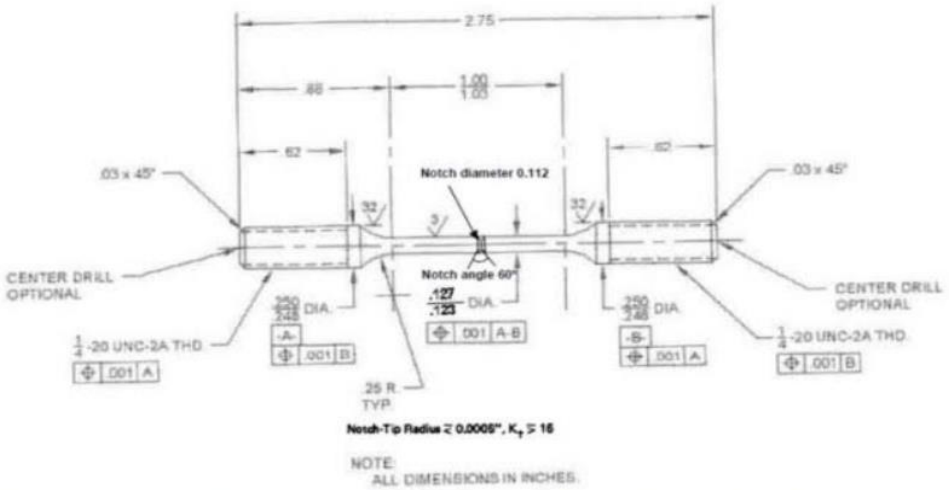

Figure 48. 20% Notch Tensile Specimen, 2000 MPa Nanostructured bainite Steel.

Fractography indicated that fracture surfaces become more brittle when the hydrogen charging duration increases. **Figure 50** demonstrates fracture surface of the 2000 MPa nanostructured notched 20% tensile specimen in air. The uncharged sample shows to be a ductile fracture. Micro-voids and dimples supports the failure of in a ductile mode. Increasing the hydrogen charging time leads to higher brittle percentage of fracture.

Figure 51 is the fracture surface of the 2000 MPa nanostructured notched 20% tensile specimen exposed to 24hr pre-charging. Cleavages in the fracture surface and inter-granular fractures are evident. **Figure 52** the 2000 MPa nanostructured notched 20% tensile specimen exposed to 48hr of pre-charging. Rivers on the fracture surface supports hydrogen embrittlement.

Figure 49. The 2000 MPa nanostructured steel notched tensile specimen while hydrogen charging.

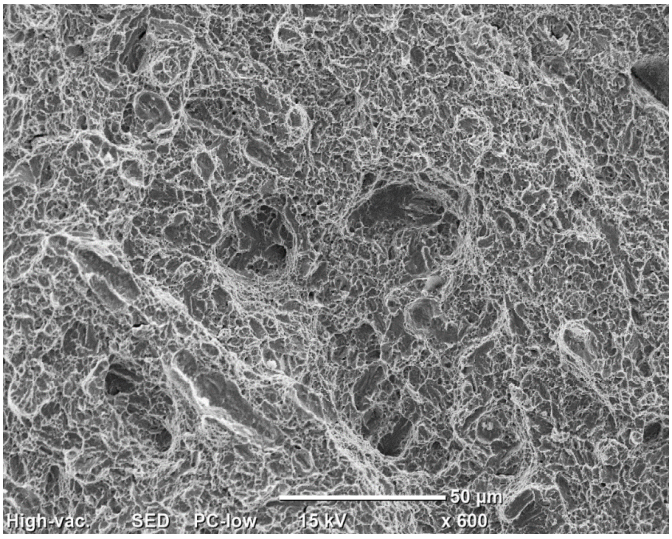

Figure 50. Fracture surface of the 2000 MPa nanostructured steel- air test.

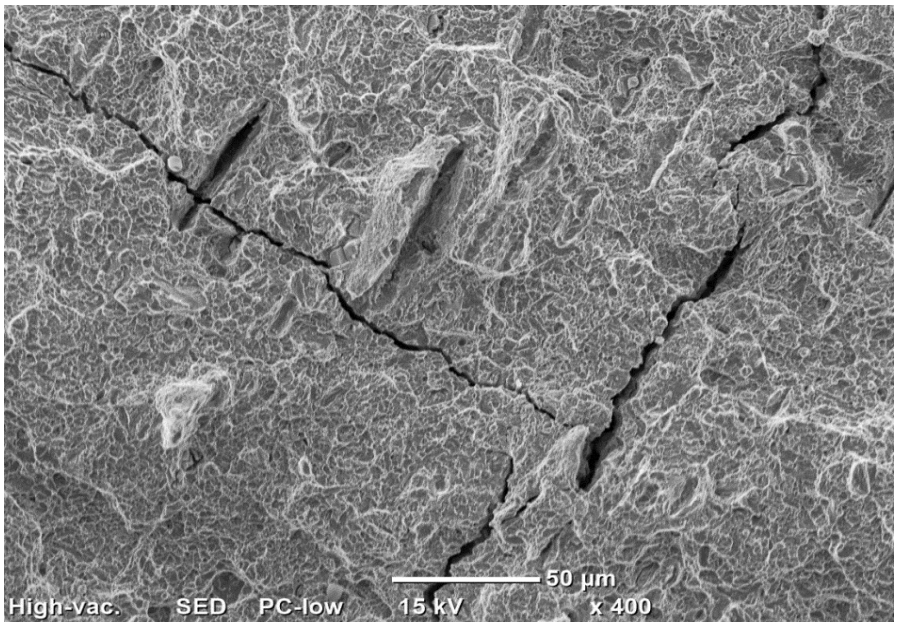

Figure 51. Fracture surface of the 2000 MPa nanostructured steel- 24hr hydrogen pre-charging.

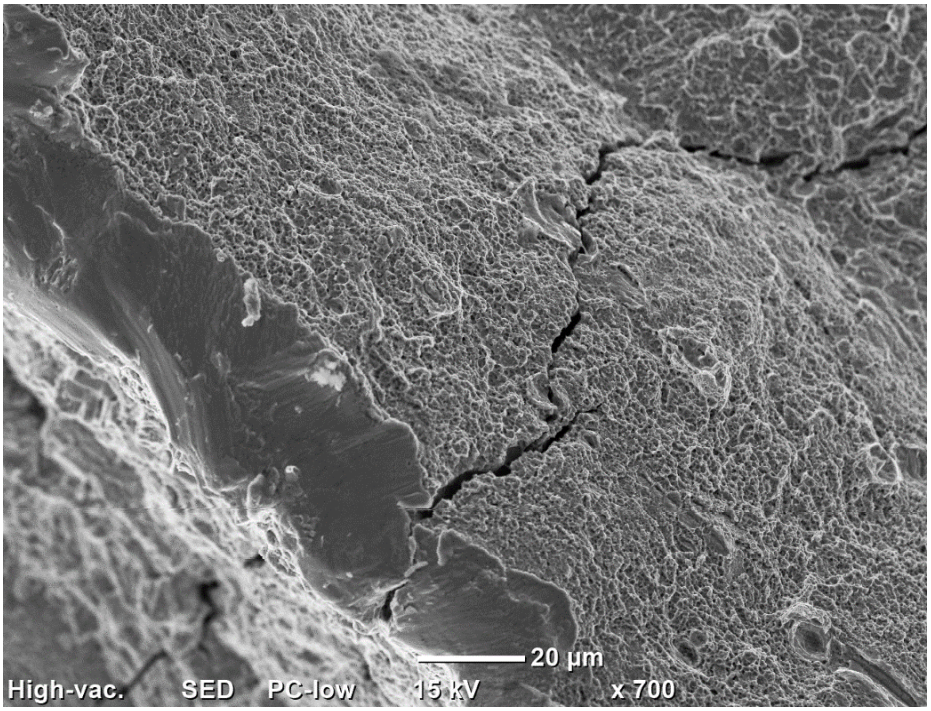

Figure 52. Fracture surface of the 2000 MPa nanostructured steel- 48hr hydrogen pre-charging.

After reviewing the qualitative fracture surfaces analysis, hydrogen embrittlement index is calculated to estimate the quantitative impact of hydrogen charging on the ductility of the 2000 MPa nano-structured bainitic steel. Lovicu et al. defined embrittlement index (EI) for hydrogen embrittlement for a notched sample, which implies the influence of HE on steel's strength[26].

$$\mathrm{HEI} = \frac{\text{Notched ultimale tensile strength}_{\text{no H}} - \text{Notched Ultimate Tensile Strength}_{\text{maxH}}}{\text{Notched ultimale tensile strength}_{\text{no H}}} * 100 \quad (36)$$

This approach does not take into account the elongation loss due to hydrogen embrittlement; however, many papers in the literature used it as an indicator of UTS loss. We determined the ultimate tensile strength of the 2000 MPa 20% notched tensile specimen as 255 Ksi without any pre-charging, **Figure 53**. Once we exposed the specimen to 1hr of hydrogen charging, the UTS dropped by 38%. 24hr of hydrogen pre-charging reduced the HEI by 52%, however, 48hr of pre-charging had negligible impact on any further significant reduction in HEI (53%). Despite the fact that 2000 MPa nanostructured steel has the highest strength and percentage of austenite (lowest hydrogen diffusivity of $4.23 \times 10^{-8}\ Cm^2.S^{-1}$), it is still showing some susceptibility to hydrogen embrittlement. **Figure 54** shows the decrease of calculated J integral.

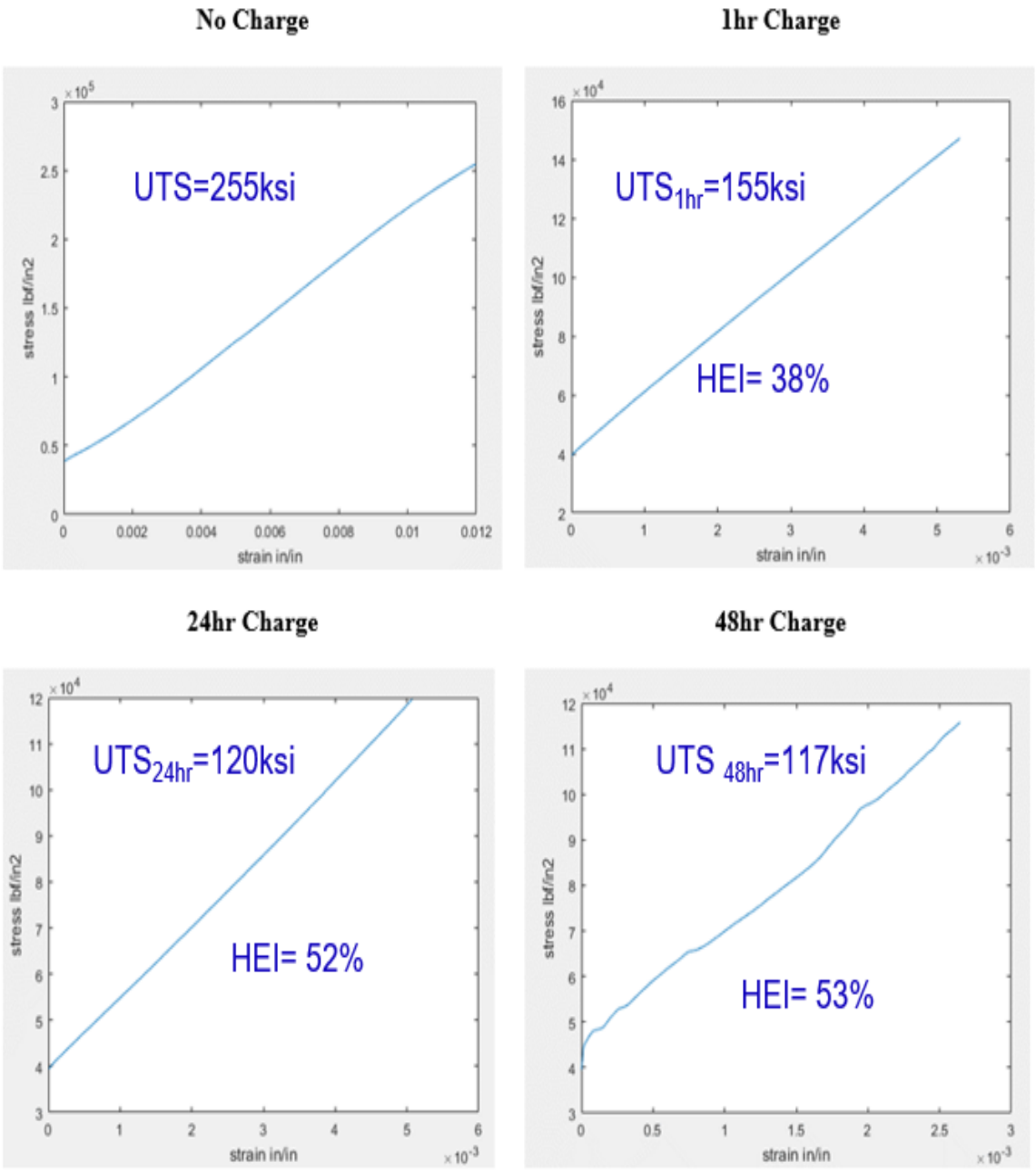

Figure 53. Stress Strain Curves of 20% Notched Samples: Hydrogen Embrittlement Index for exposed samples for 1hr, 24hr and 48hr versus air test.

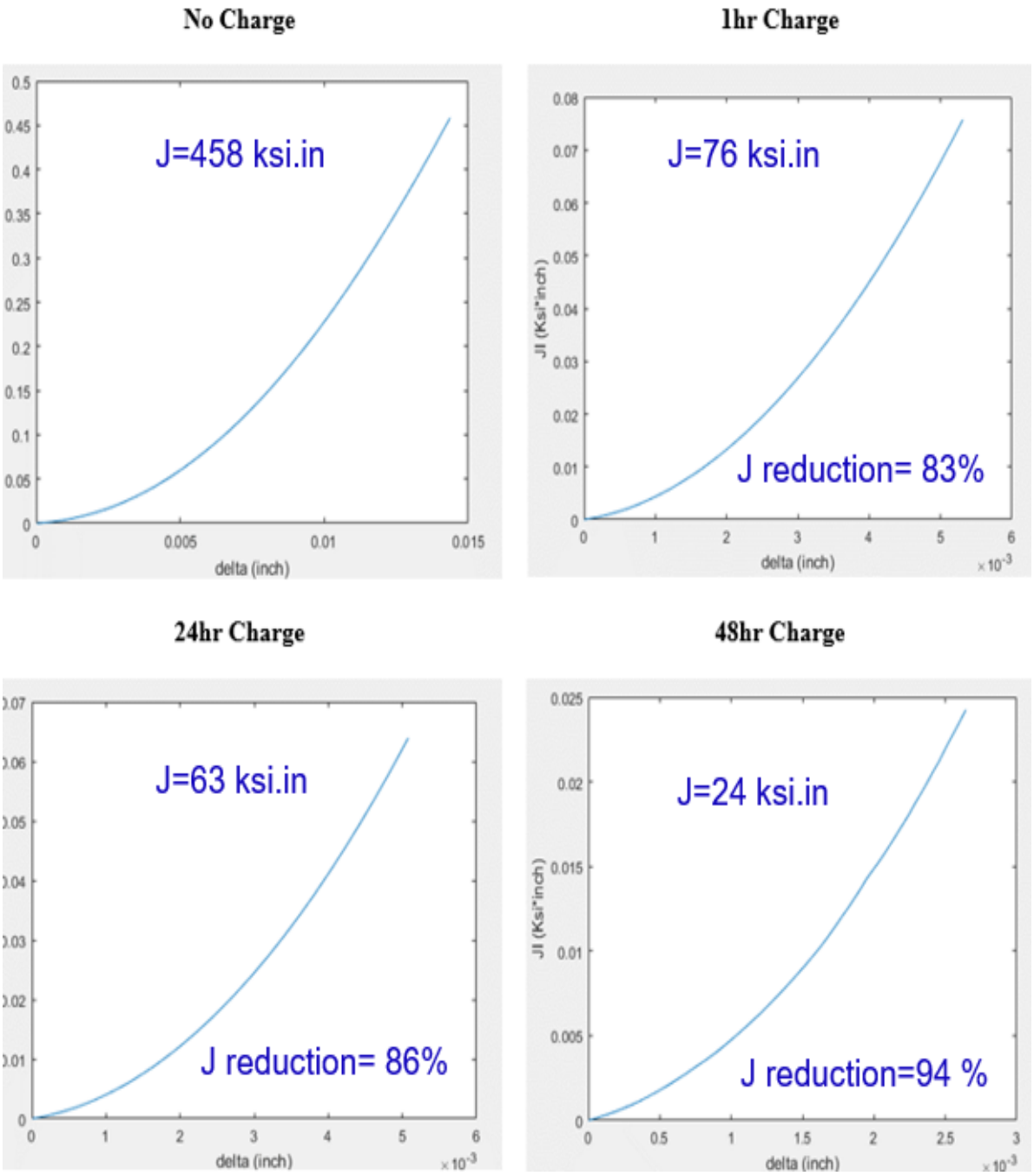

Figure 54. J curves for the 20% Notched samples: 1hr, 24hr and 48hr of hydrogen pre-charging versus air test.

4.3. Summary

- The NTSSRT testing as a technique provides more conservative values of the K_{ISSCC} parameter than the conventional DCB –NACE D method, as it can be appreciated from the results obtained in C110 steel.
- The 1600 MPa nanostructured steel exhibits a larger resistance to SSCC than the C110 in all the range of dissolved H_2S activities when tested using the NTSSRT method. The power law relationship between the K_{ISSCC} parameter and the aqueous H_2S activity, based on the description of the hydrogen damage mechanism, which controls the SSCC susceptibility in high strength steels [120, 141]. The trends lines illustrate the expected behavior of the K_{ISSCC} parameter across the all-possible values of the dissolved H_2S activity in the brine, **Figure 47**.
- For a given OCTG steel, we can use the 35 ksi $in^{0.5}$ criterion, which is considered as the threshold value of the K_{ISSCC} parameter above which a steel is immune to SSCC in practical terms. Based on this criterion it can be drawn that according to the values of the K_{ISSCC} parameter shown in Figure 12, the C110's performance steel is considered satisfactory at high H_2S activities (close to saturation at 100% H_2S). Following the same approach, it is clear that the 1600 Mpa nanostructured steel can also be considered sour service grade.
- The 2000 MPa nanostructured steel showed susceptibility to hydrogen embrittlement. The disperse and dense morphology of austenite in this microstructure reduces the diffusion relative to other classes of this steel. It's valuable to conduct NT-SSRT study on the 1000MPa and 1300 MPa and compare

the HEI for 1hr, 24hr and 48hr. This allows understanding the effect of austenite volume and morphology on the embrittlement of nanostructured steels. Due to unavailability of 1000 MPa and 2000 MPa materials we did not manage to conduct these experiments. We also need to investigate defects in the steel so we understand their contribution to hydrogen embrittlement susceptibility of nanostructured steel.

- We investigated the loss of UTS for the 20 percent notched nanostructured steel after being pre-charged for 1hr, 24hr and 48 hr. Higher charging time correlates with the introduction of higher concentration of hydrogen into the microstructure.
- We calculated the hydrogen embrittlement index. and it seems after 24 hrs of charging the majority of irreversible traps are filled. This is due to the reason that pre-charging for 48hrs barley made any difference in the HEI.
- The HEI could help determine a good safety factor for selection of this materials in applications where hydrogen could be introduced.
- A nonlinear fracture mechanics approach was used to calculate the J curves of the 2000 nanostructured steels. This approach was partially evaluated by building a finite element model, which was not included in this work. J curves takes into account the impacts of hydrogen embrittlement due to loss of UTS and elongation. On the contrary, HEI only offers a comparison based on UTS loss and is not sensitive to elongation loss.
- The majority of J reduction and HE index increase happened after one hour of hydrogen charging. One hour of charging does correlate with a critical hydrogen

concertation. After one hour of hydrogen charging filling certain number of irreversible traps were filled and this in turn aggressively embittered the 2000 MPa nanostructured steel.

5. CONCLUSION AND FUTURE WORK

- The 3rd generation nanostructured high strength steel investigated in this research have very small grains in order of 40 nm bainitic ferrite and 500nm-2 micron retained austenite. It not only provide strengths ranging from 1000 MPa to 2000 MPa but also it has reasonable ductility relative to other brittle high strength steels.
- Hydrogen embrittlement is one of the application challenges of using high strength steel. Delivery of hydrogen to critical regions of microstructure, such as a crack tip, is dependent on how diffusion takes place. Hydrogen diffusion through the microstructures of nanostructured bainitic high strength steels was studied by Devanathan–Stachurski cell.
- The microstructures are composed of various phase contents of retained austenite and bainitic ferrite. The retained austenite content along with its morphology predominantly influences the diffusion by providing higher number of traps with higher binding energy. Continuous blockade of hydrogen by thin austenitic films, besides higher ferrite austenite boundaries decrease the hydrogen diffusivity in nanostructured steels.
- Connectivity of the trap constituent morphology substantially affects the percolation of hydrogen and diffusion phenomena in this class of high strength steel. The majority of such traps are found to be more reversible traps than irreversible traps. Alloying the nanostructured bainitic steels played an important role in creating irreversible traps.

- Higher nickel and chromium improved the retained austenite formation and its stability was enhanced by higher Molybdenum content.
- The heat treatment of these samples impact the formation of unique microstructures. Smaller austenite fraction, below the percolation threshold, with higher mean free path result into higher hydrogen diffusivity. Hydrogen diffusivity of bainitic ferrite is less than ferrite. Higher volume of the retained austenite in isolation in the nanostructured bainitic steel does not produce lower diffusivity.
- We analyzed the chemical composition by EDS and WDS methods and researched the fracture surfaces of the 1000, 1300, 1600 and 2000 MPa nanostructured steel specimens after exposure to hydrogen charging various concentration of H_2S and hydrogen charging.
- We characterized the microstructure, crystal structure and morphologies created at the fracture surfaces of this material by SEM and AFM. Austenitic films and small blocks were revealed in the 2000 MPa, 1600 MPa and Austenitic granular block in 1300 MPa and 1000 MPa.
- We performed an experimental investigation by using NTSSRT techniques on specimens under
    - sour service conditions to quantify this materials susceptibility to SSCC and found out that:
    - The 1600 MPa nanostructured steel shows susceptibility to the hydrogen penetration damage produced by the presence of H_2S in brines with 1% NaCl

at pH 4.5, exhibiting a K_{ISSCC} value that decreases with the H_2S activity in the brine from 107 Ksi $in^{0.5}$ at 1% H_2S to 42 Ksi $in^{0.5}$ at 100% H_2S.

- The relative comparison with the C110 steel indicates that the 1600 MPa nanostructured steel exhibits a larger resistance to SSCC than the C110 in all the range of dissolved H_2S activities when tested using the NTSSRT method.
- Based on technical criterions the 1600 MPa nanostructured steel can be considered as sour service grade OCTG, since it can exhibit a K_{ISSCC} value higher than 35 Ksi $in^{0.5}$ when tested at high concentrations of H_2S consistent with a severe sour service environment (type 3 in the ISO 15156 diagram)

- The decohesion focused researchers used plasticity linked to advancement of a crack predominantly as a reason to produce adequately high stresses to draw the hydrogen amounts essential to cause the magnitude of bond strength decrease to induce failure. Nonetheless, this school of thought adopts that the influence of hydrogen on the deformation that took place before the failure is inconsequential to the entire embrittlement process.
- Any new HE mechanism has to consider the various features discovered nearby facture surface. HELP mechanism attribute the distinctive morphologies seen on the fracture surface to local conditions (e.g. state of stress).
- What is the threshold content of hydrogen, which would trigger inter-granular failure? Future research are vital to specify the degree of the cohesive strength decrease due to hydrogen in grain boundaries of various systems in which hydrogen stimulate an inter-granular fracture.

- Fractography with TEM plays a critical role for fracture surface analysis and topography as TEM could detects the small and shallow features better than SEM. The questions that could help advance this field are
    - What are the reasons behind inclination towards special crystallographic planes and directions which differs in different materials is dependent on the fracture mode) for brittle and quasi-brittle fractures?
- At equilibrium, hydrogen weakens the lattice bonds or grain boundaries cohesive energy, however, the main question to answer is about the degree of the reduction as a function of hydrogen content. It is also very challenging to discover the interactions of HE mechanisms during crack propagation in the nanostructured steel.
- Retained austenite enhances solubility of hydrogen and reduces hydrogen diffusivity because retained austenite captures hydrogen in an irreversible manner at room temperature. Adding Cr, Mo and Ni might amend cementite precipitation.
- It's valuable to conduct NT-SSRT study on the 1000MPa and 1300 MPa and compare the HEI for 1hr, 24hr and 48hr. This allows understanding the effect of austenite volume and morphology on the embrittlement of nanostructured steels.

REFERENCES

1. Pfeil, L., The effect of occluded hydrogen on the tensile strength of iron. Proceedings of the Royal Society of London. Series A, Containing Papers of a Mathematical and Physical Character, 1926. 112(760): p. 182-195.

2. Keeler, K., Mooney, P., Advanced High-Strength Steels Application Guidlines Version 6.0 (2017). World Auto Steel 2017 [cited 2017 24 December].

3. Tasan, C., et al., An overview of dual-phase steels: advances in microstructure-oriented processing and micromechanically guided design. Annual Review of Materials Research, 2015. 45: p. 391-431.

4. Krajewski, S. and Nowacki, J., Dual-phase steels microstructure and properties consideration based on artificial intelligence techniques. Archives of Civil and Mechanical Engineering, 2014. 14(2): p. 278-286.

5. Dini, G., et al., Predicting of mechanical properties of Fe–Mn–(Al, Si) TRIP/TWIP steels using neural network modeling. Computational Materials Science, 2009. 45(4): p. 959-965.

6. Srivastava, A., et al., Micromechanics of plastic deformation and phase transformation in a three-phase TRIP-assisted advanced high strength steel: Experiments and modeling. Journal of the Mechanics and Physics of Solids, 2015. 78: p. 46-69.

7. Aaronson, H., et al., Bainite viewed three different ways. Metallurgical Transactions A, 1990. 21(6): p. 1343-1380.

8. Bhadeshia, H., Prevention of hydrogen embrittlement in steels. ISIJ international, 2016. 56(1): p. 24-36.

9. Haezebrouck, D., Nucleation and growth of a single martensitic particle. 1987, Massachusetts Institute of Technology.

10. Swallow, E. and Bhadeshia, H., High resolution observations of displacements caused by bainitic transformation. Materials Science and Technology, 1996. 12(2): p. 121-125.

11. Singh, S., Mechanisms of bainite transformation in steels, in Phase Transformations in Steels. 2012, Elsevier. p. 385-416.

12. Chang, L. and Bhadeshia, H., Austenite films in bainitic microstructures. 1995. 11(9): p. 874-882.

13. Gourgues, A., H. Flower, and T. Lindley, Electron backscattering diffraction study of acicular ferrite, bainite, and martensite steel microstructures. Materials Science and Technology, 2000. 16(1): p. 26-40.

14. Lambert, G. and Kussell, E., Quantifying Selective Pressures Driving Bacterial Evolution Using Lineage Analysis. Physical Review X, 2015. 5(1).

15. Bhattacharjee, D., et al., Charpy-impact-toughness prediction using an "Effective" grain size for thermomechanically controlled rolled microalloyed steels. Metallurgical and Materials Transactions A, 2004. 35(1): p. 121-130.

16. Okamoto, H. and Oka, M., Lower bainite with midrib in hypereutectoid steels. Metallurgical Transactions A, 1986. 17(7): p. 1113-1120.

17. Gleiter, H., Nanocrystalline materials, in Advanced Structural and Functional Materials. 1991, Springer. p. 1-37.

18. Valiev, R.Z., et al., Structural strength and corrosion resistance of nanostructured steel 10. Steel in Translation, 2014. 44(6): p. 418-421.

19. Nakashima, K., et al., Development of a multi-pass facility for equal-channel angular pressing to high total strains. Materials Science and Engineering: A, 2000. 281(1-2): p. 82-87.

20. Kamachi, M., et al., Equal-channel angular pressing using plate samples. Materials Science and Engineering: A, 2003. 361(1-2): p. 258-266.

21. Tsuji, N., et al., ARB (Accumulative Roll-Bonding) and other new techniques to produce bulk ultrafine grained materials. Advanced Engineering Materials, 2003. 5(5): p. 338-344.

22. Caballero, F., et al., Atomic scale observations of bainite transformation in a high carbon high silicon steel. Acta materialia, 2007. 55(1): p. 381-390.

23. Garcia-Mateo, C., et al., Development of hard bainite. ISIJ international, 2003. 43(8): p. 1238-1243.

24. Committee, A.I.H., ASM handbook: Materials selection and design. Vol. 20. 1997: CRC Press.

25. Nagumo, M., Function of hydrogen in embrittlement of high-strength steels. ISIJ international, 2001. 41(6): p. 590-598.

26. Lovicu, G., et al., Hydrogen Embrittlement of Automotive Advanced High-Strength Steels. Metallurgical and Materials Transactions A, 2012. 43(11): p. 4075-4087.

27. Michler, T. and Naumann, J., Influence of high pressure hydrogen on the tensile and fatigue properties of a high strength Cu–Al–Ni–Fe alloy. international journal of hydrogen energy, 2010. 35(20): p. 11373-11377.

28. Thomas, R.L., et al., Trap-governed hydrogen diffusivity and uptake capacity in ultrahigh-strength AERMET 100 steel. Metallurgical and Materials Transactions A, 2002. 33(7): p. 1991-2004.

29. Eliaz, N., et al., Characteristics of hydrogen embrittlement, stress corrosion cracking and tempered martensite embrittlement in high-strength steels. Engineering Failure Analysis, 2002. 9(2): p. 167-184.

30. Krom, A., and Bakker, A., Hydrogen trapping models in steel. Metallurgical and materials transactions B, 2000. 31(6): p. 1475-1482.

31. Kazum, O., et al., Hydrogen permeation in nanostructured bainitic steel. Metallurgical and Materials Transactions A, 2016. 47(10): p. 4896-4903.

32. Pound, B., The effect of aging on hydrogen trapping in precipitation-hardened alloys. Corrosion science, 2000. 42(11): p. 1941-1956.

33. Tsay, L.W., et al., Hydrogen embrittlement susceptibility and permeability of two ultra-high strength steels. Corrosion Science, 2006. 48(8): p. 1926-1938.

34. Arafin, M. and Szpunar, J., Effect of bainitic microstructure on the susceptibility of pipeline steels to hydrogen induced cracking. Materials Science and Engineering: A, 2011. 528(15): p. 4927-4940.

35. Perez, T., et al., The Effect of Notch Configuration on NACE TM0177 DCB Elastic Compliance and Recommendations for Future Testing, in CORROSION 2016. 2016, NACE International: Vancouver, CA.

36. Frappart, S., et al., Study of the hydrogen diffusion and segregation into Fe–C–Mo martensitic HSLA steel using electrochemical permeation test. Journal of Physics and Chemistry of Solids, 2010. 71(10): p. 1467-1479.

37. Frappart, S., et al., Hydrogen solubility, diffusivity and trapping in a tempered Fe–C–Cr martensitic steel under various mechanical stress states. Materials Science and Engineering: A, 2012. 534: p. 384-393.

38. Noreña, C. and Bruzzoni, P., Effect of microstructure on hydrogen diffusion and trapping in a modified 9% Cr–1% Mo steel. Materials Science and Engineering: A, 2010. 527(3): p. 410-416.

39. Crolet, J. and Bonis, M., Revisiting Hydrogen in steel, Part I: Theoretical Aspects of Charging , Stress Corrosion Cracking and Permeation in Corrosion 2001. NACE International.

40. Owczarek, E. and Zakroczymski, T., Hydrogen transport in a duplex stainless steel. Acta materialia, 2000. 48(12): p. 3059-3070.

41. Addach, H., et al., Study of the electrochemical permeation of hydrogen in iron. Corrosion Science, 2009. 51(2): p. 263-267.

42. Kittel, J., et al., Effect of membrane thickness on hydrogen permeation in steels during wet hydrogen sulfide exposure. Corrosion Science, 2008. 64(10): p. 788-799.

43. Dean, F., Measurement of hydrogen permeation through structural steel sections of varying thickness at 19°C. Materials science and technology, 2005. 21(3): p. 347-351.

44. Lee, J., Hydrogen trapping in AISI 4340 steel. Metal Science, 1983. 17(9): p. 426-432.

45. Pound, B., Hydrogen trapping in high-strength steels. Acta materialia, 1998. 46(16): p. 5733-5743.

46. Toyoda, S., et al., Effects of Cu addition on hydrogen absorption and diffusion properties of 1470 MPa grade thin-walled steel in a solution of HCl. ISIJ international, 2011. 51(3): p. 456-461.

47. L.A.Skogsberg, et al., Effect of Thiocyanate on Stress Corrosion Cracking of Corrosion Resistant Alloys in Halide Brines, in Corrosion 2013. 2013, NACE International: Orlando, FL.

48. Li, D., et al., Hydrogen trap states in ultrahigh-strength AERMET 100 steel. Metallurgical and materials transactions A, 2004. 35(3): p. 849-864.

49. Thomas, et al., Internal hydrogen embrittlement of ultrahigh-strength AERMET 100 steel. Metallurgical and Materials Transactions A, 2003. 34(2): p. 327-344.

50. Tetelman, A. and Robertson, W., Direct observation and analysis of crack propagation in iron-3% silicon single crystals. Acta Metallurgica, 1963. 11(5): p. 415-426.

51. Lynch, S., Hydrogen embrittlement phenomena and mechanisms. 2012.

52. Lynch, S. and Moutsos, S., A brief history of fractography. Journal of Failure Analysis and Prevention, 2006. 6(6): p. 54-69.

53. Oriani, R. and Josephic, P., Equilibrium aspects of hydrogen-induced cracking of steels. Acta Metallurgica, 1974. 22(9): p. 1065-1074.

54. Troiano, A., Embrittlement by hydrogen and other interstitials. Metal Progress, 1960: p. 112-117.

55. Gerberich, W., Modeling hydrogen induced damage mechanisms in metals, in Gaseous Hydrogen Embrittlement of Materials in Energy Technologies: Mechanisms, Modelling and Future Developments. 2012, Elsevier. p. 209-246.

56. Beachem, C., A new model for hydrogen-assisted cracking (hydrogen "embrittlement"). Metallurgical transactions, 1972. 3(2): p. 441-455.

57. Ferreira, P., Robertson, I. and Birnbaum, H., Hydrogen effects on the interaction between dislocations. Acta materialia, 1998. 46(5): p. 1749-1757.

58. Birnbaum, H. and Sofronis, P., Hydrogen-enhanced localized plasticity—a mechanism for hydrogen-related fracture. Materials Science and Engineering: A, 1994. 176(1-2): p. 191-202.

59. Song, J. and Curtin, W., A nanoscale mechanism of hydrogen embrittlement in metals. Acta Materialia, 2011. 59(4): p. 1557-1569.

60. Song, J. and Curtin, W., Atomic mechanism and prediction of hydrogen embrittlement in iron. Nature materials, 2013. 12(2): p. 145-151.

61. Barnoush, A., Hydrogen embrittlement, in Saarland University. 2011.

62. Ronevich, J., et al., Hydrogen effects in prestrained transformation induced plasticity steel. Metallurgical and Materials Transactions A, 2012. 43(7): p. 2293-2301.

63. Zhong, N., et al., Enhancement of the mechanical properties of a Nb-microalloyed advanced high-strength steel treated by quenching–partitioning–tempering process. Materials Science and Engineering: A, 2009. 506(1): p. 111-116.

64. Rehrl, J., et al., The impact of Nb, Ti, Zr, B, V, and Mo on the hydrogen diffusion in four different AHSS/UHSS microstructures. steel research international, 2014. 85(3): p. 336-346.

65. Takai, K., et al., Effect of Si and Ca addition on delayed fracture of high-strength steels. Tetsu-to-Hagané, 1993. 79(6): p. 685-691.

66. Gangloff, R. and Somerday, B., Gaseous hydrogen embrittlement of materials in energy technologies: mechanisms, modelling and future developments. 2012: Elsevier.

67. Turnbull, A. and Hutchings, R., Analysis of hydrogen atom transport in a two-phase alloy. Materials Science and Engineering: A, 1994. 177(1-2): p. 161-171.

68. Park, Y., et al., Retained austenite as a hydrogen trap in steel welds. Welding Journal-New York-, 2002. 81(2): p. 27-S.

69. Robertson, I., et al., Hydrogen Embrittlement Understood. Metallurgical and Materials Transactions B, 2015. 46(3): p. 1085-1103.

70. Michalska, J., Sozańska, M., and Hetmańczyk, M., Application of quantitative fractography in the assessment of hydrogen damage of duplex stainless steel. Materials Characterization, 2009. 60(10): p. 1100-1106.

71. ASTM E112-13, Standard Test Methods for Determining Average Grain Size, ASTM International, West Conshohocken, PA. 2013.

72. Caballero, F., et al., Design of advanced bainitic steels by optimisation of TTT diagrams and T0 curves. ISIJ international, 2006. 46(10): p. 1479-1488.

73. Garcia-Mateo, C., et al., Tensile behaviour of a nanocrystalline bainitic steel containing 3 wt% silicon. Materials Science and Engineering: A, 2012. 549: p. 185-192.

74. García-Mateo, C. and Caballero, F., The role of retained austenite on tensile properties of steels with bainitic microstructures. Materials Transactions, 2005. 46(8): p. 1839-1846.

75. Garcia, C. and Caballero, F., Ultra-high-strength bainitic steels. ISIJ international, 2005. 45(11): p. 1736-1740.

76. Caballero, F., et al., Effects of morphology and stability of retained austenite on the ductility of TRIP-aided bainitic steels. ISIJ international, 2008. 48(9): p. 1256-1262.

77. Garcia-Mateo, C., et al., Mechanical stability of retained austenite during plastic deformation of super high strength carbide free bainitic steels. Journal of materials science, 2009. 44(17): p. 4617-4624.

78. Morales-Rivas, L., et al., Nanomechanical characterization of nanostructured bainitic steel: Peak Force Microscopy and Nanoindentation with AFM. Sci Rep, 2015. 5: p. 17164.

79. Bhadeshia, H. and Christian, J., Bainite in steels. Metallurgical transactions A, 1990. 21(3): p. 767-797.

80. Pressouyre, G. and Bernstein, I., An example of the effect of hydrogen trapping on hydrogen embrittlement. Metallurgical Transactions A, 1981. 12(5): p. 835-844.

81. Pressouyre, G., A classification of hydrogen traps in steel. Metallurgical and Materials Transactions A, 1979. 10(10): p. 1571-1573.

82. Nelson, H., Hydrogen embrittlement. Treatise on materials science and technology, 1983. 25: p. 275-359.

83. Brass, A. and Chanfreau, A., Electrochemical permeation of hydrogen in high purity nickel at 100 C. Scripta Metallurgica et Materialia, 1990. 24(3): p. 499-504.

84. Wert, C., Trapping of hydrogen in metals, in Hydrogen in Metals II. 1978, Springer. p. 305-330.

85. Yao, J. and Cahoon, J., Theoretical modeling of gain boundary diffusion of hydrogen and its effect on permeation curves. Acta metallurgica et materialia, 1991. 39(1): p. 111-118.

86. Calder, R., Elleman, T., and Verghese, K., Grain boundary diffusion of tritium in 304-and 316-stainless steels. Journal of Nuclear Materials, 1973. 46(1): p. 46-52.

87. Yazdipour, N., et al., 2D modelling of the effect of grain size on hydrogen diffusion in X70 steel. Computational Materials Science, 2012. 56: p. 49-57.

88. Huang, F., et al., Effect of microstructure and inclusions on hydrogen induced cracking susceptibility and hydrogen trapping efficiency of X120 pipeline steel. Materials Science and Engineering: A, 2010. 527(26): p. 6997-7001.

89. Lee, S.M. and Lee, J.Y., The effect of the interface character of TiC particles on hydrogen trapping in steel. Acta Metallurgica, 1987. 35(11): p. 2695-2700.

90. Garet, M., et al., Hydrogen trapping on non metallic inclusions in Cr-Mo low alloy steels. Corrosion Science, 1998. 40(7): p. 1073-1086.

91. Pressouyre, G. and Bernstein, I., A quantitative analysis of hydrogen trapping. Metallurgical transactions A, 1978. 9(11): p. 1571-1580.

92. Stevens, M. and Bernstein, I., Microstructural trapping effects on hydrogen induced cracking of a microalloyed steel. Metallurgical Transactions A, 1989. 20(5): p. 909-919.

93. Yuan, X., Precipitates and hydrogen permeation behavior in ultra-low carbon steel. Materials Science and Engineering: A, 2007. 452: p. 116-120.

94. Fielding, L., et al., Hydrogen diffusion and the percolation of austenite in nanostructured bainitic steel. Proceedings of the Royal Society A: Mathematical, Physical and Engineering Sciences, 2014. 470(2168): p. 20140108-20140108.

95. Hirth, J., Effects of hydrogen on the properties of iron and steel. Metallurgical Transactions A, 1980. 11(6): p. 861-890.

96. Xiukui, S., Jian, X., and Yiyi, L., Hydrogen permeation behaviour in austenitic stainless steels. Materials Science and Engineering: A, 1989. 114: p. 179-187.

97. G148-97, A., Standard practice for evaluation of hydrogen uptake, permeation, and transport in metals by an electrochemical technique. ASTM Int, 2011. 1: p. 1-10.

98. Yen, S. and Huang, I., Critical hydrogen concentration for hydrogen-induced blistering on AISI 430 stainless steel. Materials Chemistry and Physics, 2003. 80(3): p. 662-666.

99. Kiuchi, K. and McLellan, R., The solubility and diffusivity of hydrogen in well-annealed and deformed iron, in Perspectives in Hydrogen in Metals. 1986, Elsevier. p. 29-52.

100. Dong, C., et al., Hydrogen-induced cracking and healing behaviour of X70 steel. Journal of alloys and compounds, 2009. 484(1-2): p. 966-972.

101. Ali, M., Testing Techniques for Establishing Fracture Resistance of Steel in a Sour Environment. in ASME 2017 36th International Conference on Ocean, Offshore and Arctic Engineering. 2017. American Society of Mechanical Engineers.

102. Fujii, T., et al., Fracture mechanics study on stress corrosion cracking behavior under corrosive environment. Journal of Solid Mechanics and Materials Engineering, 2013. 7(3): p. 341-356.

103. Tanaka, K. and Harrison, J., An R curve approach to COD and J for an austenitic steel. International Journal of Pressure Vessels and Piping, 1978. 6(3): p. 177-201.

104. Rihan, R., Raman, R. and Ibrahim, R., Circumferential notch tensile (CNT) tests for determination of K1scc, using small fracture mechanics specimens, in New Test Methods for SCC Studies. 2008. p. 459-469.

105. Itoh, T., Approximate formulae for estimating the J-integral of a circumferentially cracked round bar under tension or torsion. Engineering Fracture Mechanics, 1988. Vol. 31.(No. 6,): p. pp. 967-975.

106. Kussmaul, K., et al., The transferability of elastic-plastic fracture mechanics parameters from CT-speciments to round notched tensile specimens. Nuclear Engineering and Design, 1984. 79(1): p. 1-6.

107. Zhong, X., Bali, S., and Shoji, T., Effects of dissolved hydrogen and surface condition on the intergranular stress corrosion cracking initiation and short crack growth behavior of non-sensitized 316 stainless steel in simulated PWR primary water. Corrosion Science, 2017. 118: p. 143-157.

108. Le Manchet, S., et al. Stress Oriented Hydrogen Induced Cracking Resistance of ASTM A516 Grade 70 Carbon-Manganese Steel for Oil & Gas Applications. in corrosion 2017. 2017. NACE International.

109. International, A., Standard Guide for On-Line Monitoring of Corrosion in Plant Equipment (Electrical and Electrochemical Methods). 2001: ASTM International, 100 Barr Harbor Drive, PO Box C700, West Conshohocken, PA 19428-2959, United States.

110. Okonkwo, P., et al. Corrosion Behavior of API X-80 Steel in Hydrogen Sulfide Environment at Different Temperatures. in corrosion 2016. 2016. NACE International.

111. Thodla, R., Hawk, J., and Ziomek-Moroz, M., Sour Service Fatigue and Fracture Behavior of High Strength Steels, in corrosion 2016. 2016, NACE International: Vancouver, CA.

112. Sagara, M., et al., Evaluation of Susceptibility to Hydrogen Embrittlement of High Strength Corrosion Resistant Alloys, in corrosion 2016. 2016, NACE International: Vancouver, CA.

113. Byrne, G., Francis, R., and Warburton, G., Hydrogen Induced Stress Cracking (HISC) Resistance and Improvement Methods for Super Duplex Stainless Steels, in CORROSION 2016. 2016, NACE International: Vancouver, CA.

114. Kumar, A., et al., Selecting Representative Laboratory Test Conditions for Mildly Sour Sulfide Stress Corrosion (SSC) Testing, in corrosion 2014. 2014, NACE International: San Antonio, TX.

115. Gingell, A. and Garat, X., The Role of Microstructure in Sulfide Stress Cracking Resistance of Thermomechanically Processed High Strength Low Alloy Steels, in Advances in Corrosion Control and Materials in Oil and Gas Production, P.S. Jackman and L.M. Smith, Editors. 1999, European Federation of Corrosion.

116. Echaniz, G., et al., The Effect of Microstructure on the K_{Issc} of Low Carbon Low Alloy Steels, in Advances in Corrosion Control and Materials in Oil and Gas Production, P.S. Jackman and L.M. Smith, Editors. 1999, European Federation of Corrosion.

117. Turconi, G., et al., Improvement of Resistance to SSC Initiation and Propagation of High Strength OCTG Through Microstructure and Precipitation Control, in corrosion 2001, N. International, Editor. 2001.

118. Nath, S. and Das, U., Effect of microstructure and notches on the fracture toughness of medium carbon steel. Journal of naval architecture and marine engineering, 2006. 3(1): p. 15-22.

119. Kim, S., et al., Effect of Microstructure on Hydrogen Induced Cracking and Sulfide Stress Cracking Property of Pressure Vessel Steel in Sour Environment, in corrosion 2012. 2012, NACE International: Salt Lake city, UT.

120. Cancio, M., et al., Environmental And Metallurgical Parameters Affecting Sulfide Stress Cracking Resistance Of High Strength Steels, in corrosion 2010. 2010, NACE International: Houston, TX.

121. Perez, T., et al., Development of a 110 ksi Yield Strength Grade OCTG Product for Shale Applications in Mildly Sour Environments, in corrosion 2013. 2013, NACE International: Orlando, FL.

122. Gomez-Duran, M. and Macdonald, D., Stress corrosion cracking of sensitized Type 304 stainless steel in thiosulphate solution. II. Dynamics of fracture. Corrosion Science, 2006. 48(7): p. 1608-1622.

123. Kondo, K., et al., Effect of Crack Starter on K1ssc and Compliance for DCB test, in corrosion 2014. 2014, NACE International: San Antonio, TX.

124. Dietzel, W., The Use of Crack-Tip Opening Displacement for Testing of the Hydrogen Embrittlement of High-Strength Steels. Materials Science, 2004. Vol. 40(No. 6): p. 749-755.

125. Rapid Inexpensive tests for determining fracture toughness, ed. N.M.A. Board. 1976, Washington, D.C.: National Academy of Sciences.

126. Rice, J., A Path Independent Integral and the Approximate Analysis of Strain Concentration by Notches and Cracks. Journal of Applied Mechanics,, 1968. Vol. 35: p. pp. 379-386.

127. Shindo, Y., et al., Cryogenic Fracture Toughness Determination of a Structural Alloy Weldment by Notch Tensile Measurement and Finite Element Analysis. Journal of Engineering Materials and Technology, 2001. 123(1): p. 45.

128. Mclntyre, D., et al., Slow Strain Rate Testing for Materials Evaluation in High-Pressure H2S Environments. corrosion, 1988. Vol. 44(No. 12): p. 920-926.

129. ANSI/NACE, Petroleum and natural gas industries — Materials for use in H2S-containing environments in oil and gas production — Part 2: Cracking-resistant carbon and low-alloy steels, and the use of cast irons, in MR0175/ISO 15156-2. 2009.

130. Itoh, Y., et al., Approximate formulae for estimating the J-integral of a circumferentially cracked round bar under tension or torsion. Engineering fracture mechanics, 1988. 31(6): p. 967-975.

131. NACE, A., TM0177-2016 Laboratory Testing of Metals for Resistance to Sulfide Stress Cracking and Stress Corrosion Cracking in H2S. 2016, NACE International: Houston, TX.

132. Rumann, A., ASTM E8 Tensile Strength Tests for VYKON 1000 and VYKON 2000. 2016, Vodik.

133. McIntyre, D., et al., Slow strain rate testing for materials evaluation in high-pressure H2S environments. Corrosion, 1988. 44(12): p. 920-926.

134. ANSI/NACE, Petroleum and natural gas industries —Materials for use in H_2S-containing environments in oil and gas production —Part 1: General principles for selection of cracking-resistant materials, in MR0175/ISO 15156-1. 2009.

135. Case, R., et al., Effect of Brine Ionic Strength on Sulfide Stress Cracking Resistance of High Strength Low Alloy Steel, in corrosion 2016. 2016, NACE International: Vancouver, CA.

136. Chan, S., Hydrogen trapping ability of steels with different microstructures. Journal of the Chinese institute of engineers, 1999. 22(1): p. 43-53.

137. Snape, E., Roles of composition and microstructure in sulfide cracking of steel. Corrosion, 1968. 24(9): p. 261-282.

138. Thompson, A. and Bernstein, I., The role of metallurgical variables in hydrogen-assisted environmental fracture, in Advances in corrosion science and technology. 1980, Springer. p. 53-175.

139. Fujita, T. and Yamada, Y., Physical metallurgy and SCC in high strength steels. Stress corrosion cracking and hydrogen embrittlement of iron base alloys, 1973: p. 736-746.

140. Tau, L., et al., Hydrogen enhanced fatigue crack propagation of bainitic and tempered martensitic steels. Corrosion science, 1996. 38(11): p. 2049-2060.

141. Cravero, S., et al., Evaluation Of Testing Condition Effects On The Resistance To Sulfide Stress Cracking, in corrosion 2009. 2009.

APPENDIX A

J INTEGRAL MATLAB CODE

```
DL=extension;P=load;
Ao=0.0075;Lo=1;
N=size(extension);
for a=1:N;
    e(a)=DL(a)/Lo;S(a)=P(a)/Ao;
end;
figure(9),plot(e,S);xlabel('nominal strain in/in');ylabel('nominal stress lbf/in2');
for b=1:N;
    er(b)=log(e(b)+1);Sr(b)=S(b)*(e(b)+1);
end;
figure(10),plot(er,Sr);xlabel('strain in/in');ylabel('stress lbf/in2');
for c=1:N;
    Lsr(c)=log(Sr(c));Ler(c)=log(er(c));
end;
eyield=0.015/8;SrUTS=max(Sr);
for d=1:N;
    if(Sr(d)==SrUTS)
        erUTS=er(d);
    end;
end;
index=0;
for f=1:N;
    if (er(f)>=eyield)&&(er(f)<=erUTS)
        index=index+1;ep(index)=er(f);Srp(index)=Sr(f);
    end;
end;
figure(11),plot(ep,Srp);xlabel('plastic strain in/in');ylabel('plastic stress lbf/in2');
for g=1:index;
    Lsrp(g)=log(Srp(g));Lerp(g)=log(ep(g));
end;
figure(12),plot(Lerp,Lsrp);xlabel('log plastic strain in/in');ylabel('log plastic stress
lbf/in2');
DLerp=diff(Lerp);DLsrp=diff(Lsrp);
for h=1:index-1;
    m(h)=DLsrp(h)/DLerp(h);
end;
mave=mean(m);
mave2=mean(DLsrp)/mean(DLerp);
K=log(SrUTS)-(mave*log(erUTS));K2=log(SrUTS)-(mave2*log(erUTS));
```

```
for i=1:index;
    Srpcalc(i)=exp(K)*(ep(i)^mave);
    Srpcalc2(i)=exp(K2)*(ep(i)^mave2);
end;
figure(11),plot(ep,Srp,'*',ep,Srpcalc,'r-',ep,Srpcalc2,'g.-');xlabel('plastic strain
in/in');ylabel('plastic stress lbf/in2');
DL=extension;P=load;
N=size(extension);
L=1;D=0.123;Ey=1.11e+007;nu=0.29;
d=D*0.8;
for i=1:N;
    if (er(i)<=eyield)
        Selastic(i)=S(i);Srelastic(i)=Sr(i);
    end;
end;
Syield=200e3;Sryield=200e3;%change for every material%
R=SrUTS/Sryield;
if(R<=1.10)
    Kic=SrUTS*(D^0.5)*(2*((d/D)^4)*(1-(d/D))+0.364*(D/d)*((1-(d/D))^2))^(1/2);
end;
for j=1:N;
    if(er(j)<=erUTS)

J1(j)=0.1*(L+DL(j))*(((3*pi*((D/2)^2)*(DL(j)^2)*Ey/(2*L))+(P(j)*DL(j))))/(2*L*pi*((d/
2)^2));erj(j)=er(j);
    end;
end;
figure(12),plot(erj,J1/1000);xlabel('delta (inch)');ylabel('JI (Ksi*inch)');
if(R>=1.10)
    Kielast=SrUTS*(D^0.5)*(2*((d/D)^4)*(1-(d/D))+0.364*(D/d)*((1-
(d/D))^2))^(1/2);J1elast=(Kielast^2)*(1-(nu^2))/Ey;J1pplast=max(J1)-J1elast;
end;
Kic2=((mean(J1)/1.25)*Ey)^0.5;Kic3=(SrUTS/(D^(3/2)))*(1.72*(D/d)-
1.27);Kic4=((max(J1)/1.25)*Ey)^0.5;
```

APPENDIX B

STRESS- STRAIN CURVE MATLAB CODE

```
DL=extension;P=load;
Ao=0.0075;Lo=1.2;
N=size(extension);
for a=1:N;
   e(a)=DL(a)/Lo;S(a)=P(a)/Ao;
end;
figure(5),plot(e,S);xlabel('nominal strain in/in');ylabel('nominal stress lbf/in2');
for b=1:N;
   er(b)=log(e(b)+1);Sr(b)=S(b)*(e(b)+1);
end;
figure(6),plot(er,Sr);xlabel('strain in/in');ylabel('stress lbf/in2');
for c=1:N;
   Lsr(c)=log(Sr(c));Ler(c)=log(er(c));
end;
eyield=0.002/1;SrUTS=max(Sr);
for d=1:N;
   if(Sr(d)==SrUTS)
      erUTS=er(d);
   end;
end;
index=0;
for f=1:N;
   if (er(f)>=eyield)&&(er(f)<=erUTS)
      index=index+1;ep(index)=er(f);Srp(index)=Sr(f);
   end;
end;
figure(7),plot(ep,Srp);xlabel('plastic strain in/in');ylabel('plastic stress lbf/in2');
for g=1:index;
   Lsrp(g)=log(Srp(g));Lerp(g)=log(ep(g));
end;
figure(8),plot(Lerp,Lsrp);xlabel('log plastic strain in/in');ylabel('log plastic stress
lbf/in2');
DLerp=diff(Lerp);DLsrp=diff(Lsrp);
for h=1:index-1;
   m(h)=DLsrp(h)/DLerp(h);
end;
mave=mean(m);
mave2=mean(DLsrp)/mean(DLerp);
K=log(SrUTS)-(mave*log(erUTS));K2=log(SrUTS)-(mave2*log(erUTS));
```

```
for i=1:index;
   Srpcalc(i)=exp(K)*(ep(i)^mave);
   Srpcalc2(i)=exp(K2)*(ep(i)^mave2);
end;
figure(3),plot(ep,Srp,'*',ep,Srpcalc,'r-',ep,Srpcalc2,'g.-');xlabel('plastic strain
in/in');ylabel('plastic stress lbf/in2');
```